Dissertation
submitted
to the
Combined Faculties
for the Natural Sciences and for Mathematics
of the
Ruperto-Carola University of Heidelberg, Germany
for the degree of
Doctor of Natural Sciences

Put forward by
Thales Nion Ada Gutcke, M.Sc.
Born in Bodrum, Turkey
Oral examination: May 2nd, 2018

The quenching of star formation in galaxies

Referees:
Prof. Dr. Andrea V. Macciò
Prof. Dr. Hans-Walter Rix

The quenching of star formation in galaxies

This thesis is concerned with investigating what makes star formation inefficient in galaxies. Cosmological, hydrodynamical simulations of galaxy formation show that the energy produced in stars, supernova explosions and active galactic nuclei must couple back into a galaxy's interstellar medium to prevent excess star formation. However, the physical processes at work in this feedback loop are not well understood. This thesis unravels the details of the baryon cycle to constrain the strength of feedback. The first part explores a phenomenological model of star formation quenching in massive galaxies, showing that gas starvation is a viable pathway to realistic elliptical galaxies. In the second part, a state-of-the-art implementation of stellar feedback is put to the test by comparing the chemical composition of the circum-galactic medium with the latest observations. The simulations exhibit a deficiency in highly ionized oxygen, indicating that models of thermally coupled feedback may be insufficient. The last part delves into the star formation prescription itself, since this directly affects the resulting stellar feedback cycle. An empirical model of a metallicity-dependent stellar initial mass function reveals the significant uncertainty resulting from the common assumption of its universality. Thus, this analysis links star formation processes with stellar feedback and shows how they affect the baryon cycle of entire galaxy ecosystems.

Die Unterdrückung von Sternentstehung in Galaxien

Diese Arbeit befasst sich mit der Ineffizienz der Sternentstehung in Galaxien. Kosmologische, hydrodynamische Simulationen der Galaxieentstehung haben gezeigt, dass die Energie von Sternen, Supernovas und aktiven galaktischen Kernen wieder in das interstellare Medium von Galaxien rückkoppeln muss, um übermäßige Sternentstehung zu verhindern. Die physikalischen Prozesse dieser Energierückkopplung sind jedoch wenig verstanden. Diese Dissertation untersucht den Baryonenzyklus in Galaxien, um die Stärke der Rückkopplung festzulegen. Der erste Teil untersucht ein phänomenologisches Modell der Sternentstehungsunterdrückung in massereichen Galaxien und zeigt das Gasmangel zu realistischen elliptischen Galaxien führen kann. Im zweiten Teil wird eine aktuell gebräuchliche Implementierung der stellaren Rückkopplung getestet, indem die chemische Zusammensetzung des zirkum-galaktischen Mediums mit neuesten Beobachtungen verglichen wird. Die Simulationen weisen einen Mangel an hochionisiertem Sauerstoff auf, was darauf hindeutet, dass Modelle mit thermischer Energierückkopplung unzureichend sind. Der letzte Teil untersucht den Sternentstehungsalgrithmus selbst, da sich dieser direkt auf die stellare Rückkopplung auswirkt. Die gängige stellare anfängliche Massenfunktion wird mit einem neuen empirischen Modell verglichen, worin sie in Abhängigkeit von der Metallizität gesetzt wird. Diese Analyse verknüpft also Sternentstehungsprozesse mit der stellaren Energierückkopplung und zeigt, welche Auswirkungen sie auf den gesamten Baryonenzyklus in Galaxien haben können.

Contents

List of Figures

List of Tables

1 Introduction

We live in a time where it is easy to forget the brilliancy of the night sky above us. We spend much of our time inside illuminated buildings. When we do go outside, the light pollution in and around big cities has turned the sky into a orange-brown murk through which Venus's blaze has become just a slight twinkle. Thus to many, astronomy seems like a fanciful and abstract science done for the amusement of a few.

This wasn't always such. Before Thomas Edison invented the light bulb, nights were dark and the stars and planets making their way across the heavens was a central part of life, a way to tell the passing of time. Watching a constellation arc across the sky allowed us to distinguish hours passing. Following the movement of the planets with respect to the backdrop of stars permitted the determination of months. Marking the position on the horizon where the sun set on the solstice was a way to count years. In this light, it is no wonder that people were fascinated by what they saw above them and turned to the stars looking for gods or at least some structure in their lives. Maybe they even wondered about other worlds beyond our own.

And yet our artificially illuminated era is also the most enlightened about the cosmos. We have seen the biggest, most fundamental leaps in our understanding of the Universe in the last 100 years. We have recognized that we live in a spiral galaxy called the Milky Way, our Sun being one of millions of other stars residing in the Milky Way. We know there are many other galaxies beyond our own. We realized the Universe is expanding and the speed of light is not infinite. This, in turn, allows us a view into the past, since light from many billions of years ago is still reaching us now. Recently, we have additionally figured out that our planet Earth is also not unique, that many of the millions of stars surrounding us host their own solar systems. While our paradigm was previously shifted from geocentric to heliocentric, all of this knowledge has further shifted it towards the

recognition that there is no center. Given these circumstances, the curious human now wants to know how all these galaxies and other worlds formed.

1.1 The challenge of galaxy formation

The formation and evolution of galaxies is a study positioned at the intersection of otherwise rather unconnected physical and astrophysical phenomena. Both large-scale cosmological structure formation and star formation theory are relevant for studying galaxy formation. Star formation even requires the understanding of physics down to the scales of hydrogen fusion and electron degeneracy. To create a predictive theory of galaxy evolution requires getting all these scales more or less "right". However, this can also just mean understanding which scales can be neglected due to having minor impact. This is challenging but making any progress is, in turn, also extremely rewarding and worthwhile because it repeatedly shifts how our eyes and mind interpret the images we see when we turn our heads towards the night sky (or towards a computer screen with digital images).

An average cosmic filament is of the order $300\,\mathrm{Mpc} \sim 10^{25}\,\mathrm{m}$. The Van der Waals radius of the hydrogen atom is $120\,\mathrm{pm} \sim 10^{-10}\,\mathrm{m}$. If our goal is to answer how common galaxies are throughout the Universe, we must bridge 35 orders of magnitude. If, in turn, we are interested in how galaxies came to look and interact the way they do, we must additionally build a model that describes the 13.8 billion years of temporal evolution of the Universe and of the galaxies forming within it.

Much progress has been made recently in the understanding of galaxy formation through the observations of the Hubble Space Telescope (HST). The Hubble Ultra Deep Field (UDF) put the Milky Way in its context of being just one of many millions of other similar (and dissimilar) galaxies throughout space.

The Cosmic Microwave Background (CMB) detections by the Cosmic Background Explorer (COBE), then by the Wilkinson Microwave Anisotropy Probe (WMAP) and most recently, the Planck satellite, have allowed a snapshot view into the Universe barely $380,000$ years after the Big Bang. From this, we were able to build a cosmological theory. We recognized that the baryonic matter we see on Earth is not the only matter present in the Universe. In fact, it is merely around 15%. The remainder is a substance we call "dark matter" for lack of more detailed understanding and the fact that it does not emit radiation.

Despite the uncertainties surrounding the nature of dark matter, we can use these numbers to run computations. N-body simulations are able to numerically calculate the non-linear outcome of cosmological theory, providing us with a picture of large-scale structure, which is known as the cosmic web. This created context for the millions of galaxies we have begun to observe. Adding hydrodynamics and simple prescriptions for star

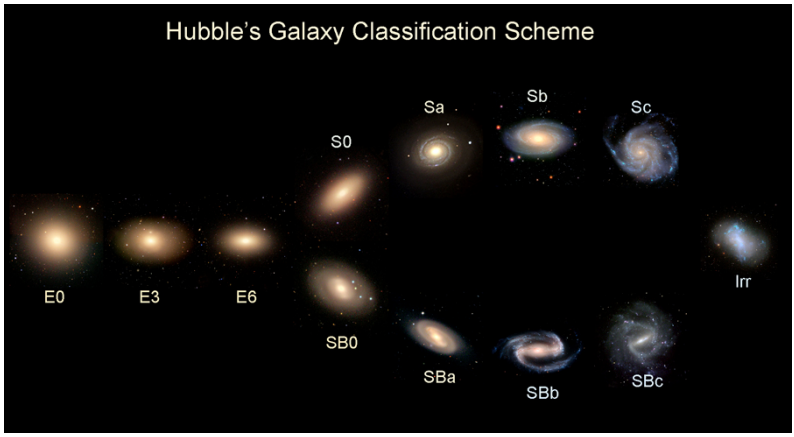

Figure 1.1. Edwin Hubble's galaxy classification. Galaxy names indicate their morphology: spiral galaxies (S0, Sa, Sb, Sc), elliptical galaxies (E0, E3, E6), barred spirals (SB0, SBa, SBb, SBc) and irregular galaxies (Irr). Image adopted from Galaxy Zoo (2018).

formation and black holes to the calculations in the simulations allows us to attempt predictions of visible structure throughout the cosmic web.

Large-scale surveys like the Sloan Digital Sky Survey (SDSS) were developed after HST to begin to gain statistics on the wealth of different galaxies. SDSS confirmed and solidified the variations we had discovered in the Hubble tuning fork (see Fig. 1.1), namely that there are generally two types of galaxies: blue and red, spiral and elliptical, star forming and non-star forming, rotationally supported and pressure supported. But the deeper we delve into the details, the more variation we see. Not all spirals are star forming, not all ellipticals are red. The ongoing work of astrophysicists is to disentangle all the data and build a coherent model that can explain and predict the wealth of observations.

More data, better telescopes, faster algorithms and bigger supercomputers are all making it steadily more attainable to bridge the "astronomical" scales necessary to understand galaxy formation.

1.2 Cosmological context

In the standard cosmological model, the Universe begins in a Big Bang. It expands homogeneously and isotropically. Slight perturbations in the homogeneity caused by quantum fluctuations are frozen-in during a period of highly accelerated expansion called inflation. These fluctuations are the origins of subsequent larger over-densities and under-densities in the distribution of energy density in the Universe.

The first Friedmann equation describes the evolution of the size of the Universe and can be derived from Einstein's field equations (Peebles 1980)

$$H^2(t) = \frac{\dot{a}(t)}{a(t)} = \frac{8\pi \mathrm{G}}{3}\rho(t) - \frac{K\mathrm{c}^2}{a^2(t)} + \frac{\Lambda}{3} \tag{1.1}$$

where the dimensionless scale factor $a(t)$ sets the scale of the Universe, G is the gravitational constant, Λ is the cosmological constant, $\rho(t)$ is the energy density and K is the curvature of space-time.

Based on various observations, most notably the CMB, it has become apparent that the Universe must be composed of various forms of energy. Not only is there matter (both baryonic and dark), but there must be another form of energy that is driving the expansion of the Universe. We call it dark energy and associate it with the cosmological constant, Λ. It comprises 70% of the energy in the Universe today, although this has not always been the case. See table 1.1 for the current cosmological parameters. The prevailing cosmological model assumes that dark energy exists and that dark matter is "cold", meaning that it only interacts weakly, if at all, with itself and other matter. Hence, this model is referred to as Λ cold dark matter (ΛCDM).

As the Universe expands, it cools. Once the temperature drops sufficiently, there is a point when baryons begin to condense into structures such as atoms. At first, protons and electrons combine to form hydrogen. This "recombination" causes a sudden drop in the free electron density. At this point, photons are abruptly able to stream freely without scattering off electrons. The CMB is created and this decoupling, thus, defines the surface of last scattering.

At this point, the Universe is dark, since most baryonic matter is in the form of neutral hydrogen. Due to the gravitational force of both dark matter and baryons, individual over-dense regions grow by accretion until a network of walls and filaments forms the cosmic web. At the intersections of dark matter filaments the over-densities are the highest. There, spherical dark matter halos form. The first galaxies to form in the centers of these dark matter halos finally provide the first light that is able to re-ionize hydrogen and end the Dark Ages at approximately $z \sim 8.5$. The remainder of the cosmological evolution of the Universe proceeds less dramatically.

1.3 The baryon cycle

Although most of the matter in the Universe is dark matter and its presence is fundamental to making accurate predictions of large-scale structure, the last few years of simulation advancement have made it ever more apparent that the small portion of matter that is baryonic plays a larger role than previously thought. Not only are baryons the only link we have between large scale structure and the visible Universe, but the electro-magnetic

Table 1.1. Planck Collaboration cosmological parameters and commonly derived values (Planck Collaboration et al. 2014).

Description	Symbol	Value
Age of the universe	t_0	$13.799 \pm 0.021 \times 10^9$ years
Hubble constant	H_0	$67.74 \pm 0.46\,\mathrm{km\,s^{-1}\,Mpc^{-1}}$
Baryon density parameter	Ω_b	0.0486 ± 0.0010
Dark matter density parameter	Ω_c	0.2589 ± 0.0057
Matter density parameter	Ω_m	0.3089 ± 0.0062
Dark energy density parameter	Ω_Λ	0.6911 ± 0.0062
Critical density	ρ_{crit}	$(8.62 \pm 0.12) \times 10^{-27}\,\mathrm{kg\,m^{-3}}$
Fluctuation amplitude	σ_8	0.8159 ± 0.0086
Redshift at decoupling	$z_\star$	1089.90 ± 0.23
Age at decoupling	$t_\star$	377700 ± 3200 years
Redshift of reionization	z_{re}	$8.5^{+1.0}_{-1.1}$

and thermodynamic characteristics of baryons make them distinct from dark matter.

With the help of cosmological, hydrodynamical simulations of galaxy formation, the dark and baryonic components can be modelled simultaneously. Through those simulations, a picture of galaxy evolution as a self-regulated system of gas inflow, star formation and outflows has emerged. This picture is replacing the more static idea of isolated disk galaxies at the centers of gravitational potential wells. Galaxies are no longer viewed as the "island universes" proposed by Curtis (1920). They are the epicenters of an entire ecosystem of cold inflows (Kereš et al. 2005), star formation, supernova ejecta and outflowing winds (Springel and Hernquist 2003; Oppenheimer and Davé 2008) that build up the energetic and chemically enriched interstellar medium (ISM), circum-galactic medium (CGM) and intergalactic medium (IGM) that we have begun to observe throughout the Universe as far back as a billion years after the Big Bang.

Given this complexity, it is surprising that galaxies display simple and tight scaling relations between many of their basic properties. In particular the well-established relations between circular velocity and luminosity (Tully and Fisher 1977), metallicity and stellar mass (e.g. Tremonti et al. 2004; Erb et al. 2006), bulge velocity dispersion and central black hole mass (e.g. Gültekin et al. 2009; Graham et al. 2011) and star formation rate and stellar mass (e.g. Davé 2008; González et al. 2010). Most have low scatter and evolve roughly independently of mass. This has given rise to the idea that there exists an underlying regularity in galaxy evolution. The complexity of current hierarchical galaxy formation models may obscure this inherent simplicity (Davé et al. 2012).

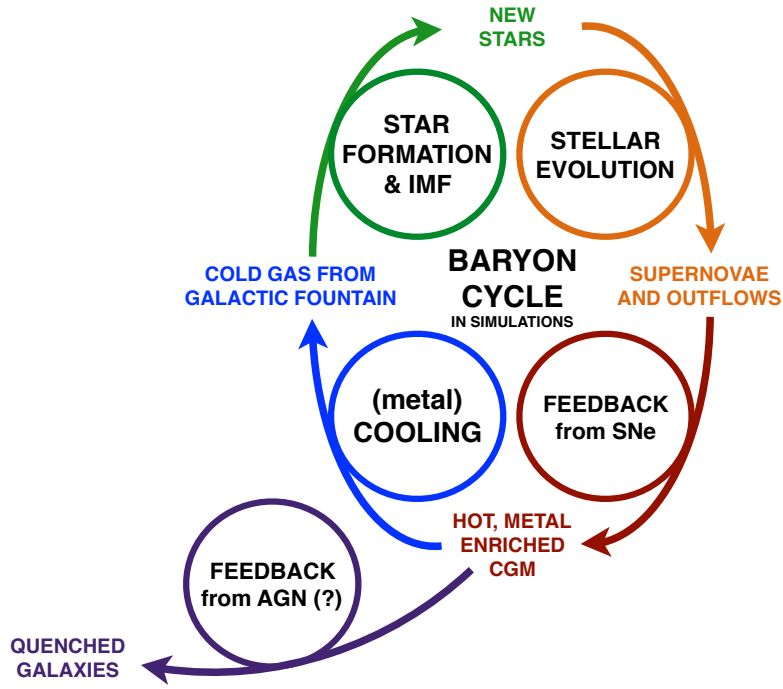

Figure 1.2. The baryon cycle in cosmological simulations. Gas cools (blue) contingent on its metallicity. Stars form out of the cold gas (green) with a given IMF that is possibly dependent on metallicity. The IMF dictates the number of resulting supernovae (orange). The supernovae feed energy and metals into the gas, producing a hot, metal enriched CGM (red). This in turn cools back onto the galaxy, restarting the cycle anew with a higher total metallicity of the gas. At some point during the lifetime of a galaxy, this cycle breaks down. The gas does not cool efficiently any longer, possibly due to heating from an AGN (purple). Thus, the quenched galaxy population is created.

1.3.1 Cooling

In the cores of dark matter halos, the dark matter and baryons decouple since the baryonic gas does not only interact gravitationally, but also electro-magnetically. Through radiation, the baryonic gas is able to shed energy and gather at the bottom of the gravitational potential wells. The baryons cool and begin to form protogalaxies. Various mechanisms for gas cooling are dominant at different temperatures. Above $\sim 10^6$ K, the gas is fully ionized and mainly cools collisionally through thermal bremsstrahlung. Between $10^4 - 10^6$ K, the gas is partially ionized and cooling is extremely density dependent. Radiation happens through free-free emission. Since the cooling timescale decreases with increasing density squared, the denser the gas gets, the more efficient its cooling becomes until it reaches temperatures of $\sim 10^4$ K. Below this temperature, molecules form and, thus, hyperfine transitions become available for radiation, producing a catastrophic cooling collapse in which the first stars form. In general, cooling is dependent on the chemical composition (termed "metallicity" in astrophysics) of the gas, since more elements provide transitions to radiate away energy.

1.3.2 Star formation

The details of cloud collapse and subsequent star formation are not well understood. In general, due to cooling clouds become cold and dense. If they accumulate enough material, they will collapse under self-gravity and produce a distribution of denser cores that become the seeds of protostars. These cores are so dense in their centers that hydrogen fusion commences. The energy produced through nuclear fusion radiates outwards, counteracting gravity and allowing the star to persist in a quasi-static pressure equilibrium. The mass of the star strongly dictates its evolution and the elements that are able to form through fusion in its core. From observations of star forming regions, it seems that stars generally form together in a single cloud collapse. The distribution function of individual star masses produced in a cloud collapse is termed stellar initial mass function (IMF).

Stellar initial mass function. The shape of the IMF is an essential input parameter in many astrophysical models and its shape is often assumed to be universal throughout time and space. The first functional form proposed by Salpeter (1955) was a single power law with a slope of 1.35. Later IMF shapes proposed in the literature incorporated a low mass turn over. The Kroupa IMF (Kroupa 2001) is described by a broken power law, where the break is set to 0.5 solar masses ($M_\odot$) and the low mass slope is 0.3. Chabrier (2003) introduced a log-normal IMF. But the notion of IMF universality has long been debated, since it is theoretically plausible that a collapsing cloud will fragment differently depending on its metallicity (also because cooling is affected by the metallicity). Some studies show a dependence of the IMF on a cloud's inner or ambient pressure. Recently,

IMF universality is also being called into question by observations. Chapter 5 will study the effects of a non-universal, metallicity-dependent IMF. An important parameter that the IMF determines is the ratio of low to high mass stars (also called the dwarf-to-giant ratio).

1.3.3 Stellar evolution and chemical enrichment

Knowing how stars age is extremely important for galaxy evolution models, since this can affect the resulting galaxy morphology and metallicity. Galaxy formation models rely on comparing predictions to observations to evaluate the "goodness" of a model. Morphology, luminosity (derived from the stellar mass) and metallicity are all vital quantities to aptly compare observed galaxies with their model counterparts. Stellar evolution is generally split into two regimes: the evolution of stars and the death of stars as supernovae.

Asymptotic giant branch stars. When low and intermediate mass stars ($M_\star \sim 0.1 - 10\,\mathrm{M}_\odot$) age, they become red giants. Their position on the color-magnitude diagram (CMD) is termed asymptotic giant branch (AGB). Here, the star undergoes a pulsation while various layers of material in the core and in shells surrounding the core contract and expand. The results is extreme mass loss and winds. This energy produced by AGB stars can create notable changes in galaxy morphology, especially in low mass galaxies.

Core collapse supernovae. Stars born with a total mass above $8\,\mathrm{M}_\odot$ will age to explode as a core collapse supernova (SNII). The exact nature of the process is not well understood. The general idea is that a massive star first fuses hydrogen in its core, then proceeds to fuse other elements. At some point, no more elements can be fused given the pressure in the core. Then, the quasi-static equilibrium breaks down and the star collapses. Due to electron degeneracy pressure in the very center, the collapse rebounds and the star "explodes" as a supernova. Some models predict varying explosion "success" rates in the mass range $8 - 40\,\mathrm{M}_\odot$. Most models do agree that all stars above $40\,\mathrm{M}_\odot$ will become supernovae and then end as BHs (Sukhbold et al. 2016). Each supernova is generally considered to develop in the same way. Thus, models have a good handle on the amount of energy released and the mass in metals produced per explosion. Core collapse supernovae primarily produce oxygen and iron. But the exact amounts vary between yield sets in the literature.

Supernovae type Ia. Supernovae type Ia (SNIa) occur in a quite different process than SNII. They are the outcome of a peculiar string of events in certain binary star systems. One of the pair must be a low mass star ($M_\star < 8\,\mathrm{M}_\odot$) that has aged to become a carbon-oxygen white dwarf. If the second star in the binary system gradually feeds material onto the white

dwarf or merges with it, the total mass can excede the threshold mass of $1.44\,M_\odot$ (Chandrasekhar mass). The white dwarf will explode. Since the mass theshold for this explosion is very consistent, SNIa are considered "standard candles" that release a fixed amount of energy per explosion. The contribution of iron from supernovae type Ia has a large impact on the total metallicity of galaxies.

1.3.4 Stellar feedback

Many galaxy properties are affected by stellar aging because AGB stars and supernovae inject large amounts of energy and chemical elements into the surrounding medium. The energy can heating it and driving galactic winds that move gas to large distances from the central star forming region. This can have a variety of effects on the morphology and chemical enrichment. Supernova blast waves can puff up disk galaxies, thus changing their scale height. Especially in low mass and dwarf galaxies, it can also rid the central region of gas necessary for further star formation, thus decreasing the amount of stars produced in total and altering the predicted luminosity function (e.g. Dekel and Silk 1986; Murray et al. 2005; Stinson et al. 2013). This is a vital aspect of galaxy quenching, which is discussed in more detail in the following section. Lastly, the amount of metals that are transported beyond the galaxy will vary with supernova feedback. This affects the predicted metal enrichment of the circum-galactic medium (see chapter 4 for more details).

When gas that was heated, expelled and enriched by supernova ejecta eventually cools and falls back onto the galactic disk, *the baryon cycle begins anew*, this time with a higher metallicity.

1.4 Quenching

The existence of red elliptical galaxies has perplexed galaxy formation and evolution modelers since the first observations of the bi-modality in the color-magnitude diagram (CMD) by Takamiya et al. (1995). Large-scale surveys such as the SDSS increased the statistical sample and broadened the knowledge of this bi-modality (Strateva et al. 2001; Baldry et al. 2004, 2006). Before then, the simple morphology and surface brightness profiles of elliptical galaxies lead to the belief that these galaxies were an early stage in the evolution process of galaxies, leading to their commonly used name early-type galaxy (ETG).

Further strengthening the distinction of the two populations, research has shown bi-modality both locally and at high redshift, not only in galaxy colors and morphologies but also their star formation rates (SFRs) (e.g. Bell et al. 2004; Brammer et al. 2009). Kauffmann et al. (2003) found that red galaxies have on average older stellar populations, higher surface stellar mass densities, and dominate at stellar masses above $10^{10.5}\,M_\odot$.

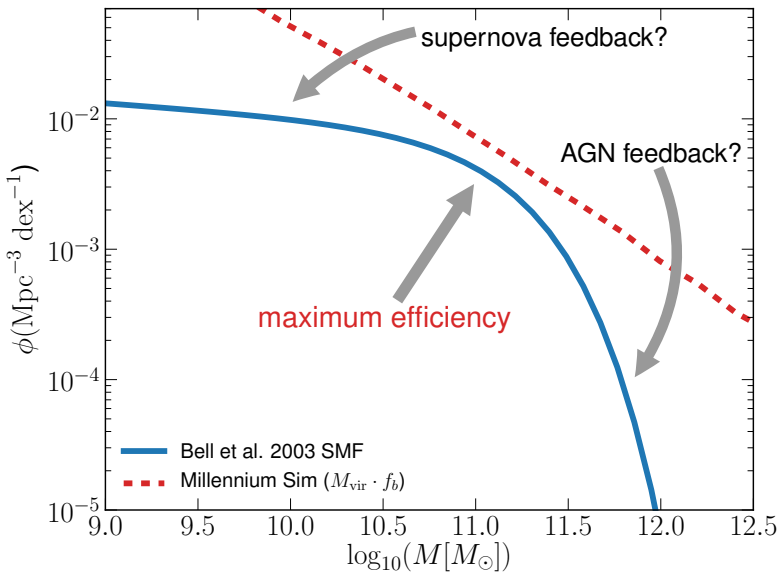

Figure 1.3. A comparison of the observed galactic stellar mass function (Bell et al. 2003, blue solid line) and the halo mass function of the Millennium Simulation (Springel et al. 2005, red dashed line). The simulation postprocessing assumes full star formation efficiency, meaning all available gas is turned into stars. Thus, the red line indicates the maximum theoretically possible stellar mass function given the distribution of halo masses. The observed function (blue) lies below the maximum at all masses, albeit the closest it gets (so the actually maximun efficiency) is at steller masses of around $10^{11}\,\mathrm{M}_\odot$. At lower stellar masses, supernova feedback is assumed to cause the low star formation efficiency. While in high-mass galaxies, AGN feedback is possibly the cause. The figure was adopted from Mutch et al. (2013).

A deeper understanding of stellar evolution has led to the insight that the red color originates from the old stellar populations. Meaning that many "intrinsically" red galaxies are at a later stage in galaxy evolution. Observations of blue galaxies have shown that disk galaxies evolve in a self-regulated manner following what is known as the galaxy star forming main sequence where the star formation rate and total stellar mass are correlated (Tacchella et al. 2016). Then, they necessarily migrate to the red sequence through a cessation of star formation (Bell et al. 2004; Faber et al. 2007).

1.4.1 Star formation efficiency

An instructive means to interpret the differences in galaxies is to calculate the efficiency with which they turn available gas into stars. This is commonly done using "abundance matching" (Moster et al. 2013; Behroozi et al. 2013). The basic assumption of abundance matching is that the luminosity derived stellar mass function and the dark matter halo mass function can be matched in mass. Thus, faint galaxies are assigned small dark matter halos and luminous galaxies are assumed to inhabit massive halos.

The resulting stellar mass-halo mass relation provides strong indications of the star formation efficiency (SFE) across stellar masses. At stellar masses below and above $10^{11}\,\mathrm{M}_{\odot}$, the star formation efficiency (SFE) decreases significantly, see Fig. 1.3. The peak efficiency around $10^{11}\,\mathrm{M}_{\odot}$ is of the order 20% compared to the cosmic baryon fraction (indicated by the red dashed line). As described in the previous section, supernovae have been shown to decrease the star formation efficiency in dwarf galaxies, thus explaining the low mass end of the discrepancy. Why star formation is inefficient at high stellar masses ($> 10^{12}\,\mathrm{M}_{\odot}$) is a central question in understanding the existence and formation of "red-and-dead" galaxies (e.g. Benson et al. 2003). Numerous attempts at modelling the formation of elliptical galaxies have explored plausible mechanisms to quench star formation and trigger a morphological change.

1.4.2 Active galactic nuclei feedback

Active galactic nuclei (AGN) feedback, the thermal or kinetic energy produced by super massive black holes (SMBHs) that reside in the centers of many galaxies, is the prime candidate to create elliptical galaxies. One motivation for this is the clustering of AGN in the "green valley", the region of the color magnitude diagram between the blue star-forming and the red quenched populations of galaxies (e.g. Nandra et al. 2007; Hasinger 2008; Silverman et al. 2008; Cimatti et al. 2013). Fig. 1.4 illustrates the green valley on the CMD. If a star-forming galaxy inhabits the blue sequence, it must cross the green valley when its star formation is quenched.

Another motivation is the success of AGN feedback implementations in

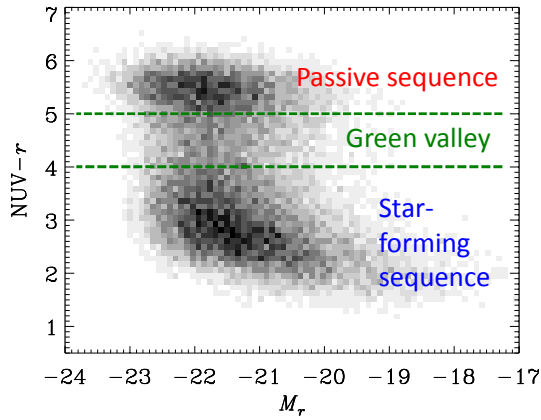

Figure 1.4. Illustration of the green valley between the blue cloud and the red sequence on the ultraviolet-optical color magnitude diagram. The grey colormap is the distribution of GALEX/SDSS galaxies from Salim et al. (2007) at $z < 0.22$. This figure was adopted from Salim (2014).

both semi-analytical and hydrodynamical models. The first of these models began by implementing one mode of AGN feedback (e.g. Di Matteo et al. 2005; Croton et al. 2006; Bower et al. 2006). Later models distinguished "radio mode" and "quasar mode" feedback (Sijacki et al. 2007; Somerville et al. 2008; Fanidakis et al. 2011, and see also Gutcke et al. 2015 for some effects of the two mode model). The two-mode model was inspired by observations of two different ways black holes (BHs) affect the gas in their vicinity. When BH accretion rates are low (low Eddington luminosity), it is common to model hot, optically thin accretion flows (e.g. an advection-dominated accretion flow or ADAF, Narayan and Yi 1994). The second mode is commonly triggered by a specific event such as a merger or disk instability. Then, BH accretion rates become extremely high (generally for short amounts of time) and models assume the BH has become a quasar that emits energy in the form of strong jets (Blandford and Znajek 1977). These models successfully create a bi-modal galaxy population with quenched, red galaxies.

However, as shown by recent large-box cosmological simulations such a Illustris (Vogelsberger et al. 2014) that employs a two-mode model and the Eagle simulations suite (Schaye et al. 2015) which uses one-mode of AGN feedback, there is still no consensus whether one or two modes are necessary. An additional uncertainty inherent in all AGN feedback models is how the energy from the AGN (possibly in the form of a jet) physically couples with the surrounding gas (e.g. see Cielo et al. 2014).

1.4.3 Alternative quenching scenarios

Another viable quenching scenario is morphological quenching in which a stellar spheroid helps the gas disk to become stable against fragmentation, which leads to less star formation (Martig et al. 2009, 2013; Genzel et al. 2014; Forbes et al. 2014). The long-term suppression of the external gas supply once the halo mass grows above a threshold mass of $\sim 10^{12}\,\mathrm{M}_{\odot}$ also counteracts excessive star formation. This can happen either via virial shock heating (Birnboim and Dekel 2003b; Kereš et al. 2005; Dekel and Birnboim 2006; Kereš et al. 2009), or by gravitational infall heating (Dekel and Birnboim 2008; Birnboim and Dekel 2011; Khochfar and Ostriker 2008), which can be aided by AGN feedback coupled to the hot halo gas (Dekel and Birnboim 2006; Cattaneo et al. 2009; Fabian 2012). Chapter 3 will examine the role of gas starvation in quenching ETGs.

The incidence of cosmic rays has been largely neglected in most galaxy evolution models. These energetic particles have the potential to increase the pressure of the gas, retaining energy and preventing it from being radiated away. Increased scale heights of the disk can prevent further star formation (Pfrommer et al. 2016).

1.5 Overview

As detailed in the previous section, a question that needs active study is *what makes star formation efficiency so low in many galaxies*. At low halo masses, this question is largely explained by supernova feedback and there seems to be consent in the in literature. On the high mass side, this question is not so agreeably solved. But despite lack of general agreement, AGN feedback does seem to be a common choice to solve this question. This thesis is concerned with investigating alternatives to AGN feedback, testing other models and producing constraints on galaxy formation models to be able to determine the source of quenching at high masses more readily. This thesis makes use of the content of the publications Gutcke et al. (2017a), Gutcke et al. (2017b) and Gutcke and Springel (2017).

The content of this thesis is organized as follows. Chapter 2 discusses the details of the two simulation codes used in the subsequent chapters. Chapter 3 presents a simple model of gas starvation that is able to quench star formation in massive galaxies. It shows how the resulting galaxies exhibit many characteristics of observed elliptical galaxies. Chapter 4 introduces the suite of zoom-in galaxy simulations called NIHAO (Wang et al. 2015) and use them to analyze the metal enrichment and morphology of the circum-galactic medium caused by supernova feedback across halo masses. The study compares this suite of simulations to relevant observations. Then, chapter 5 introduces an empirical metallicity dependent IMF model and investigates its effects on a Milky Way-like galaxy, specifically in terms of feedback and metal enrichment. Lastly, in chapter 6 the reader

will find a summary of the results of these three particular studies in the context of their impact on the theory of the baryon cycle and quenching.

2
Simulations

Galaxy formation simulations, no matter their internal methods, have generally converged in their predictions of large scale structure and, to some extent, on ways to accurately represent hydrodynamics. However, the resolution of simulations has always been its limiting factor. Individual simulation particles are many times more massive than individual stars. In grid simulations, a single grid cell often represents a spatial volume much larger than an entire star forming region.

To compare simulations with observed galaxies, there are many areas of physics that are not captured by massive particles or large, moving cells. Recall from chapter 1 that galaxy formation ultimately requiries the modelling of 35 orders of magnitude range in length scale. All the physics that is relevant for galaxy formation, but that cannot be directly simulated in current codes is implemented in what are called "sub-grid" (below resolution) models. The common practice is to build a phenomenological model that utilizes integrated quantities. This implicitly, or sometimes explicitly, assumes that the small-scale physics can be captured by modelling its large-scale effects. Star formation, stellar feedback, black hole formation and AGN feedback are all sub-grid prescriptions in state-of-the-art cosmological, hydrodynamical simulations.

This thesis employs two galaxy formation codes. For the work presented in chapters 3 and 4 is will make use of the smooth particle hydrodynamical code GASOLINE2 . Chapter 5 describes a modification and analysis that was implemented using the moving mesh code AREPO. This section will describe the major differences between the two codes and then present some features of the sub-grid models pertinent to the work in this thesis.

2.1 Smooth particle hydrodynamics

The basis of most astronomical simulation codes is a gravity solver. It is common to solve the gravitational forces between the dark matter and gas

particles using a binary tree (although there are other approaches). The simulated volume is subdivided into cubes. Nearer cubes are evaluated on a particle-by-particle (N-body) basis, while the more distant cubes are evaluated as a whole using their center of mass.

Smooth particle hydrodynamics (SPH, Monaghan 1992) is a particle based Lagrangian method for simulating hydrodynamical interactions. All forces and fluid interactions are defined on particles that move through a grid-less volume. Density and other physical quantities are calculated by summing the relevant quantities of all particles inside a smoothing kernel. The kernel defines the sphere of influence of a given particle and is often defined as a cubic spline that becomes zero at distances beyond 2ϵ, where ϵ is one smoothing length. If the kernel is a symmetric function, it will explicitly conserve energy, linear and angular momentum.

For hydrodynamical calculations it is essential to determine the density field. The density of a given particle i is calculated as

$$\rho_i = \sum_{j=1}^{n} m_j W_{ij} \tag{2.1}$$

where m_j are the masses of all n particles inside of particle i's kernel and W_{ij} is the kernel function. The density field can then be transformed onto a Eulerian grid if necessary.

To use SPH for astrophysics and bridge many scales of density it is vital to make the smoothing length adaptive such that high density regions are more highly resolved than the diffuse regions. This can be done in multiple ways, but GASOLINE2 utilizes the now common "gather" method. In effect, a number q of neighbors is defined. For each particle i, 2ϵ is determined as the distance from the particle i to its q^{th} nearest neighbor. This ensures that particles in a dense region have short smoothing lengths, since the q^{th} neighbor is closer than in under-dense areas. In general, it has been shown that $q \sim 50$ is a viable value such that the final density appropriately follows the total density field. The example of density has been used here, but this summation method is used for all necessary physical quantities.

2.1.1 GASOLINE2

The N-body SPH solver GASOLINE2 (Wadsley et al. 2017) is based on the gravity solver PKDgrav (Stadel 2001). The simulations used in this work employ a version of GASOLINE2 that treats artificial viscosity following Price (2008) using the signal velocity. The smoothing kernel is defined as the Wendland $C2$ function (Dehnen and Aly 2012), which helps avoid pair instabilities. Additionally, a timestep limiter (Saitoh and Makino 2009) was added such that the supernova blastwaves colliding with cool particles are treated correctly.

2.1.2 Sub-grid physics

The sub-grid prescriptions implemented in the version of GASOLINE2 used for this work are the same as those used in the NIHAO simulations presented in Wang et al. (2015). The following section will describe a few of the most important features.

Star formation. GASOLINE2 uses the star formation implementation by Stinson et al. (2006) with the updates described in Stinson et al. (2010). It follows a common method first proposed by Katz (1992), in which gas particles are screened for certain criteria such as a density threshold. Stars form from cool ($T < 15,000$ K), dense gas. The metal cooling readily produces dense gas, so the star formation density threshold is set to the maximum density at which gravitational instabilities can be resolved, $n_{\rm th} = \frac{50 m_{\rm gas}}{\epsilon_{\rm gas}^3}$, where $m_{\rm gas}$ is the gas particle mass and $\epsilon_{\rm gas}$ is the gravitational softening of the gas. If the criteria are fulfilled, then there is a likelihood defined by the star formation efficiency parameter, $f_{\rm SF}$ that this gas particle will produce a star. It follows the star formation equation

$$\frac{{\rm d}M_\star}{{\rm d}t} = f_{\rm SF} \frac{M_{\rm gas}}{t_{\rm dyn}}, \tag{2.2}$$

where ${\rm d}M_\star$ is added stellar mass in a simulation timestep ${\rm d}t$. $M_{\rm gas}$ is the mass of the gas particle creating the star and $t_{\rm dyn} = (4\pi G\rho)^{-1/2}$ is the dynamical time of the gas. It defines the time it would take the gas to collapse in free fall.

When it is determined that a star will form, a fraction of the gas mass is subtracted from the particle and moved to a newly introduced star particle. Each star particle is many times more massive than any single star in the Universe. Thus, it is considered a star cluster (or just a group of stars) that forms coevally and whose internal mass distribution follows a predetermined IMF shape. Star particles differ from gas particles since they do not interact hydrodynamically, i.e. they are collisionless. They obey gravity and partake in their own evolution process, whereby their mass function is altered due to the aging of the stellar population and supernovae.

Stellar feedback. The simulations use "early stellar feedback" as described in Stinson et al. (2013). In this scheme, the stars feed energy back in two epochs. The first epoch, "pre-SN feedback" (ESF), happens before any supernovae explode. It represents stellar winds and photoionization from the bright young stars, and the efficiency parameter is set to $f_{\rm SF}$=13%. Radiative cooling is left on for the pre-SN feedback.

The second epoch starts 4 Myr after the star forms, when the first supernovae start exploding. Only supernova energy is considered as feedback in this second epoch. Stars with 8 $M_\odot$ < $M_\star$ < 40 $M_\odot$ eject both energy

and metals into the interstellar medium gas surrounding the region where they formed. Supernova feedback is implemented using the blastwave formalism described in Stinson et al. (2006). Since the gas receiving the energy is dense, it would quickly be radiated away due to its efficient cooling. For this reason, cooling is delayed for particles inside the blast region for 30 Myr. This time is extended if a particle resides in the blast region of multiple supernovae.

Metal diffusion and cooling. The metal diffusion used in this work is described in Wadsley et al. (2008), but we do not use the diffusion of thermal energy between particles, because it is incompatible with the blastwave feedback that delays cooling. The cooling is as described in Shen et al. (2010) and was calculated using CLOUDY (version 07.02; Ferland et al. 1998) tables that include photoionization and heating from the Haardt and Madau (2005) UV background, Compton cooling, and hydrogen, helium and metal cooling from 10 to 10^9 K. In the dense, interstellar medium gas we do not impose any shielding from the extragalactic UV field as the extragalactic field is a reasonable approximation in the interstellar medium.

2.2 Moving mesh

Moving mesh is a synthesis of SPH features and standard grid codes. The hydrodynamical calculations in standard grid codes subdivide the volume into cells for which the flow of energy, mass and momentum is calculated through the surfaces of each Eulerian grid cell. Adaptive mesh refinement (AMR) methods improve on this by adaptively subdividing the grid when more resolution is needed in specific regions. However in a moving mesh, the grid not only adapts its size, it additionally moves to follow the fluid flow. This works by constructing the grid as a Voronoi tessellation of the mesh-generating points (see Springel 2010), which are semi-equivalent to gas particles in SPH.

The synthesis of these features solves some weaknesses of the both the SPH and the standard AMR methods. For instance, it has been shown that SPH codes have large errors when simulating shocks and sharp boundaries, as it produces spurious pressure terms. This is solved in the Eulerian grid calculation. On the other hand, AMR is non-Galilean invariant (although see Robertson et al. 2010, for an argument that the errors are caused by numerical diffusion).

The gravity solver for moving mesh uses the same binary tree as common SPH codes. The dark matter remains an N-body particle calculation.

2.2.1 AREPO

The moving mesh simulation code used in this work is AREPO (Springel 2010). The following will present some key features of the sub-grid models

implemented in the version of AREPO used here, which is the same as in IllustrisTNG presented in Pillepich et al. (2018).

2.2.2 Sub-grid physics

Multiphase ISM and Star Formation. AREPO uses a star formation prescription similar to the initial implementation by Springel and Hernquist (2003) for the SPH code GADGET and with updates described in Pillepich et al. (2018). In this method, the gas in each cell is assumed to represent a part of the multi-phase ISM. As such, the cell mass is split into a hot ambient medium and a fraction of cool clouds. The total cell, thus, receives an effective equation-of-state (eEOS)

$$\mathrm{P_{eff}} = (\gamma - 1)(\rho_\mathrm{h} \mathrm{u_h} + \rho_\mathrm{c} \mathrm{u_c}), \tag{2.3}$$

where γ is the adiabatic index, ρ_h and ρ_c denote the density of the hot and cold medium, respectively. $\mathrm{u_h}$ and $\mathrm{u_c}$ are the internal energies of the two media. The mass ratio of hot and cold components only depends on the total density of the cell once the cooling curve and IMF are fixed.

Three processes exchange mass between the phases. Star formation takes mass out of the cool clouds. Cloud evaporation caused by thermal energy from supernovae moves mass from the cool phase to the hot phase. Radiative cooling allows cloud growth by moving mass from the hot medium into the clouds. Given the exchange between the stars and the hot and cold ISM components, there is a regime where star formation is self-regulated. In the model, it is assumed that self-regulation always holds and that the multiphase model can be simplified to a stochastic calculation. Thus, given a density dependent star formation rate (SFR), a star particle is created when a randomly drawn number fullfils a probability criteria.

Throughout the simulation, each star particle is evolved injecting mass and metals back into the ISM through supernova Ia and II. The metallicity enhancement is tracked for the nine most abundant elements in the Universe: H, He, C, N, O, Ne, Mg, Si, and Fe. Additionally, asymptotic giant branch (AGB) stars also produce metals and winds.

Cooling. Gas cooling is calculated for two channels, UVB and metal line cooling. The implementation of metal-line cooling on the rates for a solar composition gas, and these rates are scaled linearly with the total metallicity Z. The total net cooling rate (as detailed in Vogelsberger et al. 2014) is

$$\Lambda(T, \rho, z, Z) = \Lambda_\mathrm{p}(T, \rho, z) + \frac{Z}{Z_\odot} \Lambda_\mathrm{m}(T, \rho, z, Z_\odot) + \Lambda_\mathrm{C}(T, \rho, z). \tag{2.4}$$

Λ_p is the contribution from primordial elements, Λ_m is the integrated contribution from the metal lines and Λ_C is the Compton cooling off the CMB. Note that time enters here as the redshift, z.

Black Holes. The version of AREPO used in this work employs a subgrid prescription for the formation, growth and evolution of super-massive black holes (SMBHs). All details are described in Weinberger et al. (2017). Here, the reader will find a summary the most important aspects. It is a two mode model that distinguishes low-accretion and high-accretion BHs. In the low-accretion mode, feedback is kinetic, meaning that the BH drives winds that create large-scale outflows. This subgrid prescription attempts to phenomenologically recreate advection dominated accretion flows (ADAFs, Yuan and Narayan 2014). In the high-accretion mode, the BH inputs thermal energy into the surrounding gas. The initial black hole seed mass is set to $8 \times 10^5 h^{-1}\,\mathrm{M}_\odot$. This model has been shown to successfully quench high mass galaxies ($10^{12} - 10^{14}\,\mathrm{M}_\odot$) and create a population of low-star forming galaxies that display elliptical morphology (Pillepich et al. 2018).

3

Forming realistic massive ellipticals with a simple model of quiescence[†]

It is our goal to understand the star formation quenching of galaxies and we will begin by developing a simple phenomenological model that alters the fate of massive galaxies. In this model, hot gas (all gas above a temperature threshold) in a $\sim 10^{12}\,\mathrm{M}_\odot$ halo mass galaxy at redshift $z \sim 3$ is prevented from cooling. The cool gas continues to form stars at a decreasing rate and the galaxy stellar mass, morphology, velocity dispersion and position on the color magnitude diagram (CMD) proceed to evolve. By $z = 0$, the halo mass has grown to $10^{13}\,\mathrm{M}_\odot$ and the galaxy has attained characteristics typical of an observed $z = 0$ elliptical galaxy. Additionally, we post-process our simulations with a radiative transfer code to create a mock CMD. In contrast to previous assumptions that a pure "fade away" model evolves too slowly to account for the sparsity of galaxies in the green valley, we demonstrate crossing times of $\lesssim 1\,\mathrm{Gyr}$. The model we present is a gas starvation model in which we remain agnostic to the physical mechanism at work to conclude that no sudden quenching event is necessary to produce the rapid colour transitions commonly observed in transition galaxies.

3.1 Introduction

There is a general consensus that the separation of galaxies into two distinct populations (the galaxy bimodality) is caused by two evolutionary epochs

[†] The contents of this chapter was published in similar form in Gutcke et al. (2017a)

in a galaxy's life. Galaxies tend to develop into star forming disks when they are less massive and transition to red spheroids when they age. The resulting gap between the blue galaxies and the red sequence in the CMD is termed the "green valley". The galaxies in the green valley constitute a transiting population between the two regions (e.g. Bell et al. 2004; Faber et al. 2007; Martin et al. 2007; Schiminovich et al. 2007; Wyder et al. 2007; Mendez et al. 2011; Gonçalves et al. 2012). Various authors have defined the green valley differently, some specifying a region in the UV-optical diagram, some using the optical-optical diagram. Although the precise definition can vary, the results seem to stay consistent.

The more rapid the transition through the green valley, the sparser this region in the CMD will be. But Peng et al. (2010) found the sparsity consistent with an overlap of a fast and a slow quenching mechanism. The timescale commonly used to distinguish fast and slow modes lies around 1 Gyr (Schawinski et al. 2007; Salim 2014). But Martin et al. (2007) recognised that the number density in the green valley does not deliver a crossing time by itself. Using $H\delta_A$ and $D_n(4000)$ spectral indices and physically reasonable star formation histories, they found that quenching timescales vary widely and green valley crossing times can be around and above 2.5 Gyr for some galaxies. Yesuf et al. (2014) used SDSS, GALEX and WISE data to estimate a transit time of 7 Gyr for the slowest galaxies, assuming that by far the majority ($\sim$ 74%) of red sequence galaxies follow the slow quenching mode. Trayford et al. (2016) used the EAGLE simulation to estimate crossing times. Although they distinguish between three characteristic evolutionary paths across the green valley, they find no distinct difference in crossing times between them. Using the Galaxy Zoo morphological classification, Smethurst et al. (2015) identified three seemingly distinct quenching timescales: morphologically smooth galaxies quench rapidly following major mergers. Disk-like galaxies quench on slow timescales caused by secular evolution. Their intermediate population reddens in intermediate timescales, which the authors attribute to minor mergers and galaxy interactions.

Although investigation into quenching mechanisms has gone far and wide, no general agreement has emerged as to which effect dominates in massive galaxies. This has led to models such as Dutton et al. (2015b) and Gabor and Davé (2015) who attempt to understand the effects of quenching without defining a physical origin. Motivated by the success of halo quenching models (Cattaneo et al. 2006), Dutton et al. (2015b) investigated a 'forced quenching' scenario where cooling and star formation are shut off at $z \sim 2$. They show that this process results in present day elliptical galaxies with stellar masses and structural properties in broad agreement with observations.

This study extends the study by Dutton et al. (2015b) by constructing a quiescence model that allows some cooling and star formation to occur after the halo quenching begins. We present the characteristics of the resulting elliptical galaxies and quantify the deviations from observations.

Table 3.1. Simulations run for this analysis and their respective parameters: $T_{\rm off}$, the temperature above which gas cooling was turned off; $M_{\rm vir}$, the virialized mass at $z = 0$; $M_\star$, the stellar mass inside $0.1R_{\rm vir}$ at $z = 0$; $R_{\rm vir}$, the radius at $z = 0$ enclosing 200 times the critical density. The table is divided into three sections: The first five simulations are the ones we will focus on most in the analysis. The second group of three are the control simulations for our three initial conditions and the third group of five are low resolution simulations we ran to test various parameter choices.

Name	$T_{\rm off}$ [10^5K]	$M_{\rm off}$ [10^{12} M$_\odot$]	$M_{\rm vir}$ [10^{13}M$_\odot$]	$M_\star$ [10^{11}M$_\odot$]	$R_{\rm vir}$ [kpc]
Halo1	1.0	2.48	1.375	0.85	510
Halo2	1.0	2.37	1.222	1.55	509
Halo3	1.0	1.94	1.229	1.17	496
Halo3late	1.0	4.11	1.268	2.62	495
Halo2h	1.0	2.39	1.232	1.70	490
Halo1c	-	-	1.363	6.74	507
Halo2c	-	-	1.241	8.68	492
Halo3c	-	-	1.268	7.5	495
H3-5e4	0.5	1.02	1.259	0.45	472
H3-1e5P	1.0	1.39	1.268	1.09	471
H3-1e5	1.0	1.02	1.249	0.63	471
H3-5e5	5.0	1.02	1.223	1.11	468
H3-1e6	10.0	1.02	1.219	1.54	467

Our model makes no assumptions about the cause of the limited cooling and can be compared to a variety of quenching mechanisms.

The structure of this chapter is as follows: In §3.2 we describe our quiescence model in detail. In §3.3 we compare our resulting galaxies to observations: in §3.3.1 the stellar mass-halo mass relation; in §3.3.2 the star formation histories (SFHs); in §3.3.3 the specific star formation rate (sSFR) - stellar mass relation; in §3.3.4 the CMD; in §3.3.5 the size-mass relation and in §3.3.6 the Faber-Jackson relation. §3.4 discusses and summarizes our results.

3.2 Numerical Simulations

Numerical simulations have been performed using a improved version of the smooth particle hydrodynamics (SPH) code GASOLINE2 (Wadsley et al. 2004; Keller et al. 2014), this new version promotes mixing and strongly alleviates the well known issues of the classical SPH formulation (Agertz

Table 3.2. Same as table 3.1 but showing further parameters: $m_{\rm dark}$, the mass of a dark matter particle in the zoom-in region; $m_{\rm gas}$, the mass of a gas particle in the zoom-in region; $\epsilon_{\rm dark}$, the dark matter particle softening length; $\epsilon_{\rm gas}$, the minimum gas particle smoothing length; $N_{\rm dark}$, the number of dark matter particles in the zoom-in region; $N_{\rm gas}$, the number of gas particles in the simulation.

Name	$m_{\rm dark}$ $[10^6 {\rm M}_\odot]$	$m_{\rm gas}$ $[10^6 {\rm M}_\odot]$	$\epsilon_{\rm dark}$ [kpc]	$\epsilon_{\rm gas}$ [kpc]	$N_{\rm dark}$ million	$N_{\rm gas}$ million
Halo1	20.71	1.139	2.127	1.192	1.24	1.25
Halo2	20.71	1.146	2.033	1.114	1.26	1.04
Halo3	20.71	1.146	1.987	1.114	1.34	1.14
Halo3late	20.71	1.145	2.127	1.192	1.34	1.30
Halo2h	2.6	0.140	1.060	0.600	15.4	10.05
Halo1c	20.71	1.144	2.127	1.192	1.26	1.11
Halo2c	20.71	1.147	2.127	1.192	1.26	1.07
Halo3c	20.71	1.147	2.127	1.192	1.34	1.18
H3-5e4	165.7	9.509	3.989	1.709	0.17	0.17
H3-1e5P	165.7	9.416	3.989	1.709	0.17	0.17
H3-1e5	165.7	9.416	3.989	1.709	0.17	0.17
H3-5e5	165.7	9.453	3.989	1.709	0.17	0.17
H3-1e6	165.7	9.262	3.989	1.709	0.17	0.17

et al. 2007). The baryonic physics treatment is the same adopted for the NIHAO simulation suite (Wang et al. 2015). Namely the code includes a subgrid model for metals mixing (Wadsley et al. 2008), ultraviolet heating and ionization and cooling due to hydrogen, helium and metals as detailed in Shen et al. (2010).

The star formation and stellar feedback follow the implementation of the MaGICC simulations by Stinson et al. (2013). We set the star formation threshold as suggested in Wang et al. (2015), using a critical density of 5.17 cm^{-3}. The density threshold is defined as a kernel of 52 gas particles within a sphere of radius equal to the softening length. Stars can return energy back to the inter-stellar medium (ISM) via blast-wave supernova (SN) feedback (Stinson et al. 2006) and via ionizing radiation from massive stars (early stellar feedback) before they turn in SN (Stinson et al. 2013). Metals are produced by type II and type Ia SN. Stars also return mass to the ISM via asymptotic giant branch stars. We adopt a Chabrier (2003) stellar initial mass function which sets the fraction of stellar mass that results in SN and winds.

We select three haloes with a present-day mass of about 10^{13} $M_\odot$ from the Planck simulations from Dutton and Macciò (2014) to be re-run at higher resolution. The initial conditions were created using a modified version of GRAFIC2 (Penzo et al. 2014); the starting redshift is $z_{\rm start} = 99$.

We run three halos which we call Halo1, Halo2 and Halo3. Halo1 has a quiescent merger history, while Halo2 and Halo3 have one major merger each (at 11 Gyr and 7 Gyr, respectively) and some minor mergers in their past. We also run a control simulation of each halo without any changes to the cooling (Halo1c, Halo2c, Halo3c). To check for convergence, we run Halo2 at three different resolution levels and Halo3 at two. See table 3.1 for an overview of the simulations and the halo properties.

We use the Amiga Halo Finder (AHF, Knollmann and Knebe 2009) to identify gravitationally bound structures and to track these throughout cosmic time. We rely on the AHF output for estimating the viral radius, which is defined so that it encloses an overdensity of 200 times the critical density of the Universe.

3.2.1 A simple model of quiescence

Numerical simulations without any form of feedback consistently overestimate the number of stars created in low mass and high mass galaxies. At the low mass end, it has become accepted to implement feedback from supernova and even radiation from young stars. For high mass galaxies often AGN feedback is assumed to limit the cooling. But observations are still very ambivalent as to whether this heating mechanism truly is able to affect such a large fraction of the gas in the centers of galaxies (see Cielo et al. 2014 for numerical simulations showing this). Many other physical mechanisms have been tested in simulations to limit SF, each varying in physical viability and success.

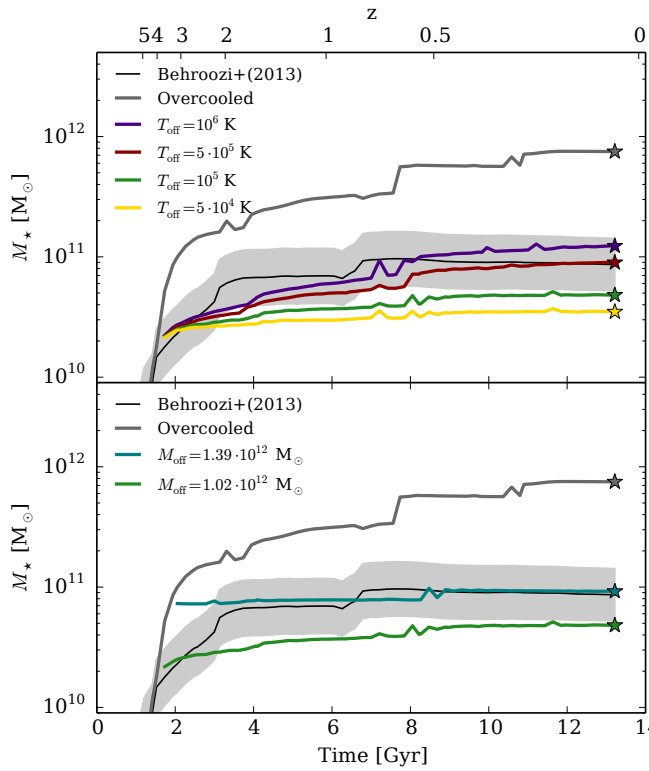

Figure 3.1. *Top:* Halo3 simulated 5 times with varying parameter $T_{\rm off}$ and $M_{\rm off} = 1.02 \times 10^{12}\,{\rm M}_\odot$(Halo3c, H3-5e4, H3-1e5, H3-5e5, H3-1e6). *Bottom:* Halo3 with varying parameter$M_{\rm off}$and $T_{\rm off} = 10^5$K (Halo3c, H3-1e5P, H3-1e5). The stellar mass is defined as the sum of all stellar particle masses within 0.1 $R_{\rm vir}$.

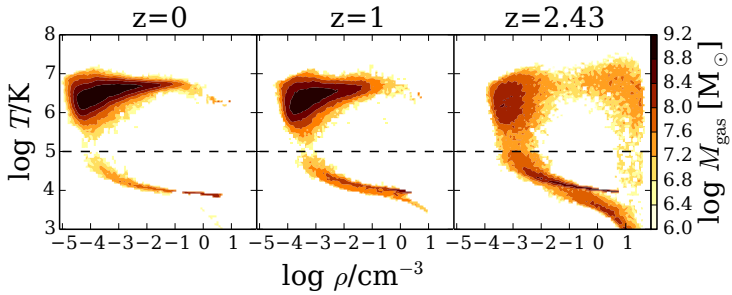

Figure 3.2. Phase diagrams for Halo3 at three different redshifts, $z = 2.43$ (where the cooling mode is switched), $z = 1$ and $z = 0$. Bin widths are $\log(\rho/[\mathrm{cm}^{-3}]) = 0.07$ and $\log(T/[\mathrm{K}]) = 0.05$. The dashed line indicates the $T_{\mathrm{off}} = 10^5$K. The parameter forces the disk and hot halo to separate at this temperature.

Here we are interested in a much simpler question: would it be enough to prevent accretion of cold gas to create a realistic elliptical galaxy? In other words, can we create a red-and-dead galaxy simply by starving galaxies above a critical mass? To test this, we implement a very simple model to force a quiescent evolution: up to a critical total mass (called M_{off}) a galaxy is allowed to evolve freely. Then, once this mass is reached we shut off cooling for all gas particles above a critical temperature T_{off}. The critical mass and temperature are the only two parameters of our simple model. It is important to notice that even for haloes above M_{off} we halt neither cooling nor star formation completely. Cold gas (i.e. below T_{off}) is still able to cool and form stars, which in turn will be sources of stellar feedback. We simply prevent the cooling (and hence accretion) of gas above T_{off} onto the galaxy.

In Fig. 3.1 we show the effects of different choices for the two parameters in our model on the evolution of the stellar mass for Halo3 at low resolution (third part of Table 3.1). Here and in the rest of this work, the stellar mass is defined as all stellar particle masses within $0.1R_{\mathrm{vir}}$. The black line shows the expected evolution of the stellar mass according to abundance matching results from Behroozi et al. (2013), the (thick) dark grey line represents the simulation without suppressed cooling which overproduces the final stellar mass by a factor of almost 10. In the upper panel we present results for four different values of T_{off} at a fixed $M_{\mathrm{off}} = 1.02 \times 10^{12}$ $\mathrm{M}_\odot$, while in the lower panel we vary M_{off} at a fixed $T_{\mathrm{off}} = 10^5$ K.

This simple study seems to justify using $M_{\mathrm{off}} = 1.4 \times 10^{12}$ $\mathrm{M}_\odot$. However, increased resolution slightly changes the star formation history (due to lower stellar mass, see Mayer et al. 2008) and we have to increase M_{off} to 2×10^{12} $\mathrm{M}_\odot$ to get the correct final stellar mass. So, for the rest of

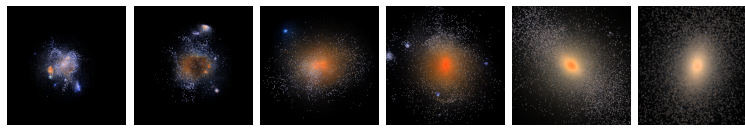

Figure 3.3. 50 kpc×50 kpc `SUNRISE` RGB images of Halo1 at redshifts (Gigayears) 2.9 (2.2), 2.6 (2.5), 1.8 (3.5), 1.6 (4.0), 0.7 (7.1), and 0.0 (13.8), from left to right. The onset of the quiescence mode is at 2.2 Gyr.

this work, the fiducial parameters for our model are: $T_{\rm off} = 10^5\,{\rm K}$ and $M_{\rm off} = 2\times10^{12}\ {\rm M}_\odot$. There is some variation from simulation to simulation in the parameter $M_{\rm off}$, given that we restart from the snapshot with a halo mass closest to the fiducial $M_{\rm off}$ value, and snapshots are on average 200 Myr apart. Given the intrinsic simplicity of our model we didn't see the need for any more fine tuning of our parameters.

Fig. 3.2 shows the phase diagram for Halo3 at three redshifts, $z = 2.43$, 1, and 0. The black dashed line indicates our choice of $T_{\rm off}$. This choice is in line with previous studies such as Gabor and Davé (2015). They heat the circum-galactic gas to $10^{5.4}\,{\rm K}$, preventing further star formation and successfully producing hot halos. The temperature is a local minimum in the cooling curve of simulations, distinguishing free-free emission and helium cooling. The temperature break forces the Halo3 phase diagram to separate along this temperature, resulting in a hot halo phase in the upper left and a denser, colder disk phase below our temperature threshold. The disk phase ($T \lesssim 10^4\,{\rm K}$, $\rho \gtrsim 10^{-2}\,{\rm cm}^{-3}$) is depleted over time since each cycle of star formation produces stellar winds and supernovae that heat a fraction of the gas to above the threshold temperature, thus making it unavailable for further cooling and star formation.

In this analysis, we are interested in affecting the gas and creating a galaxy that has a morphology and other properties typical of the elliptical population. This allows us to get a grasp on the conditions necessary in simulations for creating a quiescent environment. Our primary concern is to understand whether a pure fade-away model where gas is slowly consumed by star formation can match observational constraints without an abrupt, violent quenching event. The quiescence model makes no assumptions about the physical process that quenches a galaxy. Being agnostic about the mechanism can be used to our advantage. It can in principle be either a model of inefficient cooling or of a supplementary heating mechanism that counteracts cooling. This way, our results can be freely compared to a variety of quenching models.

3.3 Comparing to observations

We compare our model galaxies with observations of $z = 0$ elliptical galaxies. In particular, we consider the stellar mass-halo mass relation, the SF

history, the size-mass relation, the stellar mass-velocity dispersion relation and the transition from the blue cloud to the red sequence on the color magnitude diagram. To obtain a fairer comparison with observables, we run the Monte Carlo radiative transfer code `SUNRISE` (v5.0, Jonsson 2006). The code uses the stellar population synthesis model Starburst99 (Leitherer et al. 1999), assumes a Kroupa initial mass function (IMF) and traces 10 million rays per galaxy. The calculation includes dust estimates that absorb and scatter the rays. The dust mass is set to 0.4 times the metal mass for each gas particle. Additionally, dust within the birth cloud around newly formed star particles ($t_{\rm form} < 10\,{\rm Myr}$) is modeled in sub-grid using `MAPPINGS III` (Groves et al. 2008).

For the transformation from the particle positions to the grid needed by `SUNRISE`, the radius of a gas particle is defined as the distance to the 32nd nearest neighbor. The stellar radius is defined as 0.2 times the gravitational force softening. Fig. 3.3 shows six `SUNRISE` images of the Halo1. From left to right the redshifts (Gigayears) are 2.9 (2.2), 2.6 (2.5), 1.8 (3.5), 1.6 (4.0), 0.7 (7.1) and 0.0 (13.8). Morphologically, the galaxies look elliptical and red at $z = 0$.

3.3.1 Stellar mass - halo mass relation

The relation between the stellar mass of a galaxy and the total mass of the halo including dark matter is a strong constraint on galaxy formation models. For the stellar mass, $M_\star$, we consider all stars within 10% of the virial radius, $R_{\rm vir}$. The total halo mass, $M_{\rm Halo}$, includes all particles within $R_{\rm vir}$. The relation constructed between these two quantities is our primary observational constraint, and we choose our two model parameters to reproduce it. Fig. 3.4 shows the abundance matching results for $M_{\rm Halo}$–$M_\star$ from Moster et al. (2013), Behroozi et al. (2013) and Kravtsov et al. (2014). The star markers show our three elliptical halos at $z = 0$ and the blue dots show the high resolution NIHAO sample. The NIHAO sample follows the relation across two orders of magnitude in halo mass, from $10^{10} - 10^{12}$ M$_\odot$. Our quiescence model galaxies also lie on the relation at $10^{13} M_{\rm Halo}$. In this context, our model is the high mass extension of the NIHAO sample.

Fig. 3.5 shows the evolution of $M_{\rm Halo}$–$M_\star/M_{\rm Halo}$ of our three galaxies (one galaxy per panel) at the fiducial resolution level. The black stars mark the point at which the cooling mode is switched from regular metal-line cooling to the quiescence mode. The black solid lines show the abundance matching results reported by Behroozi et al. (2013), where the gray band encloses the $1 - \sigma$ scatter. We match the slope of the relation after the onset of the quiescence mode by construction, since the parameter $T_{\rm off}$ determines its behaviour. A lower $T_{\rm off}$ produces a steeper slope, while a higher $T_{\rm off}$ produces a flatter evolution. The parameter $M_{\rm off}$ was also chosen to match this relation since the knee generally appears around 2×10^{12} M$_\odot$. Halo3 in the lowest panel of Fig. 3.5 shows a slight bump above the abundance matching area around 10^{12} M$_\odot$ due to a merger. We

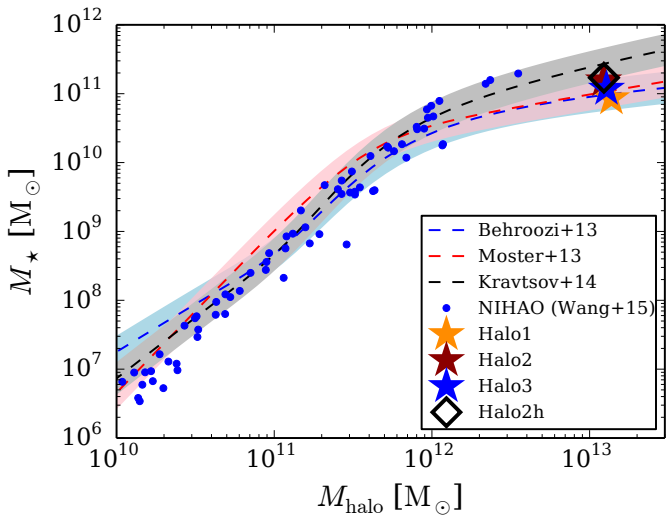

Figure 3.4. $z = 0$ Stellar mass - halo mass relation for our galaxies (stars and diamond) and those of the NIHAO sample (blue dots), which use the same physics until we switch into quiescence mode. The blue dashed line and band shows observational data based on abundance matching from Behroozi et al. (2013). Red line with a pink band shows the results of Moster et al. (2013) and black line with grey band shows results of Kravtsov et al. (2014).

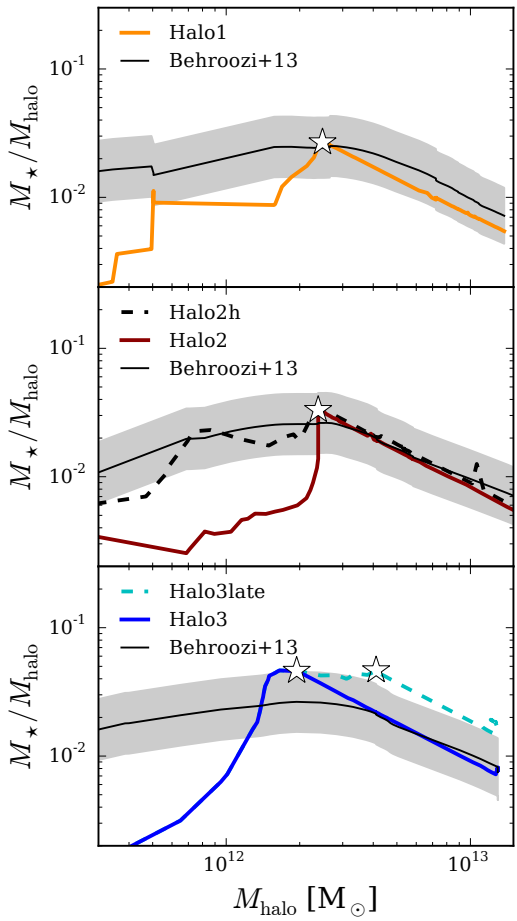

Figure 3.5. Stellar mass/halo mass - halo mass relation for our galaxies. The gray band shows observational data based on abundance matching from Behroozi et al. (2013). The colored bands show the $1-\sigma$ scatter for the data.

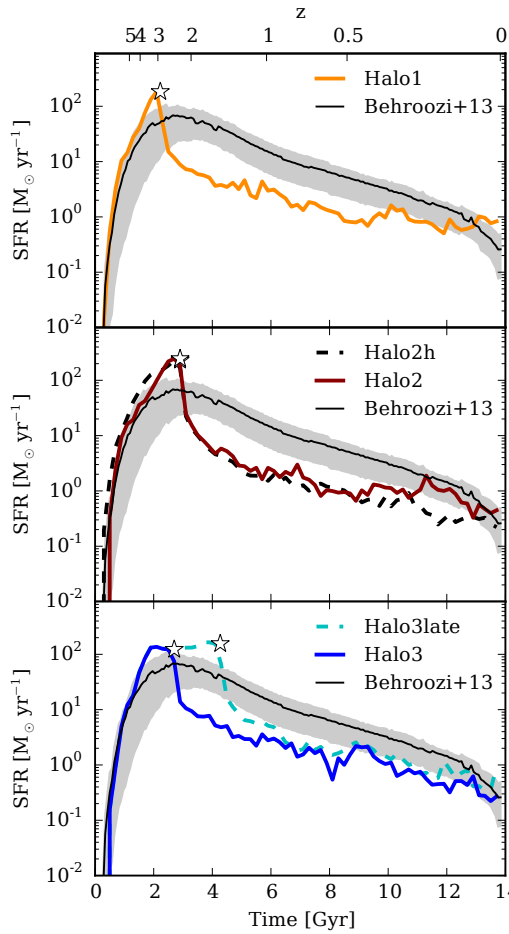

Figure 3.6. The star formation history of our galaxies, with the star markers showing the switch to quiescence mode. The black line is the SFH based on abundance matching from Behroozi et al. (2013). The grey band shows the errors on individual galaxies.

also show the relation for Halo3late, which is the same as Halo3 except that $M_{\rm off}$ is higher by a factor of about two. This leads to a higher final stellar mass. The change in final stellar mass and the intrinsic scatter in the Behroozi et al. (2013) relation show that a range of $M_{\rm off}$ are allowed while still reproducing the necessary shape.

3.3.2 Star formation history

The abundance matching technique predicts the expected stellar mass for a given halo mass at a given time. This information can be translated into the star formation rate of a galaxy throughout it's lifetime, it's star formation history (SFH). The SFH is constructed by considering the formation time of all stars and summing their mass in bins of 1 Gyr. Fig. 3.6 shows the SFH of each galaxy. The SF decreases over time after the onset of the quiescence mode (the black star in each panel). The initial ($1-3$ Gyr) and the final ($12-13$ Gyr) times broadly agree with the abundance matching results (black solid line, Behroozi et al. 2013). It should be noted that the SFHs from abundance matching shown here are for generic galaxies with $z=0$ halo masses in the range $10^{13}-10^{13.2}$ $M_{\odot}$. Our galaxies's final halo masses all fall within this range.

Due to the swiftness with which the star formation drops at the onset of the quiescence mode, there is a discrepancy at intermediate times ($4-11$ Gyr). Again, we compare Halo3 (blue line) and Halo3late (light blue dotted line) where the cooling mode is switched later, at $z=1.5$. The SF drops to values below 10 $M_{\odot}yr^{-1}$ after the switch and then progresses similarly to Halo3. From Fig. 3.5, we know the final stellar mass lies just outside the $1-\sigma$ range of the abundance matching relation. This shows that some amount of scatter in $M_{\rm off}$ is necessary (and expected) to reproduce the knee of the relation.

The intermediate times are not reproduced by these SFHs and we acknowledge the limitations of the model in this respect here, since we are not trying to produce the diversity of galaxies and SFHs seen in observations with this simulation. Ours is a heuristic quenching model with which we are merely trying to show that it can make large ellipticals. In the central panels the black dashed line shows results for the high resolution version of Halo2 (Halo2h); the fiducial and high resolution simulations agree well.

Fig. 3.7 shows the origin of all stars in each halo at $z=0$. The red and orange wedges are the fraction of stars that formed (in-situ and ex-situ) after the change in cooling mode. The total percentages are 28.7%, 21.6% and 21.7% for Halo1, Halo2 and Halo3, respectively. This means a small, but non-negligible fraction of stars form at late times after the onset of the quiescence model. The accreted fraction, or fraction of stars formed ex-situ is 26.6%, 46.5% and 18.6%, respectively, in good agreement with the results from the Illustris simulation (Rodriguez-Gomez et al. 2016), in which quenching is achieved via AGN feedback using both radio and quasar mode.

3.3.3 Specific star formation rate

The specific star formation rate (sSFR) defined as SFR/$M_{\star}$is a measure of the efficiency with which a galaxy turns gas into stars. The bi-modality of "blue" and "red" galaxies is apparent in their sSFRs. The distribution of galaxies in the stellar mass - sSFR plane shows a clear distinction between

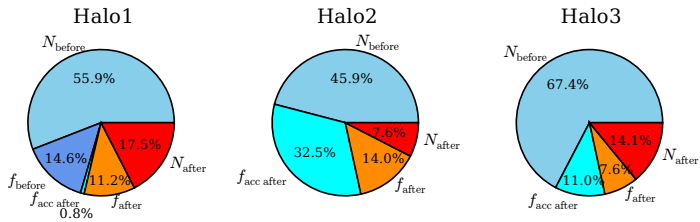

Figure 3.7. Pie charts for each halo showing the fractional origin of all stars present in the halo at $z = 0$. $N_{\rm before}$ and $N_{\rm after}$ are the fraction of stars that formed in the halo before and after the switch in cooling mode, respectively. $f_{\rm before}$ is the fraction of stars that formed and were accreted before the switch, while $f_{\rm acc\ after}$ are the fraction of stars formed before and accreted after the switch. $f_{\rm after}$ is the fraction formed and accreted after the switch in cooling modes. Both Halo2 and Halo3 have negligible fractions of stars that accreted before, $f_{\rm before}$, so these were omitted from the plot.

the "star forming main sequence" of galaxies with sSFR$\sim 10^{-10}{\rm yr}^{-1}$ at $z = 0$ and a population of galaxies with higher average stellar masses and sSFR$\sim 10^{-12}{\rm yr}^{-1}$. Fig. 3.8 shows the $z < 0.2$ SDSS density of galaxies on this plane as a grey contours. The stellar masses are taken from Kauffmann et al. (2003) and Salim et al. (2007) while the sSFRs are from Brinchmann et al. (2004).

Our galaxies's evolutionary tracks are the colored lines as detailed in the legend. Their $z = 3$ and $z = 0$ positions are marked by squares and stars, respectively. The $z = 2$ star forming main sequence from Daddi et al. (2007) is shown as the area between the two black dashed lines. The tracks evolve on this sequence until the cooling mode is changed. Then they lose the majority of their active star formation and arrive at sSFRs of $10^{-11} - 10^{-12}{\rm yr}^{-1}$. These values are in agreement with massive galaxies in the SDSS observations. The dashed lines in the respective colors show the evolution of the galaxies without a switch into quiescence mode. In this case, the sSFRs decrease more slowly and don't arrive at the low values necessary to match the SDSS sample.

We note that models such as Dutton et al. (2015b), although similar in other respects, will not be able to reproduce the sSFR as our model does. Their model has zero SF after $z = 2$ and, thus, predicts no absolute value for the sSFR at late times. As shown in Fig. 3.7, of the order of 25% of our final stellar mass is formed after the cooling mode switch. This amount of SF is in agreement with the SDSS measurements of the present-day sSFR of massive ellipticals.

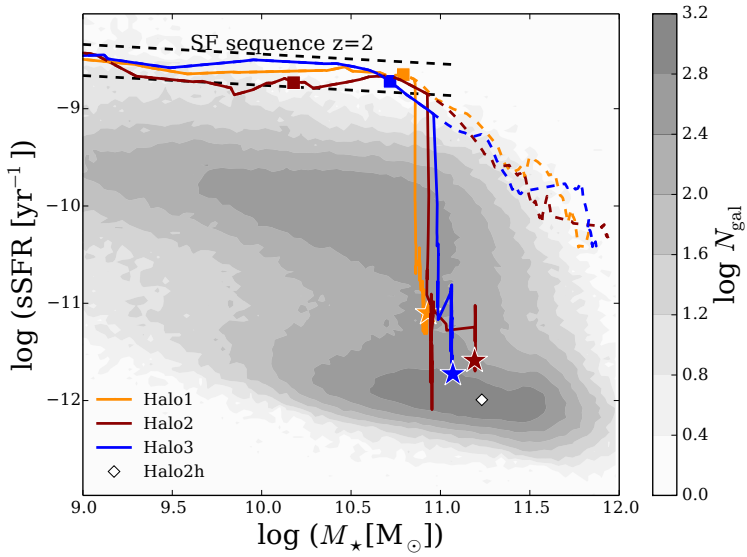

Figure 3.8. Specific star formation rate (sSFR) versus stellar mass. The full lines show the evolution of our galaxies after cooling is turned off. Dashed colored lines show the evolution of our galaxies if not change is made to the cooling. The evolution direction is downwards, where squares show the position at $z = 3$ and stars the position at $z = 0$. We plot the $z = 0$ position of our high resolution version of Halo2 at a white diamond, which can be compared to the dark red star. The gray contours are SDSS data with $z < 0.2$. The stellar masses follow the calculation by Kauffmann et al. (2003) and Salim et al. (2007). The sSFR follow Brinchmann et al. (2004). We also plot the extent of the star forming main sequence at $z = 2$ from Daddi et al. 2007 as two black, dashed lines.

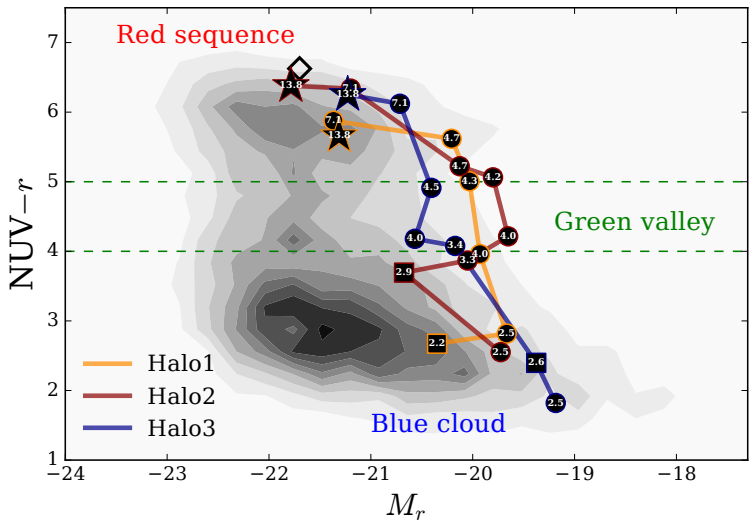

Figure 3.9. We present the color - magnitude diagram with SDSS and GALEX data for $z < 0.22$ as in Salim et al. (2007). We follow our galaxy by calculating the magnitudes with the radiative transfer code `SUNRISE`. The black numbers indicate the cosmic time in Gigayears at each point. Square points show the time at which the cooling mode is switched.

3.3.4 Color magnitude diagram - The green valley

The relatively sparse number of galaxies populating the color magnitude diagram between the blue cloud and the red sequence, a.k.a. the green valley, presents a difficulty in understanding the transition from blue, star forming galaxies to red-and-dead galaxies. In this work, we will use the term green valley to describe the region of the UV-optical diagram between $4 < \mathrm{NUV} - r < 5$, following Salim (2014). Other authors have defined it in different ways, which we note might lead to variations to the results we present here. This difficulty lies in the expected time it takes for a chromatic and morphological transition.

SDSS/GALEX data ($z < 0.22$, see Salim et al. 2007) obtain an estimate of approximately 1 Gyr for the transition. To compare our galaxies's evolutionary paths across the green valley, we run the radiative transfer code `SUNRISE` to take the dust extinction and induced reddening into account. We obtain mock fluxes of the Sloan r-band and the GALEX near ultra-violet (NUV) filter at a few redshifts. The derived magnitudes are rest-frame magnitudes inside our `SUNRISE` box of 50 kpc × 50 kpc.

The resulting tracks across the CMD are shown in Fig. 3.9. The grey contours are the SDSS/GALEX density map. The lines constitute the tracks of our three galaxies, while the black dots show the points at which a radiative transfer calculation was made. The number in the dots denotes the time in Gigayears at each point. Halo2 (dark red line) transits the green valley between $t = 3.3$ Gyr and $t = 4.2$ Gyr. Consequently, it transits the green valley in approximately 0.9 Gyr. Halo3 (blue line) crosses in ~ 1.1 Gyr, while Halo1 (dark yellow line) has an even shorter transit time of ~ 0.3 Gyr. Finally, since we have a finite number of simulations outputs, we approximate the error on the crossing times with the average time between two consecutive snapshots, which is around 0.2 Gyr.

The `SUNRISE` dust model affects the resulting magnitudes most strongly during ongoing SF, because new stars are assumed to stay enshrouded in their birth cloud for up to 10 Myr. Without SF, the dust mass scales with the gas metallicity. This effect is important after the cooling switch, since much gas is initially still in the central galaxy. With time, the effect decreases since gas, and hence dust, is expelled due to feedback. It is worth noting that our galaxies do not cross the green valley along the area of highest density in the observations, which would be around $M_r \sim -22$. Instead, they cross around $M_r \sim -20$ and become brighter after transiting the green valley. Since there is little SF at late times, this brightening is caused by the loss of dust in the galaxy. Decreasing cold gas fractions in the center cause the estimated dust extinction to decrease when more gas is heated and held in the hot halo outside of the galaxy.

We acknowledge that there are many parameters in the `SUNRISE` model that could change the resulting magnitudes, i.e. the grid cell size and the dust grain size among others. Due to the simplicity of our starvation model, we did not see the need to fine tune these. The important result of

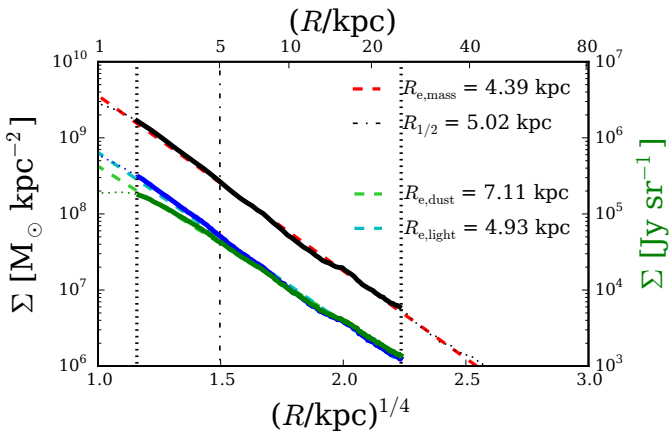

Figure 3.10. Surface density (black solid and black dotted line) and surface brightness profiles for Halo2h. The surface brightness profiles are derived from `SUNRISE` images with dust (green solid and dotted line) and without dust (blue solid and dotted line) and scale with the y-axis on the right. Each profile is fit with a de Vaucouleur profile, which are shown a thick dashed lines in red (density), cyan (brightness without dust) and light green (brightness with dust). The vertical black dotted lines show the range of the fit, which is between three smoothing lengths (1.8 kpc at this resolution) and 25 kpc, which is the extent of the `SUNRISE` image. The effective radii of the fits are shown in the legend. The vertical black dot-dashed line shows the position of the half-mass radius derived through integration and its value is also shown in the legend.

this exercise is that the relative change in color (here the NUV-r) happens in less than 1 Gyr. We expect this relative result to be less affected by the specific model parameters.

Moreover, our model is just one quenching scenario to rapidly cross the green valley. Authors such as Smethurst et al. (2015) and Trayford et al. (2016) show that different galaxy populations might well quench through a variety of mechanisms that happen with differing timescales. Some proposed causes of reddening and morphological change are secular evolution, major mergers and AGN.

3.3.5 Sizes and profiles

Matching the sizes of elliptical galaxies in simulations has been notoriously difficult, generally producing too compact centers. This difficulty might in part be related to the task of measuring the size in a comparable manner. Fig. 3.10 shows the `SUNRISE` surface brightness profile in radial annuli

(green with dust and blue without). The cyan and light green dashed lines shows de Vaucouleur (Sersic profile with $n = 4$) fit to the surface brightness profile and the resulting effective radius is shown in the legend. The fit is performed in the radial range from 3 smoothing lengths ($\epsilon_{\rm gas} \sim 3.3\,$kpc for the fiducial resolution) out to 25 kpc. The fitting range is shown between the vertical dotted lines. We compare the light profile with the mass profile by projecting the galaxy onto the same axis as the `SUNRISE` image, resulting in a surface mass density profile. The same fit is performed and shown as a red dashed line. The dot-dashed line shows half-mass radius, $R_{1/2}$, obtained from the integrated stellar mass profile as indicated in the legend.

Fig. 3.11 shows the $z = 0$ sizes of all three galaxies using all four of the above measures. The filled squares are the half-mass sizes when considering the integrated mass profile, $R_{1/2}$. The gray and open diamonds are the effective radius from the fit to the surface brightness profile with and without dust, $R_{\rm e,light}$ and $R_{\rm e,dust}$ respectively. The open star symbols are the sizes derived from the surface density profiles, $R_{\rm e,mass}$. We compare these with the fitting function (black dashed line) from Dutton et al. (2013) who used SDSS early-type galaxies within the redshift range $0.005 < z < 0.3$ and a median redshift of ~ 0.1 to produce the average as well as the 16^{th} and 84^{th} percentiles (grey area) of the observational sample. The observed relation from Nipoti et al. (2009) who used the SLACS sample of local early-type galaxies is shown as a black dotted line.

The extent of Halo1 and Halo2h are in good agreement with the observational data. Halo3 has a dense stellar core which decreases the integrated mass profile and is too compact to be consistent with a de Vaucouleur in the center. The profile of Halo2 is different from its high resolution counterpart due to an incoming merger. We are only able to fit the central part of the profile ($< 10\,$kpc) and, thus, get a steeper slope and smaller size. The integrated mass profile for both Halo2 (dark red) and Halo2h (black) are well within the observational constraints. The similarity of the high resolution Halo2h with the lower resolution Halo2 sizes gives confidence to the results of our fiducial resolution simulations. Given this simple quiescence model, the agreement between the simulation and observations is encouraging.

3.3.6 Faber-Jackson relation

The stellar mass - stellar velocity dispersion relation is one projection of the fundamental plane of elliptical galaxies. Elliptical galaxies have on average higher velocity dispersions than star-forming galaxies. This kinematical change is likely linked to the quenching mechanism and therefore provides a critical constraint for quenching models.

Fig. 3.12 shows where on the relation our three galaxies fall at $z = 0$. Lines in the appropriate color show the tracks of each galaxy up to $z = 0$. To portray the observational relation, we show the analytical fit to SDSS

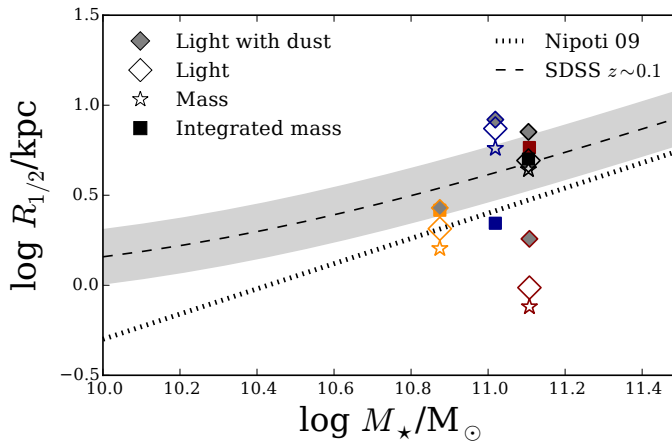

Figure 3.11. Size-mass relation for our three fiducial galaxies. The filled squares show the half-mass radii calculated from the integrated mass profile. The diamonds show the effective radii derived from the de Vaucouleur fits on the `SUNRISE` profiles with and without dust in grey and unfilled, respectively. The open stars are the effective radius from the de Vaucouleur fits to the surface density profiles. Each galaxy is shown it its respectively color (Halo1 in orange, Halo2 in dark red, Halo3 in blue). The black symbols indicate the high resolution galaxy Halo2h. The black dashed line and grey band are the analytic fit of the $z \sim 0.1$ SDSS data by Dutton et al. (2013). The black dotted line shows the fit by Nipoti et al. (2009).

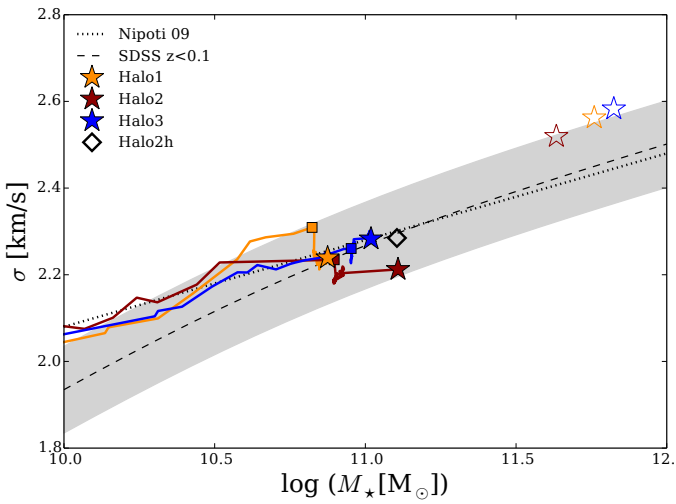

Figure 3.12. Stellar mass - stellar velocity dispersion with the observational data (SDSS z=0.1) fit by Dutton et al. 2013 (black dashed line). The 16th and 84th percentiles are shown as a grey shaded area. The star markers are our galaxy at z=0. The black diamond shows the $z = 0$ position of Halo2 in high resolution. Open stars show the $z = 0$ value for the simulations (in the corresponding color) without changing the cooling mode (overcooled). Filled squares indicate the stellar mass at the point at which cooling is switched off. The marginal evolution after this point suggests that the galaxy was already bulge-dominated at the time of $M_{\rm off}$.

early-type galaxies ($z < 0.1$) from Dutton et al. (2013) as a black dashed line and the scaling relation derived by Nipoti et al. (2009) (using SLACS early-type galaxies at $z = 0$) as a black dotted line.

Both Halo1 and Halo3 fall directly on the mean today, while Halo2 lies slight below but still inside the scatter. The high resolution version of Halo2 sits on the mean. The simulations without a change in the cooling mode produce $z = 0$ velocity dispersion values too high for their given stellar mass, as shown with the open star symbols. This is corrected with our simple quiescence model.

3.4 Summary

In this chapter we have critically examined the properties exhibited by massive galaxies whose star formation is quenched entirely by starvation. The starvation is initiated by means of a simple quiescence model in which all halo gas above a threshold temperature is prevented from cooling. This is a simple way to simulate the effects of star formation fading away. Existing stars drive winds and end as supernovae, removing cold gas from the galaxy. The cold gas reservoir is depleted over time because it is: 1) turned into stars or 2) heated. Each cycle of star formation heats a varying fraction of the star forming gas to above the temperature threshold. The threshold temperature, $T_{\rm off}$, and halo mass at which the switch is initiated, $M_{\rm off}$, are chosen to match the halo mass - stellar mass relation derived by abundance matching.

Over time, this causes less and less gas to be available for future cycles of star formation. Since we switch to this cooling mode at the height of SF (SFR$\sim 10^2$ M$_\odot$yr^{-1}), the initial effect is large and SF drops quickly (to SFR~ 10 M$_\odot$yr^{-1} in ~ 1 Gyr). Later, the SFR slowly settles down to a value of ~ 1 M$_\odot$yr^{-1}.

The resulting galaxy properties are compared to an array of observations. The SFRs follow the downward trend after the height of SF at around $z = 2.5$. But they are about 1 dex too low at intermediate times ($z = 2 - 0.5$). We vary the parameter $M_{\rm off}$ to show that a galaxy-to-galaxy scatter in the quenching time may smooth the knee of the SFH derived from abundance matching. Since we do not include other galaxy types, we don't expect it to be able to represent the overall envelope. The sSFR evolution with increasing stellar mass initially follows the $z = 2$ SF main sequence and then drops to low values (sSFR$\sim 10^{-12}$ yr^{-1}) in accordance with the SDSS values for the quenched population at $z = 0$.

A key insight of this chapter is that allowing star formation to fade by starvation can produce green valley crossing times of well below 1 Gyr, contrary to common assumptions of the opposite. We were able to show this by performing radiative transfer post-processing on the evolving galaxies and estimating their mock r-band and NUV fluxes. These were used to construct evolutionary tracks across the CMD and estimating crossing

times. The three galaxies presented in this work deliver crossing times in the range $0.3 - 1.1\,\mathrm{Gyr}$. The swiftness of the chromatic transformation is surprising and we conclude that the quenching process does not require a single event that instantaneously rids the galaxy of its gas reservoir. Rather a gradual process in which the gas is heated and made unavailable for SF is sufficient to produce the required transformation. Although we note that this result is dependent on our quenching model, and also on the dust modelling in `SUNRISE`.

We recognize that this model is too simple to delve further into the properties of these elliptical galaxies. Nonetheless, when we compare the mass profiles and resulting sizes of our galaxies with the observed elliptical population at $z = 0$, they match surprisingly well. The two galaxies with smaller stellar masses might be slightly too compact, depending on the method of calculating the sizes. Dust affects the sizes to some degree, making them slightly larger due to the decreased brightness in the central regions of the galaxies. Also the velocity dispersion at $z = 0$ matches observations, signifying that the stellar kinematics correctly change with the morphological transformation. In future work, more physically motivated models of quenching will be able to further understand the transformation of galaxies into ellipticals at $z = 0$.

4

The circum-galactic medium and outflows[†]

Through the phenomenological model presented in the previous chapter, it is apparent that stellar feedback is a vital ingredient in forming galaxies consistent with observations. And yet, the feedback strength and the precise nature of its coupling to the gas are not well understood. Since the temperature, density and chemical enrichment of the gas in the halo surrounding a galaxy is equally affected by the strength of feedback, it is instructive to compare the simulated circum-galactic medium (CGM) with the observed CGM. To attempt this, we study the hot and cold CGM of 86 galaxies of the cosmological, hydrodynamical simulation suite NIHAO. NIHAO allows a study of how the $z = 0$ CGM varies across 5 orders of magnitude of stellar mass using OVI and HI as proxies for hot and cold gas.

4.1 Introduction

The gas surrounding galaxies, the CGM, plays a major role in galaxy formation and evolution. Gas flows into the bottom of potential energy wells and turns into stars to create galaxies. As gas falls into galaxies, the mass of the dark matter halo determines its velocity and the gas heats to the virial temperature. Rees and Ostriker (1977) showed that the cooling time of the CGM gas determines how much gas cools onto the galaxy, which corresponds to the mass scales at which galaxies form.

Theorists are still working out the details of the geometry of that collapse. White and Rees (1978) included dark matter in the collapse and introduced the idea of hierarchical merging to form the most massive halos. Kereš et al. (2005) pointed out that when galaxy masses are low, gas first

[†] The contents of this chapter was published in similar form in Gutcke et al. (2017b)

cools onto filaments before flowing into galaxies along those narrow paths. Birnboim and Dekel (2003a) showed that as the galaxy increased in mass, those filaments would shock near the virial radius and the CGM would cut off the cold gas supply to the galaxy. The shocking of accreting gas is one of the many attempts at an explantation of why star formation becomes so inefficient in galaxies more massive than the Milky Way.

In such models, a large fraction of the baryons in galaxies around and above $10^{11.5}$ $M_\odot$ in halo mass is distributed in the CGM. However, since it is spread out over such a large volume it is diffuse enough that it does not emit much radiation. What radiation is emitted comes out at hard to observe energies like X-rays (see e.g. White and Frenk 1991; Crain et al. 2010). It is thus incumbent on modelers to make predictions about the chemical phase, orientation and shapes of the CGM in their models.

Fortunately, observers can detect diffuse gas in absorption if a bright source like a quasar lies behind it. Many absorption lines useful for diagnostics are in the UV portion of the spectrum. Thus, it is easiest to study the CGM at high redshifts, such that the lines redshift into the optical portion of the spectrum (e.g. Cowie and Songaila 1995; Schaye et al. 2003; Hennawi et al. 2006; Steidel et al. 2010; Rudie et al. 2012; Lehner et al. 2014).

UV spectrographs were added to the *Hubble Space Telescope* (HST), enabling studies of the low redshift CGM (e.g. Thom and Chen 2008; Tripp et al. 2008; Prochaska et al. 2011; Danforth et al. 2014). In particular, the Cosmic Origins Spectrograph (COS), adding far-UV sensitivity, represented a game changer in studies of the low redshift CGM. The COS-Halos project focused on studying the CGM surrounding a large sample of $\sim L^\star$ galaxies (Tumlinson et al. 2013), where $L^\star$ denotes the luminosity of a galaxy that lies on the "knee" of the galaxy luminosity function. COS-Halos studied OVI as one of its highly ionized species. Oxygen is collisionally ionized to OVI in gas between $10^5 < T/K < 10^6$. It is also possible for lower temperature gas to be photo-ionized to OVI by an external radiation field. Oxygen is produced primarily in type II supernovae (SNII) and can flow out of the galaxy with the galactic wind. Thus, OVI can be either a tracer of warm/hot gas in the CGM or a cooler phase that may have flowed out in the wind.

Tumlinson et al. (2011) found OVI detections (their column density detection limit being $N_{\rm OVI} \gtrsim 10^{14}{\rm cm}^{-2}$) in the majority of their 30 observed star forming galaxies, but in none of their sample of red galaxies. In galaxies with OVI detections, it was extended in projection out to 300 kpc, beyond even the virial radius. Assuming typical values for the metallicity ($0.5\ Z_\odot$), abundance ratios (solar), and ionization field shining on the CGM, Tumlinson et al. (2011) and Peeples et al. (2014) found high oxygen masses in the CGM, comparable to the amount of oxygen found in the Milky Way disk.

Detailed examination of the absorption line profiles showed hints of components with narrow lines embedded inside broader overall profiles

(Tripp et al. 2008; Thom and Chen 2008). These tentative findings hint towards OVI being cooler than expected by collisional ionization models and generally more consistent with being photo-ionized.

One surprising result of COS-Halos was that a large fraction of the CGM mass is cool and in a low ionization state. The gas also appears to be in dense knots that are not in hydrostatic equilibrium with their surroundings (Werk et al. 2014). How such gas is supported in the CGM remains a mystery.

Local $L^{\star}$ galaxies are not the only place a surprising amount of cool gas has been found (for other places, see Rudie et al. 2012; Martin et al. 2012; Prochaska et al. 2013; Crighton et al. 2013).

Several studies have looked at the HI covering fraction at a variety of masses throughout cosmic time (Rudie et al. 2013; Prochaska et al. 2014). Commonly, they report the fraction of sight lines in which HI is detected. Fumagalli et al. (2014) provides a nice summary. While models generally predict that the CGM of luminous galaxies (in modelling generally assumed to be the more massive galaxies) is comprised of more hot gas, the observations find higher HI covering fractions of the CGM surrounding more luminous galaxies.

Some work has also been focused on understanding the geometrical extent of the CGM. Bordoloi et al. (2014) present an investigation of the geometry of cool outflows traced by MgII in the absorption line spectra of 486 zCOSMOS galaxies. Splitting their sample by inclination, they find a higher equivalent width out to 40-50 kpc for galaxies with near face on inclination than for edge on galaxies. They take this to be indicative of bipolar outflows perpendicular to the plane of the disk, since absorption spectra will capture the outflowing component face on more strongly than edge on. Kacprzak et al. (2015), using OVI absorption lines, present a bimodality in the azimuthal angle distribution around 53 HST-imaged galaxies. They conclude that this bimodality is consistent with minor-axis driven outflows and that OVI is not mixed throughout the CGM.

4.1.1 Numerical predictions and observations

Galaxy formation models have used star formation feedback in an attempt to explain the low efficiency of star formation in galaxies (Springel and Hernquist 2003; Murray et al. 2005; Oppenheimer and Davé 2006; Dalla Vecchia and Schaye 2008; Davé et al. 2011; Hopkins et al. 2012; Puchwein and Springel 2013; Vogelsberger et al. 2013; Kannan et al. 2014). Stellar-driven winds could not only deplete the central galaxy of gas, its fuel for star formation, but also transport metal-enriched gas to large distances from the stars (e.g. Aguirre et al. 2001; Theuns et al. 2002; Davé and Oppenheimer 2007; Cen and Chisari 2011; Christensen et al. 2015).

Numerical simulations commonly use one of two prescriptions to model outflows: kinetic (Springel and Hernquist 2003; Davé and Oppenheimer 2007; Oppenheimer et al. 2010; Ford et al. 2015; Suresh et al. 2015) and

thermal (Stinson et al. 2006; Dalla Vecchia and Schaye 2012; Shen et al. 2012; Hummels et al. 2013; Schaye et al. 2015; Rahmati et al. 2015). The kinetic model uses a prescription for wind velocities launched from disks. Thermal models make gas around star formation regions hot and allow the supersonic pressure of the hot gas to push gas out of galaxies. Durier and Dalla Vecchia (2012) find that kinetic wind and thermal models converge to the same behavior using correct hydrodynamics.

Kinetic wind models typically turn off hydrodynamics of the wind particles, including the recent *Illustris* simulations presented in Vogelsberger et al. (2014). However, Schaye et al. (2010) implement a wind model without hydrodynamical decoupling. Early studies suggested that without hydrodynamics, such wind prescriptions preserved convergence in results of different resolutions. It is unclear whether such convergence remains in the most recent studies (Vogelsberger et al. 2013).

Many simulated galaxies now broadly match the low redshift stellar mass-halo mass relation (Oppenheimer et al. 2012; Aumer et al. 2013; Stinson et al. 2013; Hopkins et al. 2014; Vogelsberger et al. 2014; Christensen et al. 2015; Schaye et al. 2015; Wang et al. 2015). It is thus worth making a comparison with observations that could lend insight into how the CGM formed and whether it is the repository for the missing baryons in the Universe.

OVI. Hydrodynamical simulations that compare their OVI (e.g. Hummels et al. 2013; Ford et al. 2015; Suresh et al. 2015) with COS halos observations (Tumlinson et al. 2011) find that their fiducial models produce nearly a dex lower column densities across impact parameters and, when compared, also across luminosities, than the observations.

Our earlier look using a thermal model (Stinson et al. 2012, henceforth S12), showed good agreement with OVI observations, although this was a small sample of two galaxies. The purpose of this work is to expand that sample.

Using an Eulerian grid code, Hummels et al. (2013) studied variations of the CGM with thermal stellar feedback strength. While they were able to match many ion species column densities, they found that OVI presented the biggest challenge. Various strengths of their thermal feedback scheme changed the typical OVI column densities by a half an order of magnitude and the extent of the OVI halo by an order of magnitude. These changes can be attributed to changes in star formation rates due to the availability of gas reservoirs, but also to the differences in outflow strength which effect the metallicity distribution. The feedback prescription in which cooling was suppressed produced results most consistent with observations. Even in that simulation, the simulated OVI column densities remain about half a dex too low. In terms of radial extent, the cooling suppressed feedback also extends as far as the observations. Plenty of oxygen was present in their gaseous halos, but the temperature range for OVI is small enough

that not much gas stayed in that state, assuming collisional ionization dominates.

Focusing on the effect of feedback, Rahmati et al. (2016) used the EAGLE simulation suite to compare their simulated column density distribution functions (CDDFs) of a variety of elements in various ionization states, including OVI, with observations. They find that the shape and normalisation of the CDDF of OVI both strongly depend on the stellar feedback efficiency due to its effect on the amount of metals produced. But they note that OVI is directly dependent on the strength of the feedback, presumably because the temperature structure effects how much OVI is collisionally ionized

Concentrating on OVI, Suresh et al. (2015) make a detailed study of the offset between the CGM from the *Illustris* simulation and observations. In addition to the nearly order of magnitude offset in column densities, they note that their simulations show a strong correlation between galaxy stellar mass and OVI column density. Their galaxies also show steep column density gradients. Additionally, they model local photoionization to explain the low OVI column densities in simulations, but only find an effect in the inner 50 kpc of the CGM.

Most recently, Oppenheimer et al. (2016) tested a non-equilibrium ionization (NEQ) and cooling module using EAGLE zoom simulations. They find that the NEQ does not effect the oxygen ion abundances by more than ~ 0.1 dex. Their fiducial model shows a factor of two too low OVI column densities compared to observations. They argue that the NEQ effects are strongest in shocks and in gas that is exposed to sources fluctuating on a short timescale such as an AGN.

Since S12 did well matching OVI observations, another look with a newer, larger sample of galaxies is worthwhile. The study will allow for a comparison with the trend with stellar mass that Suresh et al. (2015) found.

HI. To begin to understand the large amounts of cool gas surrounding galaxies, Fumagalli et al. (2014) found that the HI covering fractions of their simulated halos with $M_{\rm vir} < 10^{12}$ $M_\odot$ were lower than $z = 2-2.5$ observations by a factor of $\sim 30\%$. Moreover, for the halos with $M_{\rm vir} > 10^{12}$ $M_\odot$ they found systematically lower values (factor ~ 3). However, the feedback prescription used in this work was not effective enough, overproducing the amount of stars and underestimating the amount of gas in the halos. It is worth pointing out that this study presented a compilation of previous results. The simulations with some of the highest covering fractions came from the *Eris* simulation (Shen et al. 2012), a simulation run with the same code and cooling modules we use.

Using the FIRE simulation suite, Faucher-Giguère et al. (2015) also studied covering fractions of HI. They found that the physical area the cold gas covers stays roughly constant with cosmic time. Thus, as the virial radius grows, the covering fraction decreases significantly. When

they compared with $z \sim 2 - 2.5$ observations they seem to better match the $M_{\rm vir} < 10^{12}$ $\rm M_\odot$ halos but they were still too low for the most massive systems. Originally, these authors claimed that the reason for this could be that their simulations did not include AGN feedback.

In a recent study, Rahmati et al. (2015) examine the HI covering fractions using the EAGLE simulation suite. They approximate the HI ionization fraction via the same fitting functions as we do (Rahmati et al. 2013) and find close agreement between the Prochaska et al. (2013) and Rudie et al. (2012) observations. They attribute this to their strong stellar and AGN feedback model, although they say that their AGN feedback prescription has a small effect. Their comparison, however, is for larger mass halos, $M_{\rm vir} > 10^{12.5}$ $\rm M_\odot$, captured within their larger simulation volume with an initial gas particle mass of 1.4×10^6 $\rm M_\odot$.

Even more recently, Faucher-Giguere et al. (2016) argue that, in fact, they can reproduce the observed HI covering fractions for the massive systems without AGN feedback when including strong stellar winds. Their simulations have a gas particle mass of a few times $10^4\,\rm M_\odot$. This highlights the fact that there is still no general agreement about the HI covering fractions around massive high-redshift galaxies between different state-of-the-art feedback models.

Aim of this analysis. In this chapter we plan to investigate the CGM properties and characterise the metallicity distribution and shape in Numerical Investigation of a Hundred Astrophysical Objects, NIHAO (Wang et al. 2015) project. The NIHAO simulations are a suite of nearly 100 hydrodynamical, cosmological zoom-in galaxies across a range in mass from $10^5 \lesssim M_\star/\,\rm M_\odot \lesssim 10^{11}$. The star formation and stellar feedback was developed in the Making Galaxies in a Cosmological Context project (MaGICC Stinson et al. 2013). The NIHAO project builds on this, extending the mass range while keeping the same stellar physics at all scales. Despite the many orders of magnitude between our smallest and largest galaxy, the amount of stellar mass formed in a halo with a given mass agrees with results from abundance matching (Wang et al. 2015). The cold gas mass in the simulated galaxy disks also agree well with observations (Stinson et al. 2015). It is for this reason that the NIHAO sample is an excellent resource for exploring the physics of galaxy formation.

Focusing on the halo mass dependence of properties of the CGM, we will mainly look at low redshifts. This work is an extension of S12 to a large sample of galaxies spanning a wide range in masses. We examine the hard-to-see low density gas surrounding galaxies, in the ensemble of the NIHAO galaxies.

§2 provides an overview of the simulations used to find this result. §3.1 shows the hot gas traced by OVI and how the profiles compare with observations. §3.2 discusses the cold gas density profiles traced by HI and takes a look at the covering fractions of HI, comparing them to observations. §3.3 studies how outflows shape different phases of the CGM. §3.4 looks at

the chemical composition of the CGM. §4 provides context for the findings in some recent theoretical models, observations of gas in galaxies, and some possible implications for future observations.

4.2 Simulations

The 86 simulations analyzed in this chapter are taken from the NIHAO project (Wang et al. 2015). The NIHAO galaxies come from $(15\ h^{-1}\ \mathrm{Mpc})^3$, $(20\ h^{-1}\ \mathrm{Mpc})^3$ and $(60\ h^{-1}\ \mathrm{Mpc})^3$ cubes from Dutton and Macciò (2014). For all work done here, we use the Planck Collaboration et al. (2014) cosmological parameters: Ω_m=0.3175, Ω_Λ=0.6825, Ω_b=0.049, $H_0 = 67.1$ km s^{-1}Mpc^{-1}, $\sigma_8 = 0.8344$. The virial mass, M_vir, of each halo is defined as the mass of all particles within a sphere containing $\Delta = 200$ times the cosmic critical matter density. The virial radius, R_vir, and the virial temperature, T_vir, are defined accordingly.

4.2.1 Calculating HI *fractions*

Unlike S12, which used an optically thin CLOUDY calculation to compute the HI neutral fraction, we use an analytic fits to radiative transfer calculations presented in Rahmati et al. (2013). Rahmati et al. (2013) post-processed SPH simulation using the radiative transfer code TRAPHIC detailed in Pawlik and Schaye (2008) and Pawlik and Schaye (2011). They show that the fitting functions, which include self-shielding density thesholds dependent on density and redshift, produce results in excellent agreement with their full radiative transfer calculations.

The CLOUDY calculation used in S12 found hydrogen ionization fractions as high as 0.3 even at densities above 0.1 cm^{-3}.

Table 2 in Rahmati et al. (2013) presents self-shielding density thresholds at discrete redshifts and for different cosmic ionization backgrounds. We calculate the self-shielding density threshold by interpolating between the redshift values for the Haardt and Madau (2001) cosmic ionizing UV background. The Rahmati et al. (2013) density threshold rises from 1.1×10^{-3} cm^{-3} at $z = 0$ to 8.7×10^{-3} at $z = 2$ before decreasing to higher redshifts.

4.3 Results

Our study of the CGM starts with a visual inspection of warm and cool gas in ionization lines that are commonly observed, OVI and HI. For the higher mass galaxies, we compare these with observations. Then we investigate trends of the shape and extent of the CGM as a function of total galaxy mass.

In Fig. 4.1 we show a $z = 0$ slice of one (arbitrary) NIHAO galaxy viewed side-on (thickness = 2 kpc) to give us a qualitative impression of gas flows in the halo. The gray shading represents gas density inside the

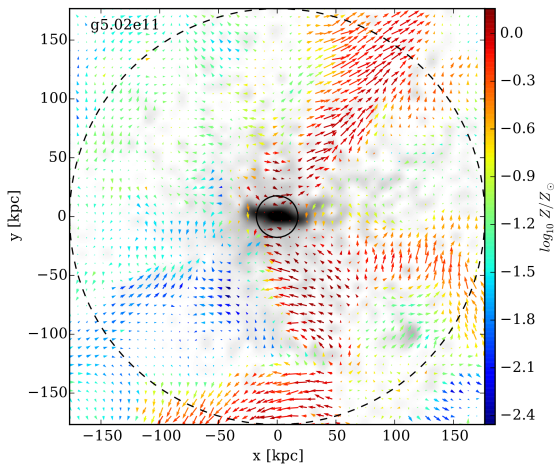

Figure 4.1. Edge on view of the velocity field in slice $R_{\rm vir} \times R_{\rm vir} \times 2\,{\rm kpc}$ for one NIHAO galaxy at $z = 0$, g5.02e11. Colors indicate the average metallicity, $\log Z/{\rm Z}_\odot$, while the grey shaded areas show mean gas density in the slice. The virial radius and 10% of it are shown by the dashed and solid circles, respectively. Metal-rich inflows and outflows can be traced approximately perpendicular to the plane of the disk.

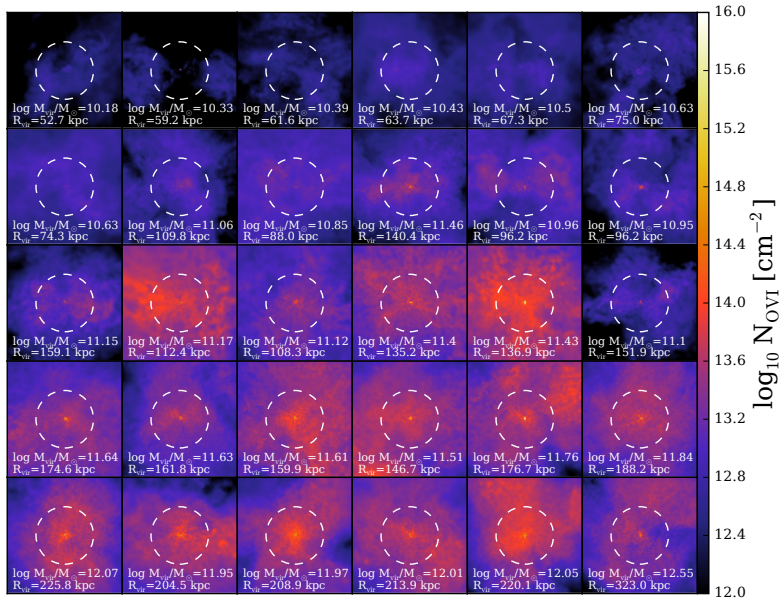

Figure 4.2. OVI column density maps for the same 30 NIHAO galaxies as in Wang et al. (2015). The CGM images are oriented such that the disks are face-on. Each image is $2R_{\rm vir}$ on each side, while the dashed white circle indicates the virial radius.

slice. We overlay the gas velocity field directions as arrows. Arrow length scales with velocity and arrow color shows the average metallicity of the gas in units of solar metallicity. The dashed black line encompasses the virial radius. Large, metal-rich ($\log Z/Z_\odot > -0.4$) inflows are visible in the lower right hand corner, while at the same time metal-rich outflows are being driven in the upper right hand corner.

4.3.1 Hot gas

Although this analysis uses 86 galaxies of the NIHAO suite, Fig. 4.2 shows column density maps of OVI for the same 30 NIHAO galaxies shown in Wang et al. (2015). The OVI mass is calculated per particle as in S12 using 1 cm thick gas slabs in Cloudy (v10.0 last described in Ferland et al. 1998). The gas is radiated with a Haardt and Madau (2005) UV radiation field evaluated at $z = 0$. The resulting OVI mass is smoothed using the smoothing kernel and then the images are created as projections of the OVI mass through the entire zoom region, a ~ 4 Mpc line-of-sight.

The 30 OVI maps in Fig. 4.2 are ordered by $M_{\rm vir}$ and range from $\approx 10^{10}$ to 10^{12} $M_\odot$. The x and y axes are scaled to show the gas halos out to

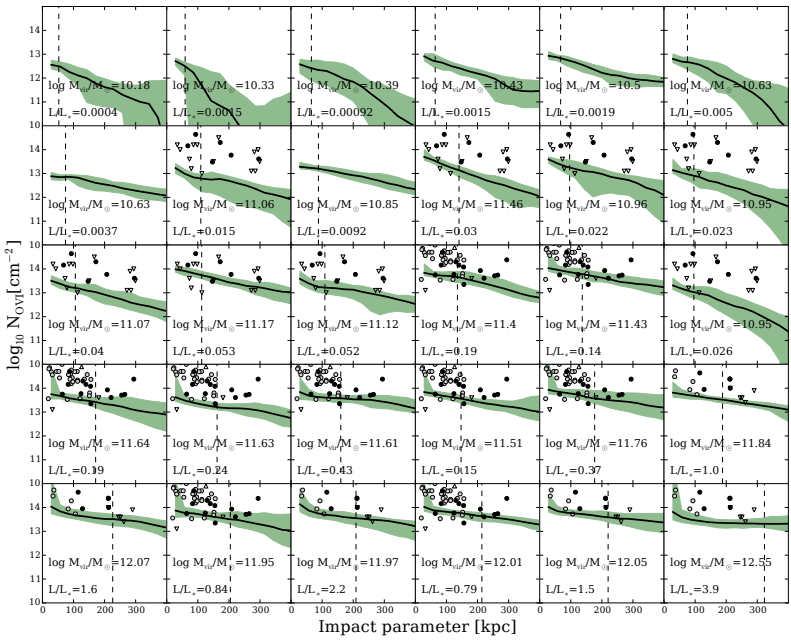

Figure 4.3. Mock sightline distributions of OVI column density for the same 30 NIHAO galaxies as in Fig. 4.2 and Fig. 3 and 4 of Wang et al. (2015). Black solid lines indicate the median column density for a given impact parameter bin. The green-gray shaded area represents the 5-95 percentile range. Observational data from Prochaska et al. 2011 (black symbols) and Tumlinson et al. 2011 (white circles). The Prochaska et al. 2011 data is split into three groups: $0.01L^\star < L < 0.1L^\star$, $0.1L^\star < L < 1L^\star$ and $L > 1L^\star$. Only the relevant group is overplotted according to the luminosity of the shown galaxy.

$2R_{\rm vir}$. Qualitatively, Fig. 4.2 shows the OVI column and its extent scales with $M_{\rm vir}$: the small galaxies are practically devoid of OVI, while more massive galaxies show observable OVI column densities out past $2R_{\rm vir}$. To compare the galaxies with observations, we use the column density maps as though each position was a QSO sightline to make a sample of thousands of sightlines (see Fig. 4.3).

Since the observed samples necessarily combine observations from a variety of galaxies, Fig. 4.4 and Fig. 4.5 show combinations of column density profiles of all 86 simulated galaxies. All the sightlines from each group of simulations are combined. Fig. 4.4 shows the median OVI column density as a function of impact parameter b normalized to each respective virial radius (left panels). The impact parameter directly is shown in the left panels of Fig. 4.5 as the black solid line. The green-gray shaded area

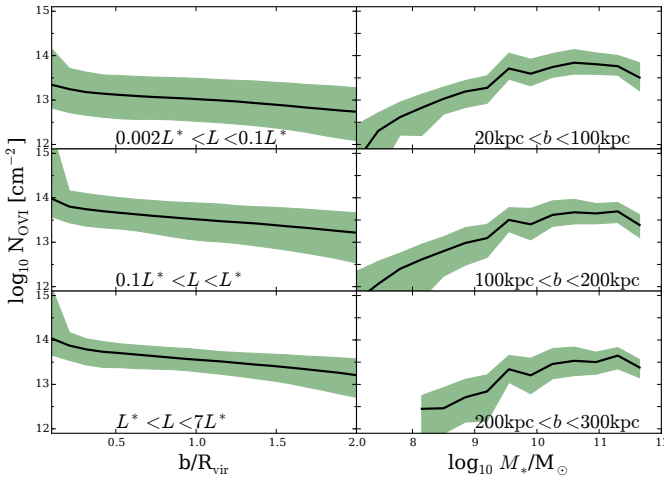

Figure 4.4. OVI column density ($z = 0$) as a function of: impact parameter normalized to the virial radius (left panels) and stellar mass (right panels). All sight lines from face-on and edge-on for every NIHAO galaxy are included. The black solid line shows the median column density at $z = 0$, while the green band shows the 5-95 percentile range. In the left panels, the column densities are divided between three luminosity bins: $L < 0.1L^{\star}$ (upper panel), $0.1L^{\star} < L < 1L^{\star}$ (middle panel) and $L > 1L^{\star}$ (lower panel). In the right panels, the column densities are divided between radial bins: $20 < b/\mathrm{kpc} < 100$ (upper panel), $100 < b/\mathrm{kpc} < 200$ (middle panel) and $b > 200$ kpc (lower panel).

shows the 5-95 percentile range of our data. The functional form of the combined profiles in Fig. 4.5 is very similar to the individual galaxy profiles seen in Fig. 4.3. This indicates that the galaxy-to-galaxy variations are small and that the combined trends mainly show the variation in profiles. Solely the galaxies with the smallest luminosities ($L < 0.002L^{*}$, the profiles without observational data in Fig. 4.3) show a larger galaxy-to-galaxy scatter. These are neither compared to observations, nor included in Fig. 4.5.

Observed data from galaxies of similar luminosities are overlaid on top of the simulated columns of Fig. 4.5, according to the luminosity ranges used in Prochaska et al. (2011), $0.01L^{\star} < L < 0.1L^{\star}$, $0.1L^{\star} < L < 1L^{\star}$ and $L > 1L^{\star}$. In the luminosity range $0.1L^{\star} < L < 1L^{\star}$, data from Tumlinson et al. (2011) are shown as gray circles. Luminosities are calculated for the simulated galaxies using Padova simple stellar populations (Marigo et al. 2008; Girardi et al. 2010). $\mathrm{L}^{\star}$ is taken as $\mathrm{M}_V = -21.12$ as reported in

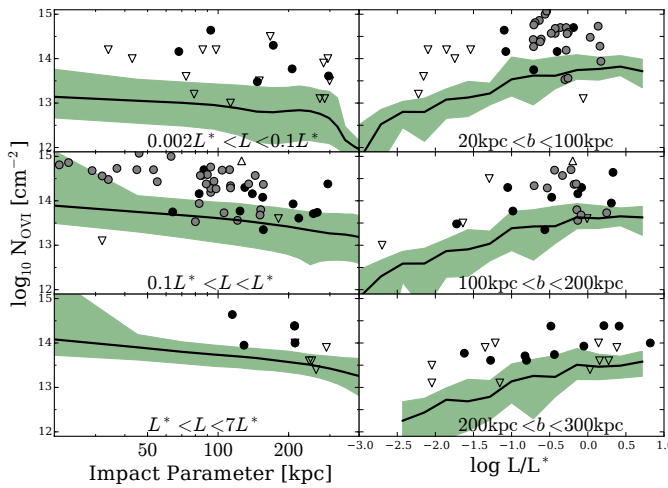

Figure 4.5. OVI column density ($z = 0$) as a function of: impact parameter (left panels) and luminosity (right panels). The simulations and binning are the same as in Fig. 4.4 above. Observational data from Prochaska et al. (2011) are shown as black circles. Tumlinson et al. (2013) data is shown as gray circles. Non-detected upper and optically thick lower limits are shown as upward and downward facing open triangles, respectively. Observational points are only shown in the lower panels, since the virial radii and stellar masses of the observations are not known.

Prochaska et al. (2011). Tumlinson et al. (2011) gives SDSS r-band galaxy magnitudes; we use $M_r = -20$ for $L^\star$. While the COS-Dwarfs project (Bordoloi et al. 2014) observed galaxies of similar luminosity as our lowest mass simulations, they have yet to publish OVI columns.

When exact data values are given, they are shown as filled black circles. Upper limits are shown as downward pointing triangles, and lower limits are shown as upward pointing triangles.

No observations are shown in Fig. 4.4 since neither the virial radii nor the stellar masses are available for the observed galaxies.

The general trend of increasing column density with increasing $M_{\rm star}$ (so also total luminosity) is apparent. For this analysis, we will focus on the $0.1 < L/L^\star < 1$ range, since many of the observations in the lower luminosity bins are only upper limits, and the sample size is mainly limited in the higher luminosity bin. In the $0.1 < L/L^\star < 1$ range, the simulations are about half a dex lower than the median of the observations. Such an offset is typical of comparisons of OVI observations with simulations (Ford et al. 2015; Hummels et al. 2013; Suresh et al. 2015). Various causes are mentioned, among them that the oxygen, which seems available in sufficient amounts, is not in the correct ionization state. Assuming collisional ionization dominates, this points to a problem with the thermal structure of the CGM produced in hydrodynamical simulations. Further discussion of this in §4.

There are two significant differences that could explain the apparent discrepancy between the NIHAO sample and analysis of S12. First, the NIHAO sample is much larger than the 2 galaxies shown in S12. In S12, only the brighter galaxy well matched the observations.

Fig. 4.6 shows that NIHAO samples the lower half of the $0.1L^\star < L < 1L^\star$ bin more than the OVI observations, which are mostly in the upper half of the bin. The right panels of Fig. 4.5 are helpful to make this comparison. They show that at common projection radii and galaxy luminosity, NIHAO galaxies indeed have lower OVI column densities.

Another difference between NIHAO and S12 is the stellar feedback. S12 used a slightly different version of hydrodynamics that required stronger stellar feedback to reduce star formation enough to fit on the stellar mass–halo mass relation. S12 and Hummels et al. (2013) showed that more stellar feedback add OVI to the CGM. We discuss in §4.4 various solutions to this problem. While the discrepancy is unwelcome, it is not so large that it precludes drawing other useful information about the properties of the CGM in simulations.

For example, the OVI column density profiles in the left panel of Fig. 4.5 are remarkably flat. From the centre out to 250 kpc, $N_{\rm OVI}$ varies less than 0.2 dex in the $0.002 < L/L^\star < 0.1$ range. In both $0.1 < L/L^\star < 1$ and $1 < L/L^\star < 10$ luminosities, $N_{\rm OVI}$ slowly, but steadily declines 0.7 dex over 300 kpc. S12 and Hummels et al. (2013) both showed that with lower feedback, the OVI does not extend to high radii. However, with sufficient feedback to match the stellar mass a galaxy should have, the OVI extends

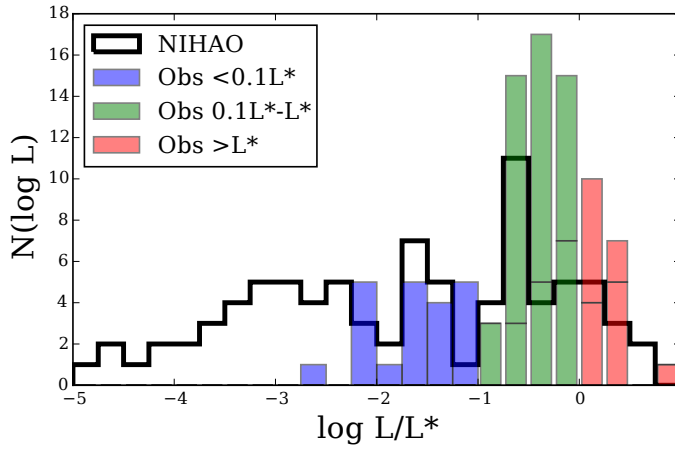

Figure 4.6. Luminosity distribution of NIHAO galaxies is presented as a black line. The colored bars (blue, green, red) show the distribution of observations from Prochaska et al. (2011) and Tumlinson et al. (2011).

in a flat distribution as far as the observations. Suresh et al. (2015) shows a much steeper profile, close to a 2 dex decline in N_{OVI} over 300 kpc in *Illustris*. Ford et al. (2015) shows little decline to 150 kpc in either their energy dependent or constant wind model. But we note that the Ford et al. (2015) analysis compares equivalent widths instead of column densities.

To examine the question of how much OVI depends on stellar mass or luminosity, the right panels of Fig. 4.4 and Fig. 4.5 show column density as a function of stellar mass and galaxy luminosity, respectively, binned into three ranges of the *impact parameter b*: $20 < b/\mathrm{kpc} < 100$, $100 < b/\mathrm{kpc} < 200$ and $b/\mathrm{kpc} > 200$. The median column density is shown as the black line. The green area outlines the spread between the 5th and 95th percentiles in the 0.25 dex luminosity bins. The simulations follow the general trends of the observations, albeit nearly a dex below the observations in all radial ranges.

The simulations clearly show a correlation between stellar mass and N_{OVI} in Fig. 4.4. This relation is mirrored in the luminosity trends in Fig. 4.5. N_{OVI} rises steadily from unobservable to a threshold N_{OVI} around 10^{14} cm^{-2}. The simulations reach the 10^{14} cm^{-2} threshold at higher galaxy luminosities the higher the impact parameter range is, from $10^{-0.5}L^{\star}$ in the central bin, to $L^{\star}$ in the medium distance radius to $> L^{\star}$ for the largest values of b. It makes sense that brighter galaxies that formed more stars have more enriched material further away. The issue with the simulations seems to be that the threshold N_{OVI} is lower than what is observed.

N_{OVI} observations are often interpreted as showing little to no depen-

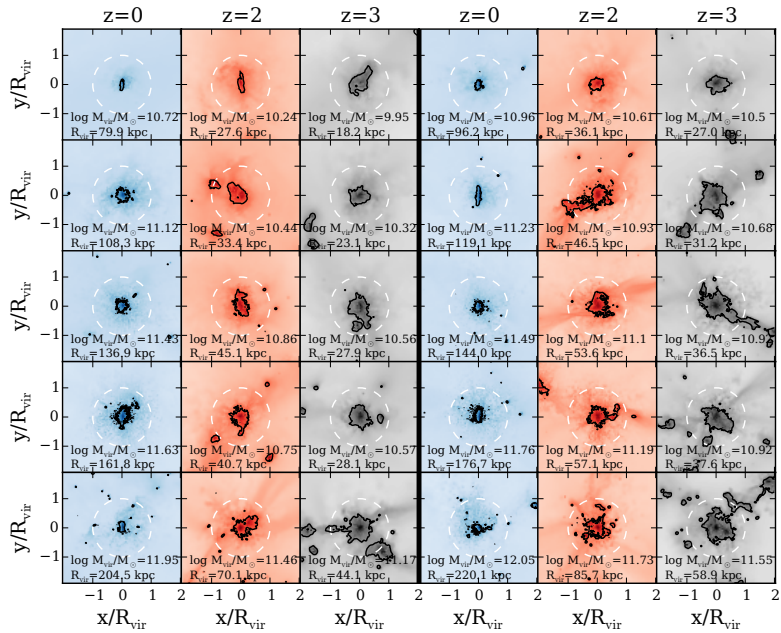

Figure 4.7. Face-on HI column density maps for 10 NIHAO galaxies. The first and fourth column shows $z = 0$, while the two neighboring columns show $z = 2$ and $z = 3$, respectively. The black contours indicate the $\log N_{HI} > 17.2$ cm^{-2} threshold, above which the gas is considered optically thick. Each box is $2R_{\rm vir}$ on each side, while the dashed white circle indicates the virial radius.

dence on luminosity. More observations are necessary to make definite statements, but the right panels of Fig. 4.5 hint at a correlation. To distinguish whether there is a trend or not, more observations are necessary at lower luminosities, since there are very few OVI detections below $0.1L^{\star}$. The trend in the simulations is visible because they predict $N_{\rm OVI}$ below the detectable limit.

4.3.2 Cold gas

Quasar absorption line spectra also include many low ionization absorption lines that indicate the presence of cool gas. Here, we examine HI as the proxy for cool gas in the simulations. Since hydrogen is so abundant, getting the correct ionization fraction requires following radiative transfer. Rahmati et al. (2013) found that a local self-shielding approximation gives results reasonably consistent with the full radiative transfer solution. We report HI column densities based on Rahmati et al. (2013) and note that this is a different treatment than that used in S12, which used an

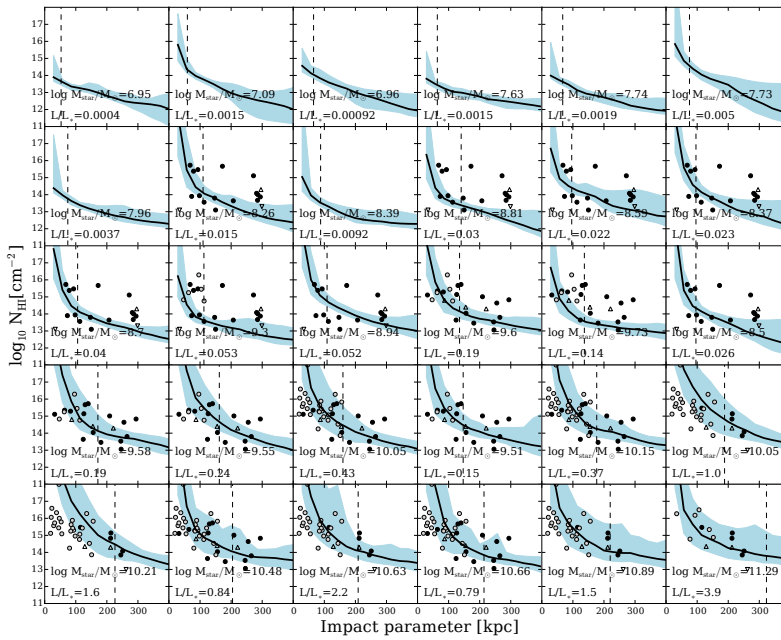

Figure 4.8. Mock sightline distributions of HI column density for the same 30 NIHAO galaxies as in Fig. 4.2. Observational data from Prochaska et al. 2011 (black symbols) and Tumlinson et al. 2013 (white circles). The data is split into three groups: $L < 0.1L^\star$, $0.1L^\star < L < 1L^\star$ and $L > 1L^\star$. Only the relevant group is overplotted according to the luminosity of the shown galaxy.

Table 4.1. Covering fractions of HI for halos with $M_{\rm Halo} \sim 10^{12}\,{\rm M}_{\odot}$ at $z = 2$ and $z = 3$ and for Rudie et al. (2012).

$\log(N_{\rm HI}/({\rm cm}^{-2}))$	z=2 $f_{\rm C}(< R_{\rm vir})$	z=2 $f_{\rm C}(< 2R_{\rm vir})$	z=3 $f_{\rm C}(< R_{\rm vir})$	z=3 $f_{\rm C}(< 2R_{\rm vir})$
> 15.5	$45 \pm 3\%$	$20 \pm 1\%$	$73 \pm 7\%$	$41 \pm 10\%$
> 17.2	$12 \pm 1\%$	$3.8 \pm 0.2\%$	$24 \pm 5\%$	$10 \pm 4\%$
> 19.0	$2.5 \pm 0.2\%$	$0.8 \pm 0.1\%$	$5 \pm 3\%$	$2 \pm 1\%$
> 20.3	$0.8 \pm 0.1\%$	$0.25 \pm 0.04\%$	$1.4 \pm 0.7\%$	$0.5 \pm 0.3\%$

$\log(N_{\rm HI}/({\rm cm}^{-2}))$	Rudie+2012 $f_{\rm C}(< R_{\rm vir})$	Rudie+2012 $f_{\rm C}(< 2R_{\rm vir})$
> 15.5	$90 \pm 9\%$	$68 \pm 9\%$
> 17.2	$30 \pm 14\%$	$28 \pm 9\%$
> 19.0	$10 \pm 9\%$	$8 \pm 5\%$
> 20.3	$0^{+10}_{-0}\%$	$4 \pm 4\%$

equilibrium CLOUDY model for determining HI fractions. Details can be found in §4.2.1.

Fig. 4.7 shows HI maps at $z = 0$ (blue), $z = 2$ (red), and $z = 3$ (grey) for a representative selection of 10 galaxies spanning the NIHAO mass range. Each image is scaled to be 4 $R_{\rm vir}$ across and along a ~ 4 Mpc line-of-sight (a discussion of this is in section 4.4). We extended our analysis to higher redshifts because most of the observational data for low ionization lines have been collected at $z > 2$. At these high-z, massive galaxies show surprisingly high covering fractions of cool gas (e.g. Rudie et al. 2013; Prochaska et al. 2014; Crighton et al. 2015).

The white dashed circle is drawn at $R_{\rm vir}$ and the black contours show where $\log N_{HI} > 17.2$, sometimes used as a limit for where HI is considered optically thick. Log $N_{HI} > 17.2$ is used as a threshold in Fig. 4.9 to calculate the covering fractions of HI inside $R_{\rm vir}$ and $2R_{\rm vir}$ for the three redshifts shown using the entire NIHAO sample. Since covering fraction measurements are limited by the sparseness of bright background quasars, there are only two reported observational data points at $z = 2 - 3$. Our estimates are compared with the observations of Rudie et al. (2012), who looked at a sample of Lyman Break Galaxies (LBGs) and Damped Lyman Alphas (DLAs) in the redshift range $z = 2 - 2.5$. LBGs have a higher $M_{\rm vir}$ than nearly every NIHAO galaxy (but for comparisons of larger galaxies simulated with a similar feedback scheme, see Faucher-Giguère et al. 2015; Faucher-Giguere et al. 2016). We also compare to a data point of Prochaska et al. (2013), who measured Lyman limit systems in a redshift range $z = 2 - 2.5$ with the aid of luminous background quasars.

With that caveat, it appears the simulated covering fractions inside

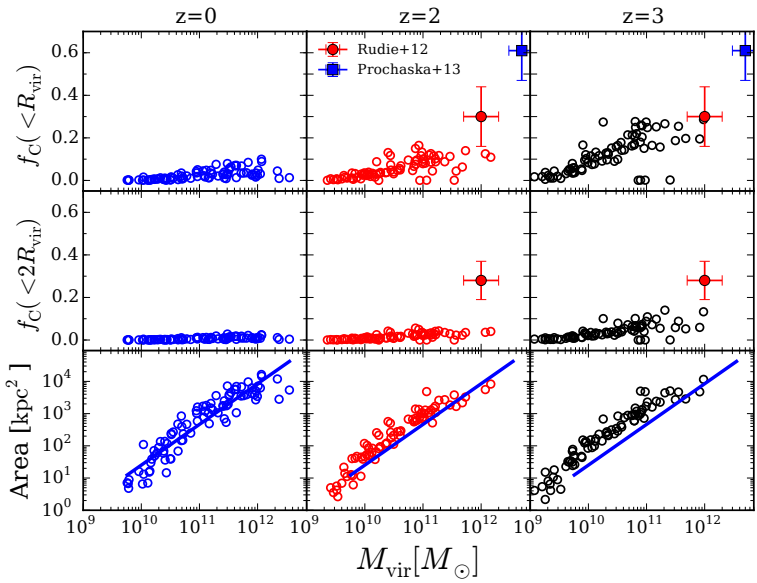

Figure 4.9. Fraction of area covered by HI with a column density for which $\log N_{HI} > 17.2$ cm^{-2}. Upper panels show the projected area fraction inside $R_{\rm vir}$ for $z = 0, 2$ and 3. Middle panels show the covering fraction in $2R_{\rm vir}$. The red error bars are from observations by Rudie et al. (2012), who observed LBGs in a redshift range $z = 2 - 2.5$. The blue error bars are from Prochaska et al. (2013) measurements of Lyman limit systems (LLS) via luminous quasi-stellar objects (QSOs). We plot the same observational points on our $z = 2$ and $z = 3$ panels. The middle panels also include an observational point from Rudie et al. (2012) for the fraction inside $2R_{\rm vir}$. The lower panels show the area covered (in kpc^2). The blue line is a power law fit to the $z = 0$ data and overplotted on the $z = 2$ and $z = 3$ panels for reference.

$R_{\rm vir}$ reach nearly the level of the Rudie et al. (2012) data point at $z = 3$. However, when comparing with the larger $2R_{\rm vir}$ measurement, the simulated covering fraction halves. As we will see, observations repeatedly find more cool gas distributed far from galaxies than simulations. In Rudie et al. (2012), the cool gas seems to extend well beyond $R_{\rm vir}$.

After the galaxies have evolved to $z = 2$, the simulations show about half the covering fractions they did at $z = 3$. So, the simulations show covering fractions less than one half of those found in the observations.

The lowest three panels in Fig. 4.9 show that the simulations actually maintain a constant optically thick physical area according to the galaxy's $M_{\rm vir}$. The blue line in each panel shows the fit to the $z = 0$ data and is

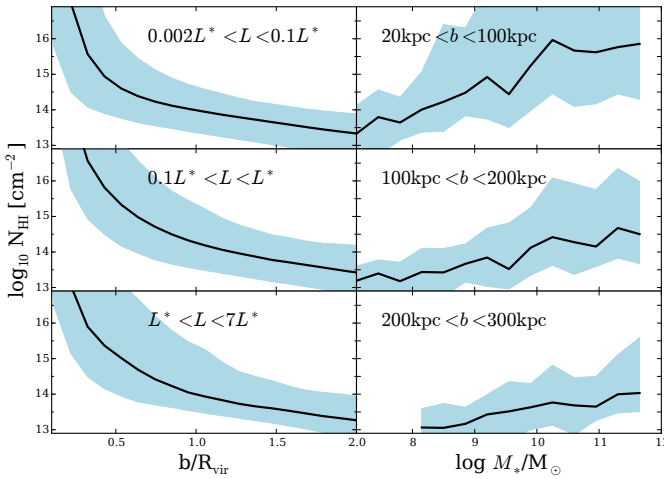

Figure 4.10. HI column density ($z = 0$) as a function of: impact parameter normalized to the virial radius (left panels) and stellar mass (right panels). All sight lines from face-on and edge-on for every NIHAO galaxy are included. The black solid line shows the median column density at $z = 0$, while the green band shows the 5-95 percentile range. In the left panels, the column densities are divided between three luminosity bins: $L < 0.1L^{\star}$ (upper panel), $0.1L^{\star} < L < 1L^{\star}$ (middle panel) and $L > 1L^{\star}$ (lower panel). In the right panels, the column densities are divided between radial bins: $20 < b/\mathrm{kpc} < 100$ (upper panel), $100 < b/\mathrm{kpc} < 200$ (middle panel) and $b > 200$ kpc (lower panel).

repeated in each panel as a reference for the reader. From this, it can be seen that the area covered does not increase much over time and that the covering fractions are decreasing mostly due to the increasing R_{vir} as the background density decreases and the Universe evolves.

We also compare our most massive systems with further data from Rudie et al. (2012) in table 4.1. For each covering fraction at different column density thresholds, our $z = 3$ measurements are closer to the observations, but most are still too low by more than 1 sigma. It should be noted that our line-of-sight is limited to the zoom region ($\sim 4\,\mathrm{Mpc}$) which is significantly less than in observations. This biases our column densities to lower values. Since other simulations have also under-predicted the HI covering fractions, this points to an issue with the amount of HI at larger radii (but see Faucher-Giguere et al. 2016 and Rahmati et al. 2015 for discussion of the effect of feedback strength on HI covering fractions).

Figs. 4.10 and 4.11 present the combination of the data from the entire

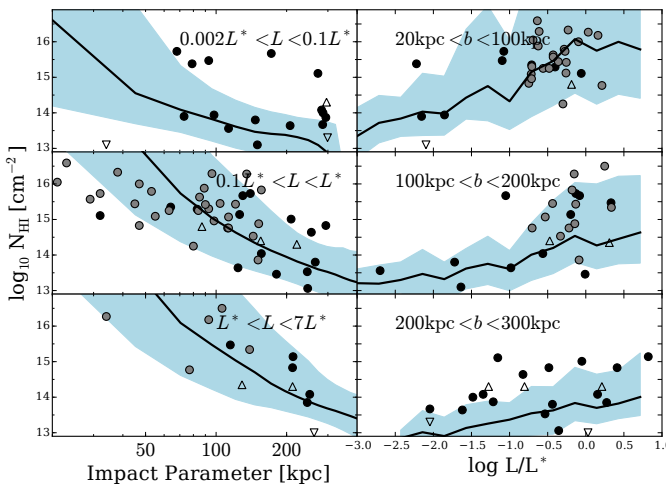

Figure 4.11. HI column density ($z = 0$) as a function of: impact parameter (left panels) and luminosity (right panels). The simulations and binning are the same as in Fig. 4.4 above. Observational data from Prochaska et al. (2011) are shown as black circles. Tumlinson et al. (2013) data is shown as gray circles. Non-detected upper and optically thick lower limits are shown as upward and downward facing open triangles, respectively. Observational points are only shown in the lower panels, since the virial radii and stellar masses of the observations are not known.

NIHAO sample (86 galaxies at $z = 0$) in the same manner as was done for OVI in Figs. 4.4 and 4.5. Again, individual galaxy profiles can be viewed in Fig. 4.8. In both panels of Fig. 4.11, the black line shows the median of the combined data and while the shaded region shows the range of data from the 5th to 95th percentile. In the left panel, column density profiles are combinations of column densities from galaxies broken into three luminosity bins. The simulations show a broader scatter in HI than they did for OVI.

The simulations agree much better with the HI data than they did with the OVI data. In all three luminosity bins, the median column density line goes through the middle of the observations. The simulations have a similar scatter to the observations. One possible exception is the dwarf galaxies ($L < 0.1L^{\star}$), for which there are observations outside 100 kpc that show higher column densities than the simulated column densities.

The right panels of Fig. 4.11 show how the HI column density varies as a function of galaxy luminosity, split into three impact parameter bins: $20 < b/\mathrm{kpc} < 100$, $100 < b/\mathrm{kpc} < 200$, and $200 < b/\mathrm{kpc} < 300$.

It is clear in Fig. 4.11 that the scatter of HI columns is largest close to the galaxy. The median HI column density in the simulations increases strongly when going towards smaller projected radii. This trend goes with galaxy luminosity. In the two inner b bins (two upper right panels of Fig. 4.11), the simulated median column density generally follows the observations. The column density does not increase as much in the outer two radial b bins. In the 100-200 kpc bin, it appears that the median observed HI column density actually increases. Again, outside 200 kpc, the observed column densities are above the simulation. It seems that the simulations have trouble putting enough cool gas at large distances from galaxies. This could be an improper treatment of the hydrodynamics or an incorrect propulsion of the winds. We discuss reasons for the lack of HI at large distances in §4.4.2.

4.3.3 Outflows and shape of the CGM

Since quasars are so rare, it will never be possible to observe the shape of the low density CGM with absorption line studies. However, closer to the disk, integral field unit (IFU) spectrographs are making it possible to map velocity dispersions of gas immediately surrounding galaxies. In recent observational studies (Wild et al. 2014), it has been assumed that an increase in velocity dispersion above and below the plane of the disk is a dynamical signature of bipolar outflows. Since outflows are expected to create steamers extending radially outward from the nucleus, the line-of-sight velocity dispersion should increase in the presence of a superwind. This is due to the increased line width caused by the bulk motion of the gas toward and away from the observer (Wild et al. 2014). Wild et al. (2014) use this method to study the kinematical structure of the "Mice" spirals, a major merger galaxy pair, and identified strong, galactic scale

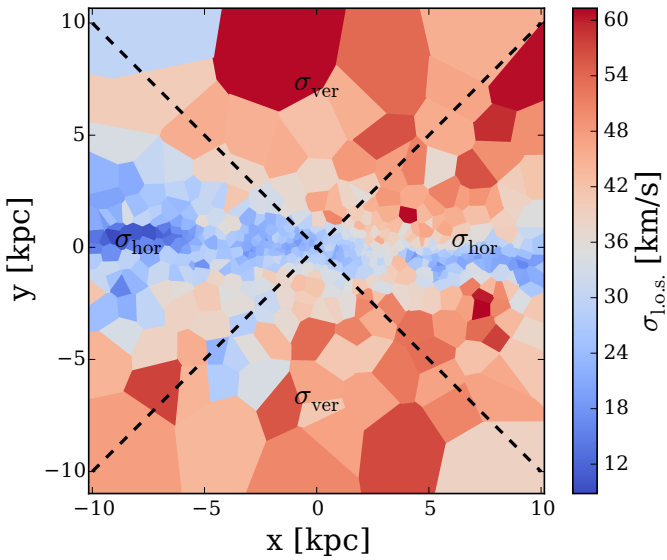

Figure 4.12. Edge-on velocity dispersion map of NIHAO galaxy, g5.02e11 at $z = 0$. In the tessellation, the disk is apparent as lower line-of-sight (los) velocity dispersion (blue). Above and below the plane of the disk, the los velocity dispersion increases (red). Wild et al. (2014) proposes dividing the velocity dispersion map using the black dashed lines to detect a bipolar outflow. $\sigma_{\rm ver}$ is the mean velocity dispersion in the triangular regions above and below the disk, while $\sigma_{\rm hor}$ indicates the mean velocity dispersion in the disk plane.

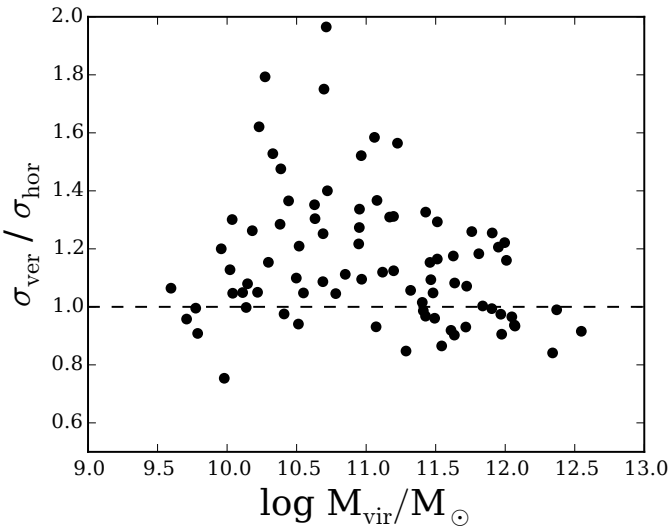

Figure 4.13. $\langle\sigma_{\rm ver}\rangle/\langle\sigma_{\rm hor}\rangle$ as a function of halo mass, $M_{\rm vir}$. $\langle\sigma_{\rm ver}\rangle > \langle\sigma_{\rm hor}\rangle$ in 70% of NIHAO galaxies, which can be interpreted as a preference for outflows to be perpendicular to the disk. Low and high mass galaxies have less clear bipolar outflows than galaxies with masses in the range $10.3 < \log(M_{\rm vir}/{\rm M}_{\odot}) < 11.3$. Low feedback efficiency in low mass galaxies and deep potential wells in high mass galaxies limit the amount of gas that escapes perpendicular to the disk.

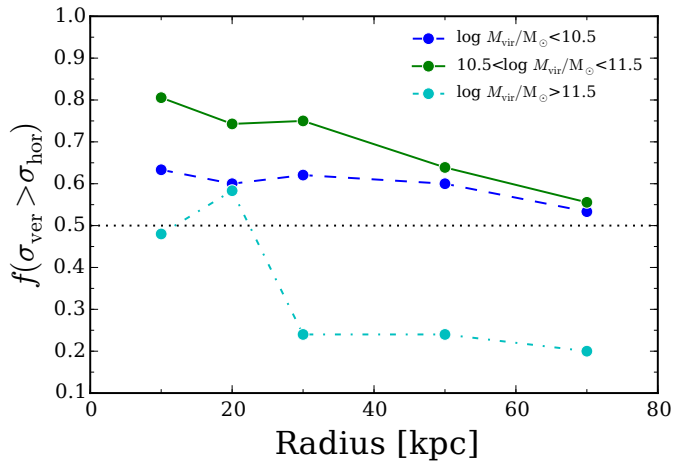

Figure 4.14. Fraction of all NIHAO galaxies with $\langle\sigma_{\rm ver}\rangle > \langle\sigma_{\rm hor}\rangle$ as a function of galaxy radius in three different halo mass ranges, $logM_{\rm vir}/\,{\rm M}_\odot < 10.5$ (blue dashed line), $10.5 < logM_{\rm vir}/\,{\rm M}_\odot < 11.5$ (green solid line) and $logM_{\rm vir}/\,{\rm M}_\odot > 11.5$ (cyan dash-dotted line). The higher fraction of galaxies with $\langle\sigma_{\rm ver}\rangle > \langle\sigma_{\rm hor}\rangle$ at small radii indicates that bipolar outflows extend to ∼40 kpc. The low fractions for the largest halos are due to the extended gas disks that dominate the velocity dispersion in the plane of the disks.

outflows in one the of "Mice" (NGC 4676A) using the IFU survey CALIFA. Since a pressure driven wind will exit a galaxy in the direction of least pressure (Hayward and Hopkins 2015), we expect outflows to exit our disks in bipolar outflows.

For this study, we make mock IFU observations of the disk edge-on. To this end, we project the galaxy onto the x-y plane and divide the plane into cells of approximately the same number of particles. A Voronoi tessellation is calculated based on the center of mass of each cell and the line-of-sight velocity dispersion is calculated for all particles in each cell. An example of a velocity dispersion map for the inner 10 kpc of a $5 \times 10^{11} M_{\odot}$ galaxy from NIHAO is shown in Fig. 4.12. The black dashed lines split the map into four triangular areas. The mean velocity dispersion of each of these is calculated. The mean velocity dispersion about the center of mass of the cells in the vertical direction (above and below the disk) is called $\sigma_{\rm ver}$. The mean velocity dispersion in the cells along the plane of the disk (left and right) regions is called $\sigma_{\rm hor}$.

To understand whether there is an outflow trend with halo mass, Fig. 4.13 shows the ratio of the mean velocity dispersions in the two directions, $\sigma_{\rm ver}/\sigma_{\rm hor}$, inside 10 kpc as a function of $M_{\rm vir}$. The most significant outflows (i.e. the departure from a ratio of 1) are seen between $10.2 < \log(M_{\rm vir}\,/\mathrm{M}_{\odot}) < 11$. These are similar masses to where the maximum stellar feedback effects are seen in other studies like Di Cintio et al. (2014) and Tollet et al. (2016b), so it is no surprise that the strongest bipolar outflow signal is seen here.

In the lowest mass galaxies, the lack of bipolar signal can be attributed to the lack of star formation. Stars form sporadically at these low masses, so it is unlikely outflows would be detected at the one output when these measurements are made. Few stars have formed over the last several Gyr in these lowest mass simulations. In higher mass galaxies, there is plenty of star formation to potentially drive winds, but wind strengths do not increase so the deepening potential well in more massive galaxies keeps the gas locked inside the disk.

A perfectly isotropic velocity dispersion would not show any of the heightened velocity dispersion in the vertical direction that is seen in Fig. 4.13. An isotropic distribution would have half the galaxies above and half below 1. Inside 10 kpc, 71% of galaxies have an increased velocity dispersion above and below the plane of the disk relative to around the disk. So, Fig. 4.14 looks at the fraction as a function of radius for three different halo mass ranges. Both the small ($\log M_{\rm Halo}/\,\mathrm{M}_{\odot} < 10.5$) and intermediate ($10.5 < \log M_{\rm Halo}/\,\mathrm{M}_{\odot} < 11.5$) halo mass ranges shows that the velocity dispersion becomes more isotropic as we move out. Bipolar outflows are most visible in intermediate mass galaxies at radii out to around 50 kpc. Beyond 50 kpc, CGM turbulence and galaxy mergers mix the gas such that the bipolarity is no longer visible. The largest halos ($\log M_{\rm Halo}/\,\mathrm{M}_{\odot} > 11.5$) have a very low dispersion ratio. This is due to the

Table 4.2. Fitting parameters for the $M_{\rm vir}$-c/a relation in Fig. 4.15. Parameters are of the form $c/a = \alpha \cdot \log_{10}(M_{\rm vir})$+c.

	T/K	α	c
Hot gas ($M_{\rm vir} < 2 \times 10^{11} M_\odot$)	$T > 10^6$	0.469	-4.395
Hot gas ($M_{\rm vir} > 2 \times 10^{11} M_\odot$)	$T > 10^6$	0.023	0.596
Warm gas	$3 \times 10^4 < T < 3 \times 10^5$	0.004	0.771
Cold gas	$T < 15000$	-0.036	0.751

fact that our largest systems are dominated by extended gas disks, which fall into our CGM definition but lie in the plane of the disk.

In the center of the halo ($r \lesssim 50\,$kpc), our predictions of the velocity dispersion will depend on our specific thermal feedback prescription, since this is what is driving the outflows. And yet, the feedback strength was calibrated to obtain the correct stellar mass - halo mass relation, so although stronger or weaker feedback would effect this result, such a prescription would not at the same time also match the stellar mass relation.

Triaxial fit. IFU observations are limited to the inner few kpc of a galaxy and QSO absorption spectra are limited to viewing one line of sight. In light of this, it is very difficult to get any data on the general shape of the CGM out to the virial radius. To get a theoretical handle on its shape and provide some numerical estimates for further use by models, we use the inertia tensor to give a rough quantity of the shape. The inertia tensor is a 3×3 matrix, which in the common definition is the sum of tensor products of all the particle positions weighted by their masses. The eigenvectors of the inertia tensor point in the 3 orthogonal directions of the major, intermediate, and minor axes. The eigenvalues of the inertia tensor are the lengths of the major axis and two orthogonal minor axes. These eigenvalues thus define a triaxial ellipsoid.

We wish to focus our study of CGM shape on only halo gas, so we try to exclude disk gas from our shape measurement. Low density is the best determinant of halo gas, so we classify the halo as all gas with gas density, $n < 10^{-2}$ cm^{-2}, and lies outside $0.1R_{\rm vir}$. The density was chosen as the density where self-shielding starts becoming effective. We did not add a temperature cut because some analyses of the CGM have found that it is surprisingly cold. We did not want a temperature cut in our definition to preclude this possibility in our analysis.

Fig. 4.15 shows the eigenvalues of the inertia tensor for halo inside $0.5R_{\rm vir}$. The upper panels show c/a, where a is the major axis and c the minor axis of the fitted ellipsoid as a function of total mass of the galaxy. The lower panels show b/a, where b is the middle axis of the fit. The left panels show the hot gas (red circles, $T > 10^6$K) in each galaxy. The right

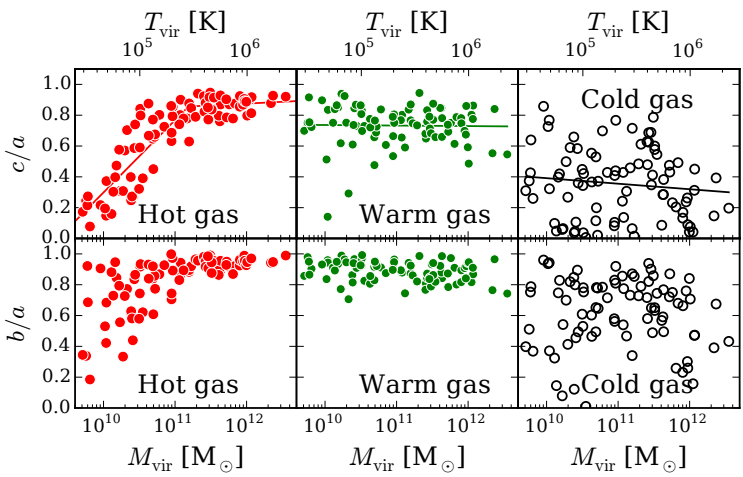

Figure 4.15. c/a (upper panels) and b/a (lower panels) for the gas shape (without the disk in $0.5R_{\rm vir}$, this radius is a compromise between being too close, which would mean not capturing enough of the halo and too far, where the CGM is already so well mixed, that no structure would be recognizable.) in three temperature ranges. Hot gas: $T/K > 10^6$ (red circles), warm gas: $3 \times 10^4 < T/\mathrm{K} < 3 \times 10^5$ (green circles) and cold gas: $T/K < 15000$ (black open circles). Lines show fits to the data in the respective color. Fit values can be seen in table 4.2.

panels show the intermediate (green circles, $3 \times 10^4 < T/\mathrm{K} < 3 \times 10^5$) and cool gas (white circles, $T < 1.5 \times 10^4$ K) for each NIHAO galaxy. The three temperature regimes are roughly the portions of the cooling curve dominated by 3 different cooling processes. The hot regime is dominated by bremsstrahlung, the warm is dominated by metal cooling, while the cool regime is dominated by hydrogen and helium line cooling. The lines represent simple fits to the distribution of c/a. The fitting parameters are given in table 4.2.

The c/a distribution of the hot gas rises steadily with mass up to around $2 \times 10^{11} M_\odot$. Since the b/a ratio also grows with a similar, albeit not so strong trend, the hot gas distribution transforms from being prolate at low masses (small c/a and small b/a) to being mostly oblate or even spherical at high masses. The flattening at high masses can be understood with galaxy virial temperatures in mind. The virial temperature is the peak temperature inflowing gas can reach falling into a potential well. Anything higher, so for most NIHAO galaxies our hot CGM gas, should come from gas heated by stellar feedback.

For the most massive galaxies, our hot CGM threshold is their virial temperature. We expect more massive galaxies where the gas is heated by gravitational infall should be more spherical. The hot gas already attains a spherical shape in galaxies with lower virial temperature than 10^6 K. The hot CGM may become spherical at slight lower masses (lower virial temperatures) due to winds reaching sufficient distances from the galaxy, and then being blown back and shaped by the ambient CGM.

Warm gas does not exhibit the same trend with c/a as the hot gas at low masses. Both the c/a and the b/a values stay relatively constant and high (~ 0.8) across all halo masses indicating a mostly spherical shape. The relatively high c/a and b/a values are due to the fact that this gas is both cooling out from the halo and isotropically falling inwards. Some of this is also gas that has been heated by stellar feedback and blown out perpendicular to the plane of the disk.

The cold gas exhibits the lowest c/a values, as one would expect since it is dominated by the inner disk. One would further expect a cold gas disk to have high b/a values since those axes should be approximately the same length. For the most part, the b/a values are high in Fig. 4.15, though they tend towards lower values at low and high masses. In general, the cold gas measurements show the largest scatter, most likely since it becomes extremely sparse beyond the inner disk and is hard to fit.

CGM-Disk orientation. Since outflows are expected to be aligned perpendicular to the plane of the disk, the hot CGM should appear bipolar in galaxies with lower virial temperatures than 10^6 K. The prolate shape at low masses could indicate that the hot CGM is configured as a bipolar outflow. To understand whether this is the case, we present Fig. 4.16. It shows the angle between the angular momentum vector of the disk and the major axis of the inertia tensor. The angle is plotted as a function of M_{vir}.

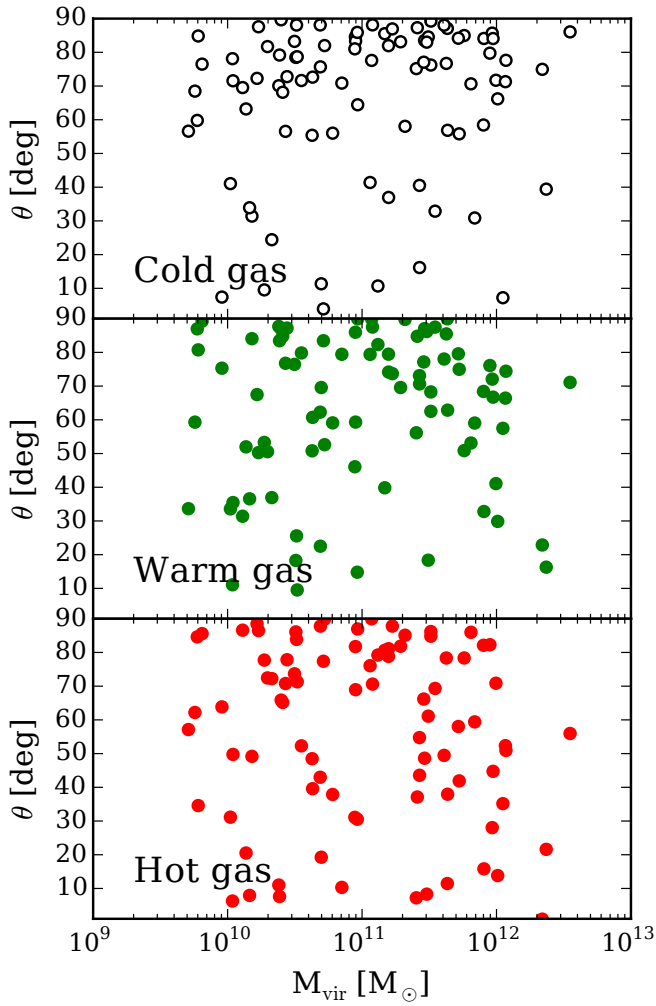

Figure 4.16. Angle θ between the rotation axis of the disk and the major axis of the inertia tensor fit as a function of viral mass. 90° indicates that the major extent of the fitted gas is in the plane of the disk, while 0° indicates gas extending perpendicular to the disk. Each panel shows a different temperature range of the gas, as denoted on the plots.

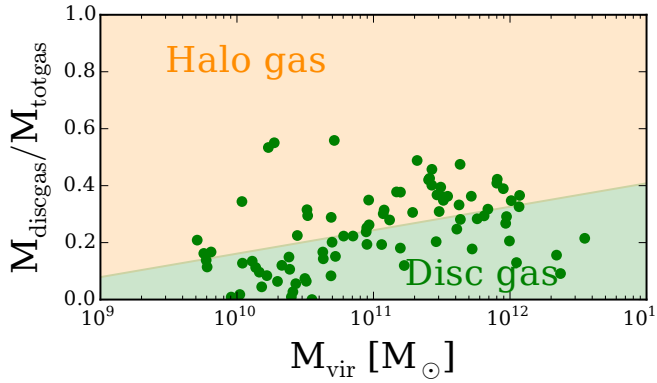

Figure 4.17. Mass fraction of disk gas relative to the total amount of gas. A power law fit to the data is shown as the boundary of the colored areas. The parameters of the fit are given in table 4.3.

A 90° angle indicates that the major moment of inertia axis lies in the plane of the disk, while 0° indicates the gas is perpendicular to the disk.

There is no trend with mass for either the hot or warm gas. In the angle analysis, the alignment appears random. Since the warm and also the hot gas is for the most part spherically shaped, it is not surprising that the orientation of the major axis of the inertia tensor is random.

At low mass, some of the random alignment may not come from the outflow but from the disk angular momentum vector. Stellar feedback drives so much turbulence that most NIHAO galaxies with $M_{\rm vir} < 10^{11}\,{\rm M}_\odot$ do not have well ordered thin disks Obreja et al. (2016), in effect making the direction given to the disk random.

The only temperature gas that does not have random scatter of angle values is the cold gas. For the cold gas, the angle clusters around 90°. Such a configuration is consistent with an extended cool gas disk.

The lack of a clear bipolar shape out to large radii is consistent with our velocity dispersion analysis which showed a fading away of the bipolarity at around 40 kpc. Even the smallest NIHAO galaxies have virial radii larger than this.

4.3.4 Chemical composition of the CGM with galaxy mass

Lastly, we attempt to portray the chemical makeup of the CGM and the disk separately and how these change as a function of halo mass in our simulations. We follow Suresh et al. (2015) and define the disk as all gas inside $0.1R_{\rm vir}$ with a density higher than 0.01 cm^{-3}, and the CGM all other gas inside $R_{\rm vir}$. Thus, CGM gas is characterized according to

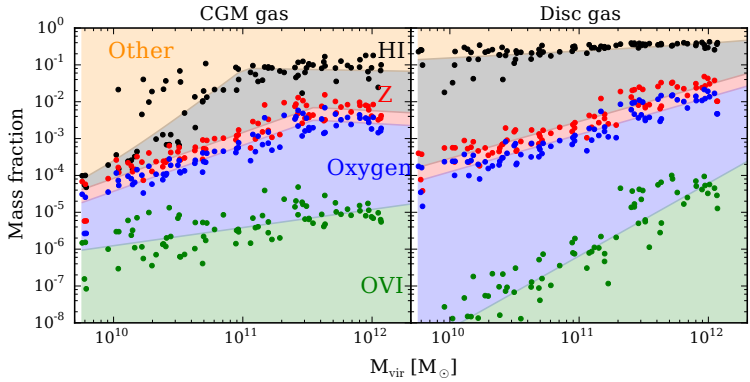

Figure 4.18. Mass fraction of gas split into chemical components. The plot should be read from top to bottom: Of all gas in a given halo mass range, the fraction of gas that is HI is given by the black line and the amount in metals is given by the red line. Of all metals, the mass fraction in oxygen is given by the blue line. Of all oxygen, the mass fraction in OVI is given by the red line. Each line is a fit to the data points and the fit parameters are given in table 4.3.

its diffuse nature, but the definition includes all gas inside $R_{\rm vir}$, allowing satellite galaxies and streams that may have pockets of higher density gas to be classified as part of the halo.

Fig. 4.17 shows the disk gas mass fraction of all the gas inside $R_{\rm vir}$. The disk gas fractions are plotted as a function of $M_{\rm vir}$. In nearly every case, the halo gas comprises the majority of the gas inside $R_{\rm vir}$ (note the logarithmic axes). The disk gas fraction shows a large amount of scatter. Below $3 \times 10^{10}\,{\rm M}_\odot$, the disk gas fraction varies from almost nothing to over 50%. The high variation corresponds with the bursty star formation that happens in such low mass galaxies. The high disk gas fractions represent galaxies that haven't had much recent star formation, while the low disk gas fraction galaxies have had a starburst that blew their cool, dense disk gas away. The NIHAO sample includes few galaxies over $M > 10^{12}\,{\rm M}_\odot$, but the three that show up in Fig. 4.17 indicate that the disk gas fraction starts to drop above $10^{12}\,{\rm M}_\odot$. The pattern is reminiscent of galaxy formation efficiency found using abundance matching techniques (Guo et al. 2010; Moster et al. 2013; Behroozi et al. 2013). One expects the disk gas mass to appear similar to star formation efficiency since stars must form out of cool, dense gas.

Fig. 4.18 shows the mass fractions of the cool and hot gas tracers, OVI and HI, out of the total gas masses for the halo and disk gas components separately. Since OVI is a particular ionic species of oxygen, which itself is a metal, the colored OVI and oxygen regions are subsections of the larger

region of which they are part. The region of the plot above the "Z" metals line is comprised of hydrogen and helium. The part labeled "HI" is the neutral hydrogen component. For clarity, we note that the HI line and points are the HI mass fraction added to the metals mass fraction $(M_{HI} + M_Z)/M_{tot,X}$.

The behavior of the halo and disk gas fraction differ as a function of mass. In the halo, the fractions of the species we tracked increase with increasing M_{vir} to some threshold mass at which point they flatten out and stop rising as a function of mass and may start to decline slightly. In the disk, the fractions of each component continues rising steadily through the high end of the NIHAO mass range.

The metals are all produced as the result of star formation, so one expects the metal fraction to increase in galaxies forming stars. Except for the extreme low mass end, the NIHAO galaxies form stars throughout their lifetimes. The continued increase in the disk metal gas fraction reflects the continued star formation. The halo metals gas fraction flattens because metal enriched outflows decrease significantly, or stop altogether, once galaxies surpass some mass threshold as it becomes harder for winds to escape the disk in the more massive gravitational potential wells (see Muratov et al. 2015, for a detailed study of this). Based on this, the threshold halo mass at which the flattening occurs is a tug-of-war point between feedback strength, which pushes gas outward, and the depth of the gravitational well. As such, if this turnover mass were measured observationally, it could set a contraint for the strength of feedback models.

The metals reach the mass threshold where their mass fractions flatten around $3 \times 10^{11}\,M_\odot$. HI flattens at a lower mass around $M_{vir} = 10^{11}\,M_\odot$. Different physics governs the HI fraction, since it does not increase due to of star formation. Its fraction is dominated by ionization; "other" gas in the halo is mostly ionized hydrogen. Whether the HI fraction comes from outflows or is simply a natural consequence of the gas density profiles of galaxies is a question for study in future work. The sharp decrease in HI fraction in some of the lower mass galaxies reflects the lack of any dense gas in the halos of those galaxies.

The OVI trend is ambiguous as it has the largest scatter of any species, so if the high boundary is indicative of the OVI fraction, then the OVI fractions reduces. The OVI can also be well fit using a single power law, which we have done for simplicity. OVI is a similar case to HI since it will depend on the ionization conditions. The virial temperature of the most massive halos is around the ionization temperature for OVI.

While it is hard to see on the logarithmic scale, the disk HI fraction grows by a factor of a few over the halo mass range. That trend follows the the disk gas mass fraction, and reflects the increasing gas densities with M_{vir}.

The OVI fraction in the disk increases the most steeply of any species, with a slope $M_{disk,OVI} \propto M_{vir}^2$. That increase reflects the deeper disk

Table 4.3. Fitting parameters for the power law fits in fig. 4.18. Parameters are of the form $\log_{10}(f_{\rm X}) = \alpha \cdot \log_{10}(M_{\rm vir})$+c.

	Name	$M_{\rm vir}$ range	α	c
Halo gas	HI	$< 1 \times 10^{11}\,{\rm M}_\odot$	2.643	-30.202
	HI	$> 1 \times 10^{11}\,{\rm M}_\odot$	-0.050	-0.589
	Z	$< 5 \times 10^{11}\,{\rm M}_\odot$	1.214	-16.208
	Z	$> 5 \times 10^{11}\,{\rm M}_\odot$	-0.309	1.476
	O	$< 5 \times 10^{11}\,{\rm M}_\odot$	1.219	-16.608
	O	$> 5 \times 10^{11}\,{\rm M}_\odot$	-0.315	1.202
	OVI	all	0.492	-10.823
Disk gas	HI	all	0.183	-2.643
	Z	all	1.00	-13.534
	O	all	1.011	-14.013
	OVI	all	1.972	-27.880
Disk/Total		all	0.082	-0.662

potential, which is able to hold onto more hot gas as the galaxy gets more massive.

To each mass fraction, we fit power laws. In the case of the gas in the halo, we fit a broken power law to the HI, the metallicity and the oxygen components. The threshold for the break was chosen "by eye" and is $10^{11}\,{\rm M}_\odot$ for HI and $5 \times 10^{11}\,{\rm M}_\odot$ for both the metallicity and the oxygen components. The fitting parameters are given in table 4.3.

4.4 Discussion

In general, the simulated CGM compares well with current observations, but two problems stand out: 1) the OVI simulated column densities are almost 1 dex lower than observations; and 2) optically thick HI extends much further in observations than simulations.

4.4.1 OVI *deficit*

We use the suite of 86 NIHAO simulations to analyse the CGM and the extent of OVI column densities out past the virial radius of galaxies from $\log(M_{\rm Halo}/\,{\rm M}_\odot) \sim 9 - 12$. The right panel of Fig. 4.4 shows how the predicted OVI column density changes with the stellar mass of the galaxy. Fig. 4.5 shows the changes with impact parameter and luminosity and includes the observations. We under-predict OVI at all radii and for all galaxy luminosities by about the same amount everywhere, approximately 1 dex. The origin of this discrepancy is not yet well understood, but has

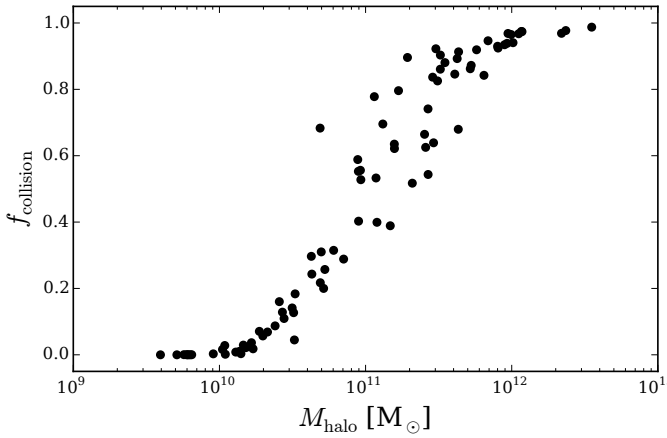

Figure 4.19. Mass fraction of OVI in the CGM created by collisional ionization per galaxy as a function of halo mass. OVI in low mass galaxies is mainly created through photoionization from the UV background. Massive galaxies have a large fraction of OVI that is collisionally ionized.

been seen in most galaxy formation simulations to date (Hummels et al. 2013; Suresh et al. 2015; Ford et al. 2015). While Suresh et al. (2015) suggest that the observations are consistent with a constant column density across galaxy mass/luminosity, the observations are also consistent with an increase to around $1L^*$, above which the trend flattens off. In the simulations, the plateau is at $\log(N_{\rm OVI}/{\rm cm}^{-2}) \sim 13.5$ in each radial range. The plateau is reached at progressively higher luminosities at larger radii.

The observational data is relatively sparse and shows a fairly broad scatter, but there may be a similar plateau that is higher than the simulations, at $\log(N_{\rm OVI}/{\rm cm}^{-2}) \sim 14$.

OVI can be photoionized at low temperatures and low densities ($T \lesssim 10^{4.5}$ K, $\rho \lesssim 10^{-4}{\rm cm}^{-3}$) by incoming radiation assuming photoionization equilibrium (see Kollmeier et al. 2014, for possible shortcomings of this assumption) and a constant UV background. Assuming collisional ionization equilibrium produces OVI in denser gas ($\rho \gtrsim 10^{-4}{\rm cm}^{-3}$) with temperatures around $10^5 - 10^6$K. Disentangling these two channels is vital to get the correct amount of OVI.

Fig. 4.19 shows the mass fraction of OVI in the CGM produced by collisional ionization, $f_{\rm collision}$, as a function of halo mass for all NIHAO galaxies. The definition of CGM is the same as in the rest of the chapter and $f_{\rm collision}$ is defined as the fraction of OVI above 10^5 K with respect to the total amount of OVI in the CGM per galaxy. This approximation of the amount of collisionally ionized OVI is adequate to get a sense of the

trend as a function of halo mass, which is all we are interested in here.

Small galaxies are mainly photoionized, while massive galaxies are predominantly collisionally ionized. The approximate threshold halo mass between these two regimes is 10^{11} $M_\odot$. This is caused by the fact that much of the CGM gas is around the virial temperature, which enters the OVI collisional ionization regime at about this halo mass, being too low for smaller galaxies.

The assumption of collisional ionization equilibrium (CIE) generally works best in high density, low temperature regions. Not assuming CIE has been tested in a variety of non-equilibrium models (see Cen and Fang 2006; Savage et al. 2014; Oppenheimer et al. 2016). Cen and Fang (2006) show a decrease in the OVI column densities relative to CIE since the shock heated gas is initially above 10^6 K and cools through the collisional ionization regime. Conversely, Savage et al. (2014) show that non-CIE models can increase the amount of OVI produced through collisional ionization at temperatures below 10^5 K. Although testing non-CIE models might hold the answer to the OVI deficit, it is beyond the scope of this analysis.

Ford et al. (2015) point out that while the virial temperature of massive halos around 10^{12} $M_\odot$ is around 10^6K, most gas that is *photoionized* into the OVI state has a temperature around $10^{4.5}$K. OVI ionization might best be explained as a transient state of hot gas cooling out of the halo. Simulations have a hard time capturing non-equilibrium states, so they might therefore show a persistent deficit in OVI. Rahmati et al. (2015) find that collisional ionization is a non-negligible effect for OVI. Collisional ionization fractions are above 20% for $z = 0.1$ in their fiducial model.

The only way photoionization from the UV background could be the dominant process in producing OVI in massive halos above 10^{11} $M_\odot$ would be if the CGM gas were systematically cooler. This means either the gas never shock heated to the virial temperature or the cooling time is short enough to pass through the collisional ionization range without exciting OVI. But since simulations generally have trouble with the overproduction of stars, a further enhanced cooling time would worsen this problem.

Both Shen et al. (2012) and Suresh et al. (2015) ran models that included local sources of photoionization to test whether this significantly effects the overall amount of OVI. Both found that the effect is negligible for $r \gtrsim 50$ kpc. So, although this could ameliorate the OVI deficit in the center of haloes, this is not sufficient to account of the large amounts at larger radii.

The two main pieces of physics that contribute to the OVI column density are *stellar feedback* that drives galactic outflows and the *radiation field*. The detailed interaction of stellar feedback with the interstellar medium and the CGM are poorly resolved in simulations. The shock fronts occur on small scales relative to the distance that the outflowing gas travels, so they are difficult to model. In spite of the poor resolution, S12 and Hummels et al. (2013) showed the strength of stellar feedback has a big impact on OVI column densities. Also, if resolution was a major

cause of error, the NIHAO simulations would show a clear difference in CGM properties with halo mass, since the physical resolution decreases with increasing galaxy mass.

Fig. 4.18 shows that there is plenty of oxygen in the CGM, so matching the observations seems not to be a matter of transport, but one of getting it into the correct ionization state. Hummels et al. (2013) tested manually varying either the density, the metallicity or the temperature of their simulations. Only the simulations with feedback and outflows and a manually decreased temperature (to 3×10^5 K) could produce enough OVI to reproduce the observations. They note that temperature structure of the CGM is dependent on resolution within $r \gtrsim 50$ kpc based on their thermal feedback prescription.

An intrinsic error in our method to be noted is that we only account for gas absorption within ~ 4 Mpc of the galaxies. We are aware that quasar sightlines pass through a larger volume, possibly gathering additional absorption lines along this path. This would cause our column densities to be underestimated. We assume this effect to be small, similar to other analysis such as Hummels et al. (2013).

4.4.2 Extended HI

One of the more mysterious discoveries about the CGM has been observations of optically thick, cool, neutral gas covering large cross sections surrounding galaxies (Hennawi et al. 2006; Prochaska et al. 2013; Werk et al. 2014). Particularly perplexing is that the cool gas covering fractions increase when looking at more massive galaxies that are also quasars (Prochaska et al. 2014). Naively, more massive galaxies should have hotter CGMs and quasars should ionize any neutral gas. Observations show the opposite: quasars have more cool, neutral gas in the form of small, dense clouds.

Our simulations are not ideally suited to study the CGM of massive galaxies at high-z; NIHAO is focused on galaxies smaller than the Milky Way at $z = 0$. However, we present a comparison to give some idea of how our simulations perform on this problem. Our HI ionization fraction takes self-shielding into account, which has the effect of increasing the amount of HI in high density regions. Fig. 4.9 shows that optically thick HI covers a small fraction of $R_{\rm vir}$ at $z = 0$, but that the NIHAO simulations cover a large fraction at higher redshift that approaches the observed value. While the fraction of $R_{\rm vir}$ covered increases with redshift, Fig. 4.9 also shows that the physical area covered changes little.

Fig. 4.11 shows that the simulations match the cool gas column densities very well in the inner regions of the CGM. The simulations have trouble producing high enough HI column densities in the CGM outskirts.

This is a general discrepancy between observations and simulations that has not been solved: why there is so much cool gas at such large distances from galaxies? In an evolving galaxy there are two possibilities:

cool gas clouds are ejecta from the disk or gas cools at large distances and is in the early stages of accreting onto the galaxy.

Since the cool gas is not pressure supported, cooling condensations contribute to overcooling in simulations as the clouds fall onto the disk. It remains a mystery how clouds like those observed continue to be supported at large distances in the CGM, since they do not appear to contribute to star formation.

SPH simulations without a careful numerical treatment of hydrodynamics will overestimate these cooling condensations (Maller and Bullock 2004). Such condensations are the numerical embodiment of the Field (1965) instability. Agertz et al. (2007) identified such blobs as a numerical problem in SPH that does not exist in grid simulations, where cool clouds are quickly destroyed when moving through a hot medium.

Hints to solve the mystery are coming from focused, high resolution simulations. Quataert et al. (2015) showed that magnetic fields can provide internal pressure for cool clouds and allow those cool clouds to survive for much longer times. High resolution simulations are also being used to understand how cool gas can be driven out of galaxies. Scannapieco and Brüggen (2015) simulated cold gas clouds in supersonic flows and found that they survived longer than clouds in subsonic flows because the shock front suppresses the Kelvin-Helmholz instability. Such enhancements allow cold clouds to survive out to several kiloparsec from galaxies, but not hundreds of kiloparsec where HI is observed.

Brüggen and Scannapieco (2016) adds thermal electrons to the Scannapieco and Brüggen (2015) simulations. Conduction efficiently heats the cloud below a threshold density. When the cloud is more dense, it collapses into a dense filament that is able to radiate away any energy that conducts into its center, which also lengthens its lifetime. Adding to prior research, Thompson et al. (2015) take into account the rapid destruction of cool clouds entrained in a hot $\sim 10^7$ K outflow. They suggest that the cool gas in the CGM outskirts has two sources. An initial source is hot outflowing gas that radiatively cools. A secondary source is the gas that cools out of the shock front created as the wind plows into the CGM.

These modelers suggest that galactic winds include physics that is too difficult for simulations to model and provide prescriptions to include the physics in simulations. It is unclear whether it is possible to easily include such prescriptions. Faucher-Giguère et al. (2015) has shown promising results in fully self-consistent simulations using higher resolution. For instance, higher resolution adds a significant area of optically thick gas. Rahmati et al. (2015) were also able to match the HI column densities even at large distances from the galaxy using strong stellar and AGN feedback. Combining insights from both high resolution models and more advanced simulations can help to deepen our understanding of how the CGM is created and evolves.

4.5 Summary

We analysed the CGM of the NIHAO galaxy simulation suite, which includes 86 galaxies ranging in halo mass from $10^{9.7} - 10^{12.5}$ $M_\odot$. The galaxies follow the stellar mass–halo mass relation (Wang et al. 2015) and the disk gas–stellar mass relation (Stinson et al. 2015).

The hot and cold gas phases were examined using the commonly observed OVI and HI ions. We compared their column density profiles with observations, studied the covering fractions of dense HI, looked at the shape of the CGM and studied its chemical composition. Our goal was to present the simulations so that observers and modellers can compare with them in future studies.

We combined column densities of HI and OVI from all of the galaxies in NIHAO according to both the luminosity of the galaxy and impact parameter of the measured column density. Overall, the simulations provide a good match to observations. The column density of OVI increases as a function of galaxy luminosity to a plateau. Observations are still too sparse to make definite conclusions, but the simulations seem to follow the same functional form. Using an updated self-shielding approximation (Rahmati et al. 2013), the simulated HI column densities follow observations more closely than OVI. At $z = 3$, optically thick HI covers the same fraction of $R_{\rm vir}$ as the observations.

In addition to the successes of the simulations, two problems common to many numerical simulations are apparent. While the trend of the OVI simulations with luminosity agrees with observations, its normalization is about 0.7 dex too low, a trend commonly seen in simulations (e.g. Hummels et al. 2013; Ford et al. 2015; Suresh et al. 2015). In S12, this discrepancy was not as apparent, since they examined just two galaxies and used a slightly stronger feedback model than what was used in NIHAO. We do not propose using stronger feedback to create more OVI because it would reduce star formation too much. Instead, we point to the large amount of oxygen present in the CGM and conclude that our OVI ionization fraction is incorrect, possibly due to the temperature structure of the CGM.

Second, the extent of optically thick HI ($\log N_{\rm HI} > 17.2$) covers too small a fraction of the projected area, particularly between $R_{\rm vir}$ and $2R_{\rm vir}$. The source of the large amount of cool gas observed in the outer CGM and how it stays out there remains unknown. Unfortunately, our simulations shed little new light on the mystery. We simply note that that optically thick HI covers the same physical area as a function of galaxy halo mass at all redshifts in the simulations.

Given the similarity of the simulations and observations, we extend our analysis to the outflows that transport gas and metal enrichment to the CGM. Specifically, we recreate observations of gas velocity dispersion around edge-on disks. Wild et al. (2014) proposed that heightened velocity dispersions perpendicular to the disk with respect to the velocity dispersion in the disk plane are evidence for bipolar outflows. We detect a signal

in intermediate mass galaxies ($10 \lesssim \log M_{\rm Halo}/\,{\rm M}_\odot \lesssim 11.5$), though the ratio never exceeds two. Such enhanced velocity dispersions are visible in maps out to around 40 kpc in this halo mass range. 40 kpc is the same distance to which Bordoloi et al. (2014) observes outflows. Beyond 40 kpc, the velocity dispersion signal is isotropic. Larger halos do not show this signal, since their inner CGM is dominated by an extended gas disk which lies in the plane of the stellar disk.

Given the weak outflow signal, it is perhaps no surprise that it is hard to find any evidence for bipolar shapes in our simulations. Using the inertia tensor, we studied the shape distribution for three different gas temperatures. The hot ($T > 10^6$ K) gas showed a somewhat bipolar shape in the lowest mass simulations. The direction of the long axis was uncorrelated with the disk angular momentum axis. So, at $z = 0$, bipolar outflows do not make up a dominant mass component of the CGM. Rather, the CGM shape is mostly spherical because of virialization and the interaction of outflows with the ambient CGM. The cool ($T < 10^4$ K) CGM is an extended disk, while warm gas ($3 \times 10^4 < T/{\rm K} < 3 \times 10^5$) is always spherical.

The chemical enrichment of both the disk and the halo follow expected monotonically increasing trends. The mass fractions of HI, metals, oxygen and OVI can be well fit with power laws as a function of halo mass. The power law fits might be useful in galaxy formation models that do not use full hydrodynamics, such as semi-analytical models. Most notably, there is much more oxygen than what is shown as OVI, so fixing the OVI problem is not a transport problem, but an ionization problem.

Our analysis here focused on the $z = 0$ universe. More work is necessary to put these results into context of the high redshift universe.

5

Simulating a metallicity-dependent initial mass function[†]

To conclude our analysis of feedback, we will delve deeper into the fundamental interactions of gas cooling, star formation and stellar feedback. At the heart of star formation lies the IMF. It governs the subsequent stellar evolution and chemical enrichment of a galaxy. In this chapter, we use the simulation code AREPO as a testbed for a model of IMF non-universality. In particular, we compare a constant Chabrier and a varying metallicity-dependent initial mass function (IMF) in zoom-in simulations of Milky Way-sized halos. We find that constraints on stellar-to-halo mass ratios, feedback strength, metallicity evolution and metallicity distributions are in part degenerate with the effects of a non-universal, metallicity-dependent IMF. Interestingly, the empirical relation we use between metallicity and the high mass slope of the IMF does not aid in the quenching process. Additionally, the enrichment history and the $z = 0$ metallicity distribution are significantly affected.

5.1 Introduction

The majority of stars are known to form in shared star formation (SF) regions known as embedded clusters (Lada and Lada 2003; Kroupa et al. 2005; Megeath et al. 2016). The cause of this is assumed to be the collapse of giant molecular clouds (GMC) where many stars form simultaneously. This implies a distribution of stellar masses originating from each collapse, the stellar initial mass function (IMF). An unanswered question

[†] The contents of this chapter was submitted for publication in similar form in Gutcke and Springel (2017)

in stellar and galaxy formation physics is whether the IMF is universal, i.e. whether the distribution is the same in each star forming region or varies systematically with some dependency on its environment.

The details of the physics governing the regulation of star formation are poorly understood, since it is still unclear to what degree radiation, turbulence, magnetic fields, and instantaneous feedback from the forming young stars are able to counteract a pure gravitational collapse model. But observations of the Milky Way (MW) Galaxy, including resolved imaging of individual stars in globular clusters and the use of dwarf and giant sensitive spectral features, are broadly in agreement with a universal IMF shape (Scalo 1986; Kroupa 2001; Chabrier 2003; Bastian et al. 2010; Hopkins 2013). Pioneering observational work on the IMF and a first functional fitting form were made by Salpeter (1955), who suggested a power law slope of 1.35. Later, Kroupa (2001) and Chabrier (2003) added a low mass turn over to this basic model.

Studies of other galaxies yielded varying results. Some are consistent with the results from the MW (Kroupa 2002; Chabrier 2003; Kirk and Myers 2011; Bastian et al. 2011). But recently, some evidence for IMF variations has emerged, especially in early-type galaxies (e.g. Hoversten and Glazebrook 2008; Meurer et al. 2009; Gunawardhana et al. 2011; Cappellari et al. 2013). Studying resolved star clusters in M31, Weisz et al. (2015) found a steeper high-mass power law slope of (1.45 ± 0.05). We note that this is still consistent within the uncertainties for the high-mass slope reported by Kroupa (2001) of (1.3 ± 0.7). Martín-Navarro et al. (2015) used a sample of CALIFA elliptical galaxies to demonstrate a dependency of the IMF on the metallicity of the gas from which the stars formed. They use the dwarf-to-giant ratio and allowed the high-mass slope, $\Gamma_{\rm b}$, of the Vazdekis IMF (Vazdekis et al. 1996) to vary.

La Barbera et al. (2013) attempt to put constraints on the IMF using a large spectroscopic sample of early-type galaxies from the SPIDER survey. Their primary conclusion is that they find a correlation between the IMF slope Γ and the central velocity dispersion, σ_0. Spiniello et al. (2014) use a set of galaxies from the MILES library of stellar spectra that show a dependency of the IMF slope on the global velocity dispersion.

Chabrier et al. (2014) examine the evidence in the literature supporting a variable IMF in "extreme starburst environments" and in massive early-type galaxies (ETGs). They show that ETGs sport spectral absorption features, larger mass-to-light ratios and larger $[\alpha/\mathrm{Fe}]$ than spiral galaxies. ETGs therefore are assumed to host more low-mass stars such as M dwarfs. The authors postulate that these local ETGs evolved from small, compact dense progenitors between $z \sim 3 - 5$. These very compact systems were 10^3 times denser than the MW, had higher velocity dispersions and possibly higher temperatures. Also, these progenitors had different turbulent velocity than the MW, producing intense pressure and high accretion rates. The IMF in these "extreme starburst environments" is thus expected to be bottom-heavy with respect to the MW.

Simulations have also been used to study the effect of an IMF variation on the properties of galaxies. Blancato et al. (2017) post-process the Illustris simulation to study the effects of an IMF dependency on local and global velocity dispersion and on the metallicity, finding that the hierarchical nature of massive galaxy assembly significantly complicates the interpretation of the observed trends.

Yan et al. (2017) build on the integrated galactic IMF (IGIMF) model (Kroupa and Weidner 2003a). This model defines the galaxy-wide IMF as the integration of both the local IMF of a single embedded star cluster and the cluster mass function. Smaller clusters can be "optimally sampled" from a universal local IMF, but given their total mass, will not produce any stars more massive than the cluster mass. The result for galaxies as a whole is that a universal local IMF can produce a IGIMF that varies.

Clauwens et al. (2016) also use the metallicity-dependent IMF from Martín-Navarro et al. (2015), applying it to a sample of SDSS galaxies to investigate the effect on total stellar mass and star formation rates. They find that a bottom-heavy IMF at late times can aid in the quenching process, speeding it up. Guszejnov et al. (2017) use the FIRE simulation suite to study the IMF variation caused by a number of different cloud collapse models, and show that only a protostellar feedback model produces small enough variations to be consistent with observations.

This chapter is organized as follows. §5.2 outlines the simulation code and physics, §5.3 describes the variable IMF model, §5.4 compares the Chabrier and variable IMF results, and §5.5 summarises our findings. We use the cosmological parameters from the most recent Planck results ($\Omega_\mathrm{m} = 0.31$, $\Omega_\mathrm{L} = 0.69$, $\Omega_\mathrm{b} = 0.0486$, $h = 0.677$, $\sigma_8 = 0.8159$, $n_s = 0.97$ Planck Collaboration et al. 2016). We assume solar metallicity, $Z_\odot$, to be 0.0127. We use the variable $R_\mathrm{vir}$to denote the radius inside which the average density is 200 times the critical density.

5.2 Numerical Simulations

We have run six zoom-in simulations of Milky Way mass galaxies ($\sim 10^{12} M_\mathrm{vir}$ at $z = 0$). The initial conditions are drawn from the Auriga zoom-in simulation project presented in Grand et al. (2017b), and correspond to their galaxy numbers 6, 9, 13, 16, 24, and 28. We use the magneto-hydrodynamical moving-mesh code AREPO (Springel 2010) with a physics setting that differs slightly from the Auriga project with respect to parameters used for black hole seeding, active galactic nuclei feedback, and galactic winds. In particular, we use here the updated yield tables introduced in the IllustrisTNG simulation (Pillepich et al. 2018; Naiman et al. 2017) project. These changes in the details of the physics implementation with respect to Auriga are however immaterial for the qualitative results of our simulations. Nevertheless, to differentiate the true Auriga galaxies from our re-simulations also in the universal IMF case (which have slightly different physics), we will henceforth call our galaxies

"Halo-X", where 'X' denotes the corresponding number 6, 9, 13, 16, 24 and 28 in the Auriga project.

The IMF slope effects both the SNII rate and the AGB wind metal enrichment. The SNII rate at a given timestep is determined by

$$N_{\rm SNII}(t, \Delta t) = \int_{M_{\rm low}}^{M_{\rm high}} \Phi(m)\, {\rm d}m. \tag{5.1}$$

For SNII, $M_{\rm low} = \max[M(t + \Delta t), 8\,{\rm M}_\odot]$ and $M_{\rm high} = \min[M(t), 100\,{\rm M}_\odot]$, where $M(t, Z)$ is the inverted stellar lifetime function (see Vogelsberger et al. 2013, §2.3.1). The yields for AGB stars are taken from Karakas (2010) for $1 - 6\,{\rm M}_\odot$, and from Doherty et al. (2014) and Fishlock et al. (2014) for $7 - 7.5\,{\rm M}_\odot$. The SNII yields are taken from Portinari et al. (1998) for $6 - 13\,{\rm M}_\odot$ and $40 - 120\,{\rm M}_\odot$. For $13 - 40\,{\rm M}_\odot$, they are from Kobayashi et al. (2006).

The mass fraction of SNIa (in the range 1.4-8 $\rm M_\odot$) for different IMF is not changed in our model. Likewise, the "delay time distribution" function, $g(t)$, is taken in unmodified form from the Pillepich et al. (2018) model. Since the SNIa treatment does not explicitly take the IMF into account, the variable model does not affect it. It is nevertheless indirectly affected by the changed star formation history. The SNIa rate is computed as

$$\dot{N}_{Ia}(t) = \int_0^t \Psi(t') g(t - t')\, {\rm d}t', \tag{5.2}$$

where $\Psi(t')$ is the star formation rate and $g(t - t')$ is the delay time distribution (DTD) defined as

$$g(t) = \begin{cases} 0 & \text{if } t < 40{\rm Myr} \\ N_0 \left(\dfrac{t}{40{\rm Myr}} \right)^{-s} \dfrac{s-1}{40{\rm Myr},} & \text{if } t \geqslant 40{\rm Myr}. \end{cases} \tag{5.3}$$

The SNIa yields are taken from Nomoto et al. (1997).

The fiducial resolution level of the bulk of our simulations corresponds to "level 5" as tabulated in Grand et al. (2017b). We also run one "level 4" version of Auriga halo number 16 as a resolution test. The fiducial baseline IMF when universality is assumed is the Chabrier IMF (Chabrier 2003), which we compare with a simple metallicity-dependent IMF model described in the following section.

5.3 The variable IMF model

We use the relation derived in the study by Martín-Navarro et al. (2015) as the starting point of our simulations. The empirically derived relation between the high-mass slope of a Vazdekis IMF, $\Gamma_{\rm b}$, and the [M/H] of the gas is:

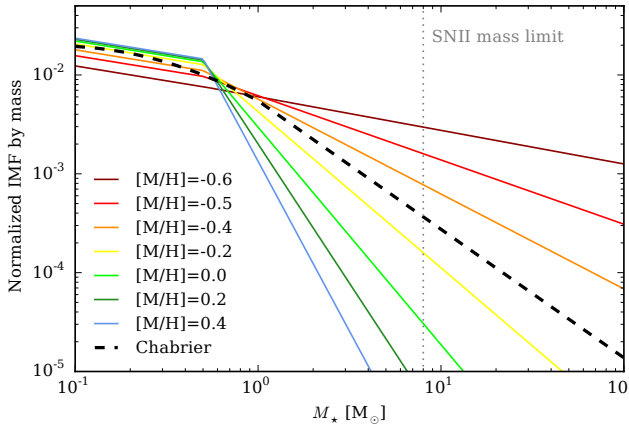

Figure 5.1. Illustration of the varying IMF (by mass) with different [M/H] values. The dashed black line is the Chabrier IMF. The grey dotted line indicates the lower mass limit for core collapse supernovae.

$$\Gamma_\mathrm{b} = 2.2(\pm0.1) + 3.1(\pm0.5) \times [\mathrm{M/H}]. \tag{5.4}$$

We use this relation, but combine it with the Kroupa IMF (Kroupa 2001) to define a metallicity dependent IMF as follows:

$$\Phi(m) \propto \begin{cases} m^{-0.3} & \text{for } 0.1 < m/\,\mathrm{M}_\odot \leq 0.5 \\ m^{-\Gamma_\mathrm{b}} & \text{for } 0.5 < m/\,\mathrm{M}_\odot < 100. \end{cases} \tag{5.5}$$

The integral of the IMF is normalized to the total initial stellar mass of a star particle, M_init. This mass has a resolution-dependent target value corresponding to our gas-cell resolution but can vary slightly around the target value as described in Vogelsberger et al. (2013). We extract the value for [M/H] from the simulation as

$$[\mathrm{M/H}] = \log_{10}\left(\frac{\sum \frac{M_\mathrm{Z}}{M_\mathrm{tot}}}{Z_\odot}\right), \tag{5.6}$$

summing over all Z above He.

In the following, we will use the terms “bottom-heavy” and “top-heavy” to refer to IMFs with large and small (or even negative) Γ_b, respectively. Given that each IMF is re-normalized to M_init, a steep high-mass slope will leave more stellar mass in the low-mass region. Thus, these terms only refer to the relative amount of M_init in the low-mass ($\lesssim 1\,\mathrm{M}_\odot$) and high-mass ($\gtrsim 1\,\mathrm{M}_\odot$) regions of the IMF.

Since the observations of IMF variations are as of yet inconclusive, the common choice made by most galaxy formation simulations is to assume universality (an Occam's razor argument). The primary goal of our present analysis is to assess the magnitude of potential changes in global galaxy properties that a variable IMF consistent with observations can produce. This then provides an approximate determination of the uncertainties associated with making the ad-hoc choice of a universal IMF.

Most simulations studying variable IMF models use simulations run with a constant IMF and post-process these to re-calculate galaxy properties assuming a variable IMF. These models cannot easily account for the non-linear effects caused by variability, i.e. for the changes in star formation rates and associated feedback resulting from variations in the enrichment history due to a different IMF. Thus, a second goal of our analysis is to understand such non-linear effects on the metallicity that a variable IMF can cause. Hence, we will investigate the enrichment history and the metallicity distribution functions (MDFs) of our simulated galaxies.

We note that Martín-Navarro et al. (2015) used early type galaxies to derive their empirical relation, whereas our study focuses on Milky Way-like spiral galaxies. While there is no direct evidence that the relation also applies to late type galaxies, we here shall assume that it does. Conceptually, this means that only one new parameter (in our case the metallicity of the star forming gas) is added when moving from the assumption of a fixed universal IMF to a universally varying IMF. This thus represents the next simplest model in which the variation of the IMF with metallicity is identical in all types of galaxies.

5.4 Results

5.4.1 Stellar mass evolution

Given the mutual self-regulated coupling of star formation and stellar feedback it is difficult to predict a priori whether our variable IMF simulations would produce more or less stellar mass than their Chabrier counterparts. Since metallicity is low at early times, the IMF in our model has a shallow slope then (being "top-heavy"), allowing for many high mass stars. These in turn produce a lot of core-collapse supernovae (SNII) and stellar feedback. The heating from the feedback can inhibit further star formation. On the other hand, the increase in high mass stars at early times also produces significant early enrichment in the gas. This enrichment steepens the IMF slope of subsequent generations of stars, thus decreasing the amount of feedback energy effecting the gas in subsequent cycles. A critical question then is, how long does it take to enrich the gas sufficiently that the IMF is truncated below $8\,\mathrm{M}_\odot$, the minimum mass of core-collapse supernovae. Once this occurs, both chemical enrichment and stellar feedback come largely to a halt. Since our IMF variations do not affect the total mass of a formed star particle but only the distribution of its mass (the mass

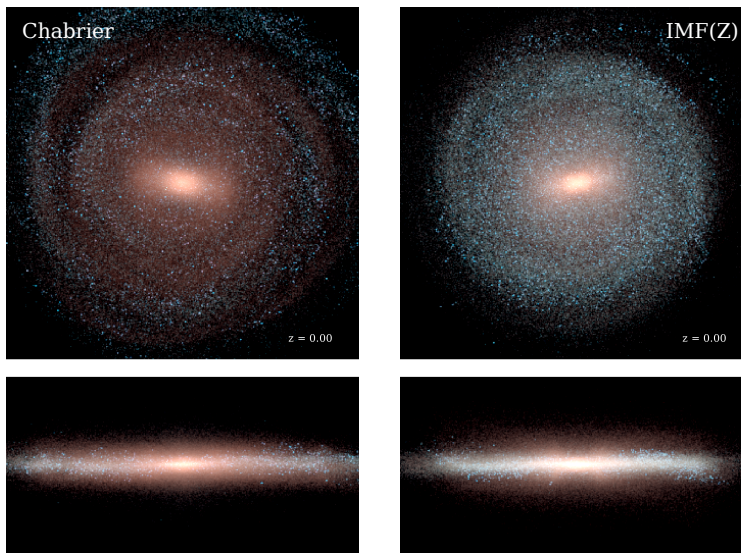

Figure 5.2. RGB images of Halo 16 for Chabrier IMF (left) and the metallicity dependent IMF (right). The galaxy is rotated to see the disk face-on in the upper panels, and edge-on in the lower panels. The images are 50 kpc wide. The K-, B-, and U-filters were mapped to RGB channels, respectively. We note that the photometric calculations assume a Chabrier IMF in both cases.

function), stellar mass build up can then proceed without the effect of feedback, due to the lack of high mass stars, and is solely regulated by the available gas reservoir after this point.

A bottom-heavy IMF and the resulting lack of stellar feedback has the further effect that less mass is returned to the interstellar medium (ISM) and becomes again available for subsequent star formation. Depending on the precise dependency of the IMF slope with metallicity, and on the efficiency of stellar feedback, these two processes can dominate at different times in a galaxy's life.

Fig. 5.2 shows $z = 0$ RGB images of Halo 16 in face-on and edge-on projections for both our models. The RGB channels use the K-, B- and U-filters based on the stellar population synthesis model by Bruzual and Charlot (2003). We note however that the image was created with the standard photometric calculation that assumes a Chabrier IMF, for simplicity. Thus, young stars (blue) are a bit brighter than they would self-consistently appear if the variable IMF was also used for making the image, since the variable model produces a bottom-heavy IMF at late times.

The upper panel in Fig. 5.3 gives an overview of the stellar mass evolution of our six halos. The black solid line is the evolution with the universal Chabrier IMF, while the red line is the variable IMF model. The dotted lines show Halo 16 at resolution level 4. In all cases, the variable IMF model produces more stellar mass at early times ($z \sim 2 - 3$) and keeps the lead for the entire evolution. The final stellar mass is a factor of 2-3 higher for the variable model in all model galaxies.

We stress that the feedback model was calibrated for the universal IMF and no adjustments were made to account for the variable IMF scenario. This means that the change in final stellar mass should only be interpreted as a relative change from model to model when only the IMF parameterization is changed, but other aspects of the model are left unchanged. Of course, if the variable IMF model was adopted as a new default description of the galaxy formation physics, the feedback strength would have to be re-calibrated. Increasing the feedback would likely again be able to match the stellar mass – halo mass relation.

The lower panel of Fig. 5.3 shows the star formation histories of our six halos. The star formation rates are higher at early times in the variable IMF case, but drop below the Chabrier model in all but one of our halos by $z = 0$. Due to the shortage of core-collapse SN after $z \sim 3$, the gas in the galaxy becomes calm and is not driven into outflows. Thus, it is consumed by SF quickly at that time. The stars formed have a bottom heavy IMF that stores much of the mass for times close to the Hubble time. Thus, SF then decreases, in most cases below the Chabrier level.

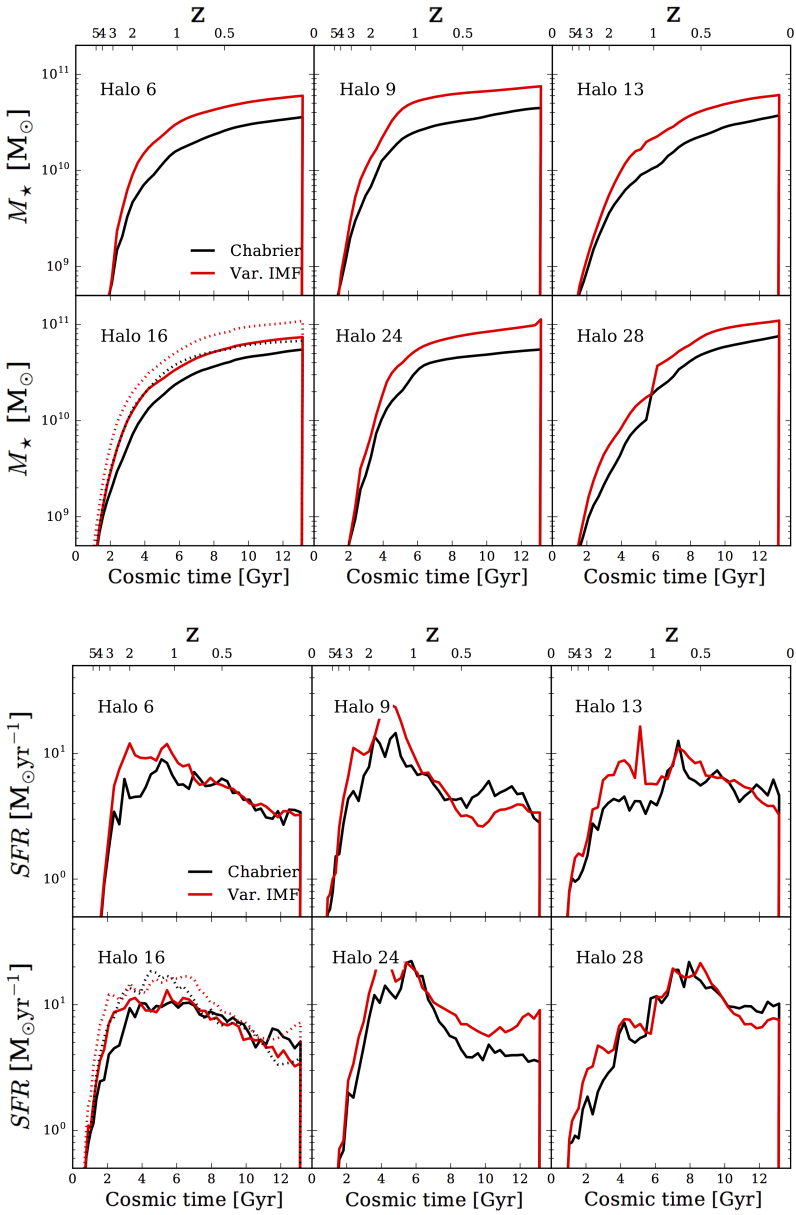

Figure 5.3. Stellar mass evolution (top) and star formation histories (bottom) for the six halos (initial conditions from the Auriga galaxies 6, 9, 13, 16, 24, 28). The black lines are the galaxies assuming a universal Chabrier IMF. The red lines are the same galaxies re-simulated with the metallicity-dependent IMF. The stellar mass is the sum of all star particle masses inside $R_{\rm vir}$at each timestep. The dotted lines in the panel with Halo 16 are the higher resolution versions of the same initial conditions.

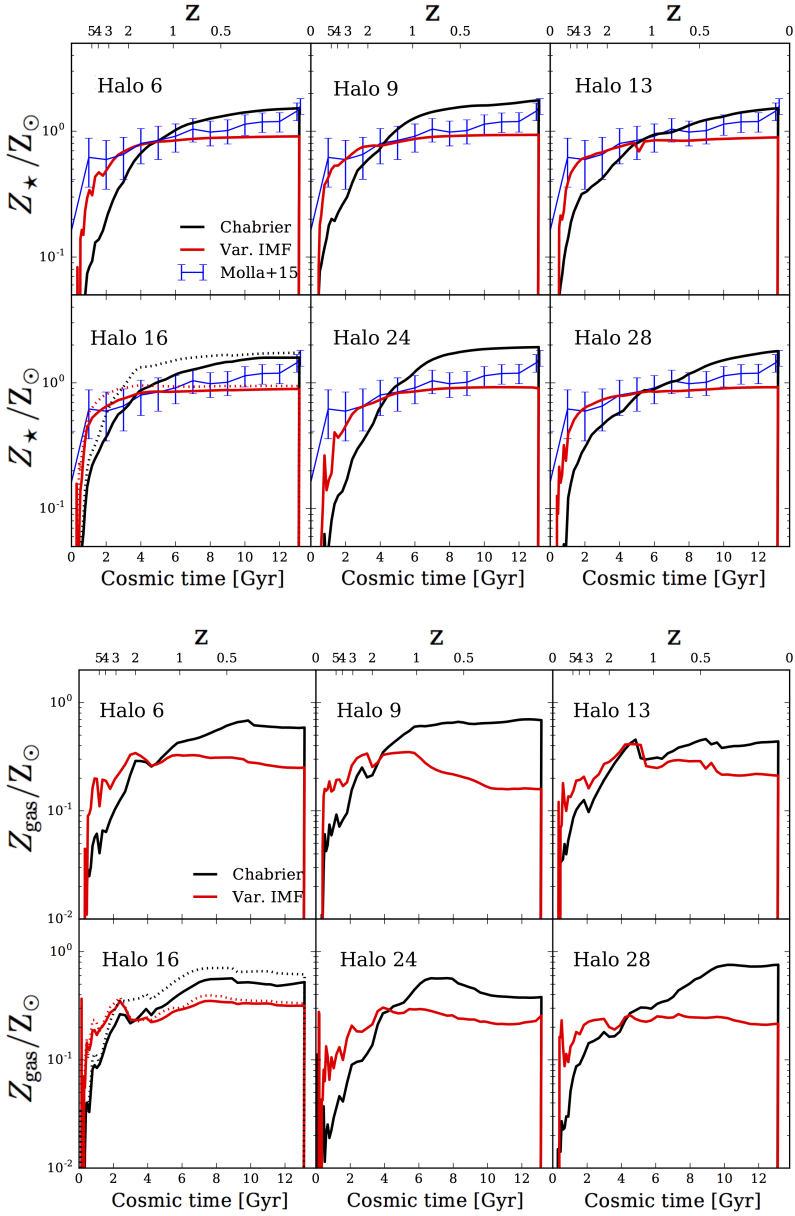

Figure 5.4. Total stellar (top) and gas (bottom) metallicity evolution of all stars within R_{vir} for each galaxy. Lines are the same as in Fig. 5.3. The blue error bars are the data points from Mollá et al. (2015), who compiled a variety observational studies of the Solar neighborhood.

5.4.2 Metallicity evolution

Stellar metallicity is what determines the IMF and subsequent evolution of each star particle. This is where the two IMF models show their most significant differences. The evolution of the total stellar metallicity of each halo is shown in the upper panel of Fig. 5.4. The blue line and error bars are the binned MW data compilation from Mollá et al. (2015). All six halos in the variable model increase their global metallicity dramatically in the first 2 Gyr. After that, the evolution flattens out and stays practically constant for the last 8 Gyr till $z = 0$. The compiled observations from Mollá et al. (2015) allow for such a rapid increase at early times. But by $z = 0$, the Chabrier value better matches the data.

The gas phase metallicity evolution across the entire halo is shown in the lower panel of Fig. 5.4 and sports the same change from Chabrier IMF to variable model. The total gas metallicity increases faster and earlier in the metallicity dependent case, and then slows its evolution, until no significant increase in total metallcity happens in the last 7-8 Gyr.

This similar trend in both the stellar and gas metallicity in the variable model can be explained by the change in IMF slope across time. Initially, the gas has a primordial composition, with no metals. Thus, the IMF allows for many high-mass stars that undergo core collapse within the first 1-2 Gyr. This increases the metallicity rapidly. After this first phase, the gas has been enriched and the subsequent generation of stars have IMFs with much steeper slopes and fewer high-mass stars. The strong enrichment stops and the metallcity of both gas and stars does not increase much further.

In Fig. 5.5, we compare our galaxy stellar metallicity to the observational data from Gallazzi et al. (2005) who used SDSS data. We match the observational selection by cutting the view at 5 kpc, which is the average physical size of the galaxies inside the SDSS fiber. The points show the ten most massive (and resolved) galaxies/satellites for each simulation. We compare Chabrier, Kroupa, Salpeter and variable IMF models. At low masses, we have added the MW satellite data from Kirby et al. (2010). At these low masses ($M_{\rm vir} < 10^8\,{\rm M}_\odot$), the universal IMF models match the data better. Interestingly, at higher masses (the highest being the MW-like galaxy itself), the results for the metallicity-dependent IMF are closer to the mean of the Gallazzi et al. (2005) data.

5.4.3 Metallicity distribution functions

The metallicity distribution functions (MDFs) of the stars and gas are a good way to track the changes caused by the variable IMF model, since the metallicity dependence causes non-linear effects in the metal production. The stellar MDFs are shown in Fig. 5.6. Both models produce distributions that peak around [M/H]$\simeq$ 0.0 dex, but the variable IMF model is distributed less towards high metallicity. This is caused by the lack of high-mass stars at late times, since the IMF drops off steeply. In both cases

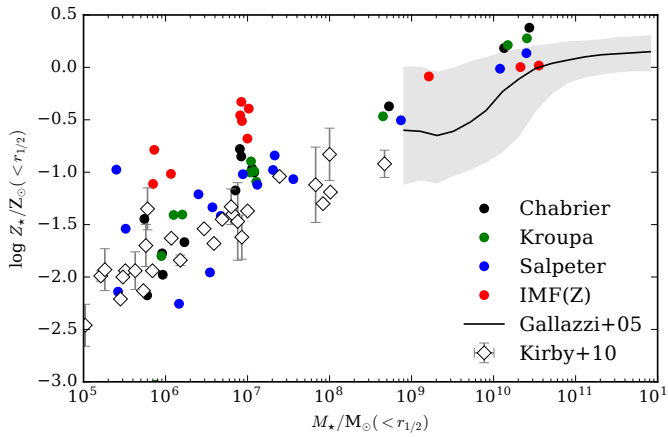

Figure 5.5. Stellar metallicity within the half mass radius, $r_{1/2}$, as a function of stellar mass. Dots represent the ten most massive halos/subhalos in the zoom simulation Halo 16. Three universal IMFs (Chabrier, Kroupa and Salpeter) and the metallicity dependent IMF are shown. The gray band shows the SDSS data from Gallazzi et al. (2005). Gray data with error bars show the MW dwarfs from Kirby et al. (2010).

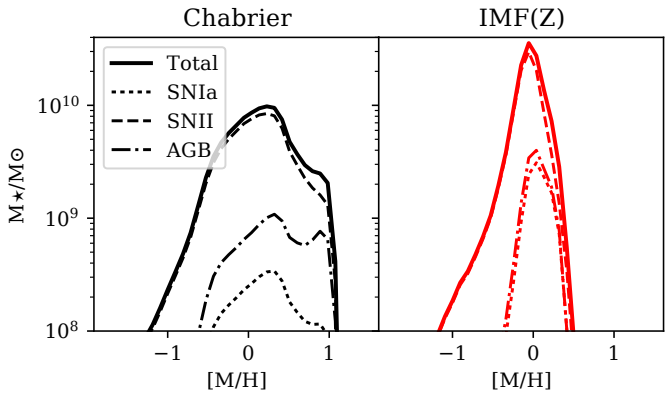

Figure 5.6. Stellar metallicity distribution function (solid line), split into contributions from SNIa (dotted), SNII (dashed) and AGB stars (dot-dashed). Shown is the $z = 0$ simulation output of Halo 16 (level 4).

Table 5.1. Fit parameters for the [α/Fe] – [Fe/H] relation with the linear function [α/Fe] = m · [Fe/H] + y_0. The fit parameters for the data after the APOGEE selection function are also shown, indicated by the index A.

Model	m	y_0	m_A	$y_{0,A}$
Chabrier	-0.21	0.36	-0.15	0.30
IMF(Z)	-0.77	0.02	-0.79	-0.09

the majority of metals are produced in core-collapse supernovae (SNII, dashed lines). In the Chabrier case, asymptotic giant branch stars (AGB) produce most of the remaining metals whereas SNIa contribute very little. In the variable IMF model, AGB and SNIa produce approximately the same amount.

5.4.4 α-Enhancement

The so-called α-enhancement is an important independent constraint on simulations. It has often been disregarded in the comparison with observations since it is difficult to match and depends on many factors in the simulations. In particular, it depends not only on the IMF, but also on the prescription for SNIa, the ratio of SNIa to SNII and, importantly, the yield sets used.

Marinacci et al. (2014) previously explored the α-abundance patterns predicted in AREPO simulations, finding a need to increase the SNIa rate by a factor of ~ 4 and being prompted to add fully metal-loaded winds to

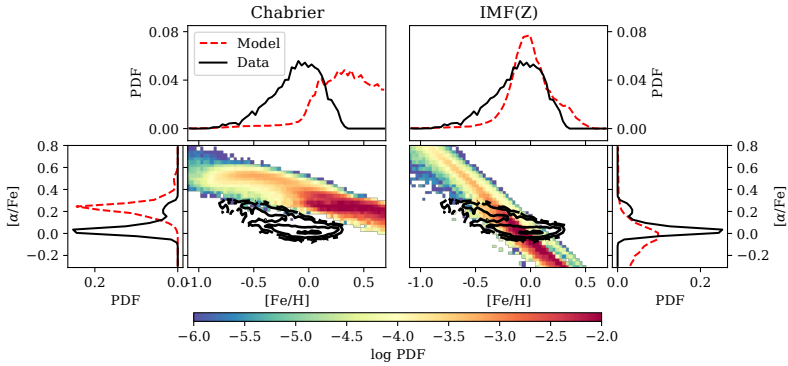

Figure 5.7. Distribution of simulated stars in the [α/Fe] vs [Fe/H] plane for Chabrier (left panels) and metallicity-dependent IMF (right panels). The black contours are the APOGEE data (Bovy et al. 2014; Ness et al. 2017). We attempt to mimic the age selection function of APOGEE. The spatial selection for both the model and APOGEE is the following: $5 > R_{\rm xy}/{\rm kpc} > 9$ and $|z|/{\rm kpc} < 1$. The bin width is set to 0.05 in abundance space for both axes. Shown is the $z = 0$ simulation result of Halo 16 (level 4).

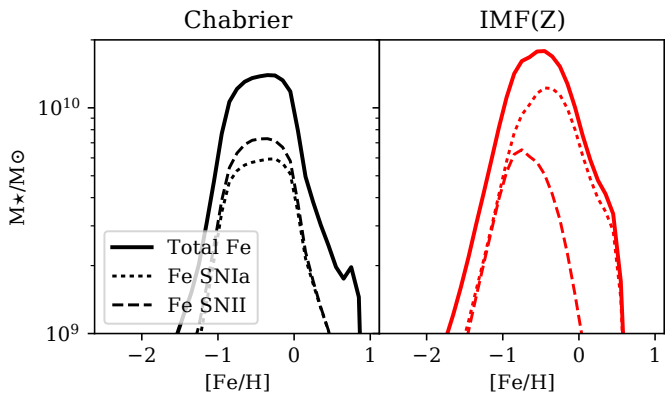

Figure 5.8. Distributions of [Fe/H] for Chabrier and metallicity-dependent IMF. Dotted lines show the iron component created in SNIa. Dashed lines show the iron from SNII. Displayed is the $z = 0$ simulation result of Halo 16 (level-4 resolution).

reproduce the slope of the observations. For a study of the α-abundances of the Auriga sample, see Grand et al. (2017a). We show the [α/Fe]-[Fe/H] plane in Fig. 5.7. Our estimate of α is calculated by averaging the metallicity contribution of oxygen, silicon and magnesium.

To compare our simulations with the Milky Way, we show data from the SDSS Apache Point Observatory Galactic Evolution Experiment (APOGEE), which is a high-resolution near-infrared spectroscopic survey (first presented in Bovy et al. 2014). The chemical abundances were updated to a homogeneous sample by Ness et al. (2017). We choose stars in the radial range $5 < R_{\rm GC}/{\rm kpc} < 9$, where $R_{\rm GC}$ is the distance to the Galactic center in the plane of the disk. The scale height is confined to $|z|/{\rm kpc} < 1$. APOGEE uses red clump stars and these have a strong age-dependent selection function, described in Bovy et al. (2014, their equation 11). We mimic this selection function when analyzing the simulation data, which is strongly biased towards young stars.

The left panels show the data for Chabrier, and the right ones for the metallicity dependent IMF. The colored images display the distribution of the simulation, while the overplotted black contours show the APOGEE data. The graphs to the top and sides are the one-dimensional histograms of the same data. Here the simulations are shown as red dashed lines, while APOGEE is given through black solid lines. The variable IMF model causes a significant change in the α-enhancement of the stars. The distribution becomes much steeper and the mean matches the data better. The shape and slope of the distribution in the Chabrier model seem to match the data more closely, but in this case the normalization is off by around 0.3 dex. We fit the slope of the [α/Fe]-[Fe/H] distribution with and without the APOGEE selection function. The fit results are noted in table 5.1. In the Chabrier case, the selection function causes the fit to be shallower, the slope being 0.21 without and 0.15 with it. This is opposite in the variable IMF case, where the slope becomes 0.79 with the age selection and 0.77 without.

We note that the bimodality in [α/Fe] of the Chabrier model is likely due to the age-selection, since the total distribution in the simulation does not show this trend. We assume that the overlapping functional forms of the SFH (which peaks at $z \sim 2$) and the age-dependent selection function (which peaks around $z \sim 0.15$) can cause an apparent dip in the distribution, making it seem bimodal.

In Fig. 5.8, we show the [Fe/H] distribution of stars in the entire halo. The dashed and dotted lines are the components of the distribution split by the channel in which the iron was produced. In the Chabrier model, SNIa and SNII produce approximately equal amounts of iron. In the variable IMF model, most of the metal-rich stars have their iron from SNIa alone. This difference in iron production is the driving factor that changes the α-enhancement between the two models. The increased iron production at late times (and high metallicity) brings the [α/Fe] ratio down to solar values and causes the steep dependence in the distribution.

5.5 Summary

The strength of energetic feedback from supernova and black holes is not well constrained by observations. Although simulations require some amount of feedback to control the run-away character of star formation and to match empirical relations such as the fundamental plane and the $M_\star - M_{\rm vir}$ relation, the (sub-grid) parameter choices used in simulations cannot be determined from first principle calculations but rather rely on empirical input. Variable IMF models add additional complications here, because their effects can be degenerate with the feedback models themselves. Thus far, theoretical investigations have largely sidestepped this problem and focussed on constraining feedback under the assumption of a universal IMF, for simplicity.

In this study, we investigate the effects of a metallicity-dependent IMF that is constrained by observations of a sample of ETGs from the CALIFA survey. We have quantified the differences exhibited by Milky Way analogues whose IMF varies with the total metallicity of the gas from which each star particle (representing a single stellar population) forms with respect to "standard" galaxies with a universal Chabrier IMF. We did not recalibrate the feedback strength or adjust any other parameters in the simulations, thus our results expose the effect of the variable IMF in isolation. This maximizes the corresponding effects and thus brackets the uncertainty due to a possible environmental dependence of the IMF.

One interesting outcome of our variable IMF model is that it produces too many stars to match the $M_\star - M_{\rm vir}$ relation. This results from a slight change of the star formation history, generally being higher than the Chabrier model around $z \sim 2-3$. This differs from the observational results by Clauwens et al. (2016), who show that a metallicity-dependent IMF can speed up the quenching process. They maintain that a lack of feedback at late times will cause a last burst of star formation that empties the gas reservoir. Our simulations do not show such a trend. Instead, late time SFRs vary between halos. Halos 9 and 28 show a slightly lower SFR compared to the Chabrier IMF in the last $\sim 2\,$Gyr. Whereas the SFR of Halo 6 does not significantly change and Halo 24 has $\sim 0.5\,$dex higher SFR since $z \sim 0.3$ (compared to the Chabrier IMF halos).

The most significant result is that the metallicity evolution rises faster and flattens out early, which produces lower total metallicities. The MDF of stars is then less broad and more peaked. We have investigated the metal production further by examining the α-abundance and its dependence on iron abundance. The corresponding distributions are broader in the variable IMF model, and even hint at a bimodality. To compare this accurately with observations, we mimic the selection function of stars in the APOGEE survey. This includes a spatial selection in the disk and in terms of the scale height. But since APOGEE observes primarily red clump stars, it also includes an age selection (see Bovy et al. 2014). The distribution in the [α/Fe]-[Fe/H] plane is strongly influenced by the

IMF model, with the slope of the relation being much steeper in the variable model. This model in fact matches the APOGEE data considerably better, since its mean is closer to the observed values. Although the Chabrier model does not pass through the data, its slope appears closer the data, but its normalization is too high by 0.3 dex. Overall, these results highlight the significant constraining power in detailed abundance patterns for fundamental questions in galaxy formation such as the degree of universality of the stellar IMF. More detailed simulation studies will be needed to fully understand the non-linear cross-talk between feedback modelling, chemical enrichment, and the variability of the IMF.

6

Summary & Outlook

The last two decades have seen significant development in our understanding of the buildup of galaxies through Cosmic time, especially in terms of their global properties and behavior. Galaxies appear bimodal in morphology as spiral disk galaxies and elliptical galaxies, in color between the blue cloud and the red sequence, and in specific star formation rate, between main sequence galaxies and quenched galaxies (Bell et al. 2004; Faber et al. 2007). The Hubble tuning fork (see Fig. 1.1) is considered to be an evolutionary sequence, where blue, spiral galaxies grow and age to become red ellipticals. To explain this progression, theoretical models need to account for a sudden change in dominant physical process.

Hydrodynamical simulations have shown that energetic feedback from stars, supernovae and active black holes can regulate star formation, keeping galaxies on the star formation main sequence. But neither stellar nor AGN feedback have strong observational support and neither is implemented from first principles in simulations. Thus it is significant that the amount of energy injected by feedback is so large that it stifles much detailed physics from other processes, such as magnetic fields, viscosity, conduction and metal diffusion (Su et al. 2017). A major hurdle to disentangling the relative dominance of all the processes active inside a galaxy is to pin down the strength of feedback. There is a crucial need for observationally and theoretically constraining the power of stellar and AGN feedback in galaxy evolution models.

To investigate the contribution of gas starvation to the formation of massive, quenched elliptical galaxies, I modified the smooth-particle hydrodynamic code GASOLINE2 to prevent gas cooling in the halo. In chapter 3, I showed that preventing halo gas from cooling onto $z = 2 - 3$ star forming galaxies can produce realistic elliptical galaxies by $z = 0$. The star formation is quenched in $\sim 1\,\mathrm{Gyr}$ by the lack of additional gas supplied to the galaxy. This result challenges previous work (Schawinski et al. 2007; Salim 2014) that claims that short quenching timescales cannot be

produced by starvation alone, but are necessarily powered by an additional quenching mechanism such as a quasar.

Through my work on quenching, I became aware of the observational and theoretical lack in constraining power on stellar and AGN feedback in galaxy evolution. The recent observations of the ionized CGM (Prochaska et al. 2011; Tumlinson et al. 2013), have given rise to a new avenue for constraining the possible strength of feedback. The evolution of galaxies and their gas halos has been proven to be strongly linked. The distribution of ionized gas throughout the halo provides valuable information on the nature of the feedback that heats and ejects gas from galaxies. However, these observations pose challenges to current simulations. Hydrodynamical simulations systematically under-predict the column density of ionized gas at large distances. The distribution of gas metallicities and ionization fractions throughout the halo provides valuable information on the strength and nature of the feedback that is heating and ejecting the gas from the galaxy. Allowing for self-shielding of HI in clouds, my simulations predict the correct amount of HI column density out to impact parameters of $\sim 200 - 300\,\mathrm{kpc}$. However, many state-of-the-art hydrodynamical simulations including cosmological boxes such as Illustris (Vogelsberger et al. 2014) and EAGLE (Crain et al. 2015), but also zoom-in suites such as NIHAO under-predict the column density of OVI at distances comparable to the virial radius (Hummels et al. 2013; Suresh et al. 2017; Gutcke et al. 2017b). This systematic mismatch is discussed in chapter 4 and it contains needed information to help understand feedback.

The question of feedback is affected by all aspects of the baryon cycle, many of which are not well understood or harbor large uncertainties. For example, the IMF greatly affects the stellar component of galaxies, which is at the same time the major observable constraint on galaxy evolution and feedback models. Numerous studies have presented evidence of systematic IMF variations based on observations of dwarf galaxies and massive elliptical galaxies (Hoversten and Glazebrook 2008; Meurer et al. 2009; Gunawardhana et al. 2011). At the same time, dwarfs and ellipticals inhabit the two galaxy mass regimes where feedback is at its strongest and the star formation efficiency at its lowest. Yet, theoretical work quantifying the implications of a variable IMF on galaxy evolution is still in early stages. In chapter 5, I showed that a change in the IMF, such as adding a dependency on metallicity, critically affects the total stellar mass and observables predicted by simulations. Thus, constraining feedback must take the possibility of IMF variations into account and I plan to study this further in my future work.

6.1 Outlook

There are multiple ways to pursue this line of investigation. First, it would be interesting to conduct further tests with empirical IMF dependencies

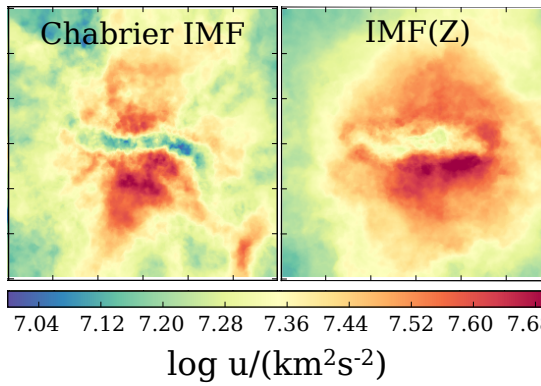

Figure 6.1. Energy density projection of the gas in two simulated galaxies ($M_{\rm halo} \sim 10^{12}\,{\rm M}_{\odot}$) viewed edge-on. The left galaxy evolved with a universal Chabrier IMF, while the right evolved with a metallicity-dependent IMF. Each image is 300 kpc × 300 kpc. The effect of different prescriptions is apparent on the energetic state of the CGM.

using AREPO, since it includes the full physics of star formation, metal enrichment, cooling, stellar and AGN feedback. In chapter 5, I implemented a metallicity-dependent IMF *without changing the feedback*. Next, I intend to readjust the feedback parameters to regain the correct final stellar mass and investigate the remaining effects of my variable model on galaxy evolution. Then, I plan to implement a suite of models that integrate further empirical IMF dependencies, testing these with zoom-in simulations. The IMF dependencies I plan to investigate are: metallicity (Martín-Navarro et al. 2015), pressure (Baugh et al. 2005), velocity dispersion (Spiniello et al. 2014) and the gravitational potential.

In a second step, it would be instructive to refine the star formation prescription. Most cosmological simulations model stars as massive simulation particles with identical masses. Therefore, single simulation particles act as a proxies for millions of actual stars. I plan to improve the state-of-the-art codes to model star particles as star clusters with varying masses. The cluster masses will be allowed to vary according to an empirically derived cluster mass function (CMF) such as that of Portegies Zwart et al. (2010): $M_{\rm cluster} \propto m^{-2}$. Each star cluster then obtains an internal IMF whose cut-off mass is unequivocally dictated by the total cluster mass. This sampling effect might be able to self-consistently mimic a varying IMF on local scales (Kroupa and Weidner 2003b), thus complying with observations of non-standard IMFs even if the IMF slope is universal. Additionally, the production of observable predictions through thorough simulation analysis and post-processing will be crucial to aptly compare with observational surveys, either validating or rejecting these IMF dependencies.

In a further step, I will take advantage of the high resolution simulations run with my new star formation prescription to study the effects of IMF variations on the CGM. Studying the small scale IMF and the large scale CGM simultaneously will allow me to bracket the effects of feedback between its primary producer, the high mass stars in the IMF, and its largest product, the kinematics and physical state of the CGM. In my preliminary work with a metallicity-dependent IMF, I found that the IMF alters the state of the CGM (see Fig. 6.1). In future work, I plan to use the new star formation models I develop to study the effects of IMF and feedback on the CGM. Specifically, I intend to study the enrichment timescales of the CGM and its kinematics. I will relate select star formation events to specific enriched CGM clouds in simulations, quantifying the travel time of ejected gas through the CGM and beyond the halo. To aptly compare with the COS observations, I want to investigate whether OVI has distinct kinematic properties, i.e. whether it is more likely to be entrained in inflows due to shock heating, as may be hinted at in my preliminary analysis of the CGM of elliptical galaxies.

7
Bibliography

First author publications by Thales A. Gutcke

T. A Gutcke and V. Springel. Simulating a metallicity-dependent initial mass function: Consequences for feedback and chemical abundances. *ArXiv e-prints*, October 2017.
This publication was used in this thesis.

T. A. Gutcke, A. V. Macciò, A. A. Dutton, and G. S. Stinson. Quenching versus quiescence: forming realistic massive ellipticals with a simple starvation model. *MNRAS*, 466:4614–4624, April 2017a. doi: 10.1093/mnras/stx005.
This publication was used in this thesis.

T. A. Gutcke, G. S. Stinson, A. V. Macciò, L. Wang, and A. A. Dutton. NIHAO - VIII. Circum-galactic medium and outflows - The puzzles of H I and O VI gas distributions. *MNRAS*, 464:2796–2815, January 2017b. doi: 10.1093/mnras/stw2539.
This publication was used in this thesis.

T. A. Gutcke, N. Fanidakis, A. V. Macciò, and C. Lacey. The star formation and AGN luminosity relation: predictions from a semi-analytical model. *MNRAS*, 451:3759–3767, August 2015. doi: 10.1093/mnras/stv1205.

Contributing author publications

O. Philcox, J. Rybizki, and T. A Gutcke. On the Optimal Choice of Nucleosynthetic Yields, IMF and Number of SN Ia for Chemical Evolution Modelling. *ArXiv e-prints*, December 2017.

A. A. Dutton, A. Obreja, L. Wang, T. A Gutcke, T. Buck, S. M. Udrescu, J. Frings, G. S. Stinson, X. Kang, and A. V. Macciò. NIHAO XII: galactic uniformity in a ΛCDM universe. *MNRAS*, 467:4937–4950, June 2017. doi: 10.1093/mnras/stx458.

L. Wang, A. A. Dutton, G. S. Stinson, A. V. Macciò, T. A Gutcke, and X. Kang. NIHAO VII: predictions for the galactic baryon budget in dwarf to Milky Way mass haloes. *MNRAS*, 466:4858–4867, April 2017. doi: 10.1093/mnras/stx066.

M. Tala, P. Heeren, M. Grill, R. J. Harris, J. Stürmer, C. Schwab, T. A Gutcke, S. Reffert, A. Quirrenbach, W. Seifert, H. Mandel, L. Geuer, L. Schäffner, G. Thimm, U. Seeman, J. Tietz, and K. Wagner. A high-resolution spectrograph for the 72cm Waltz Telescope at Landessternwarte, Heidelberg. In *Society of Photo-Optical Instrumentation Engineers (SPIE) Conference Series*, volume 9908 of *Proc. SPIE*, page 99086O, August 2016. doi: 10.1117/12.2232730.

E. Tollet, A. V. Macciò, A. A. Dutton, G. S. Stinson, L. Wang, C. Penzo, T. A Gutcke, T. Buck, X. Kang, C. Brook, A. Di Cintio, B. W. Keller, and J. Wadsley. NIHAO - IV: core creation and destruction in dark matter density profiles across cosmic time. *MNRAS*, 456:3542–3552, March 2016a. doi: 10.1093/mnras/stv2856.

A. A. Dutton, A. V. Macciò, G. S. Stinson, T. A Gutcke, C. Penzo, and T. Buck. The response of dark matter haloes to elliptical galaxy formation: a new test for quenching scenarios. *MNRAS*, 453:2447–2464, November 2015a. doi: 10.1093/mnras/stv1755.

C. Schwab, T. A Gutcke, J. F. P. Spronck, D. A. Fischer, and A. Szymkowiak. Investigating spectrograph design parameters with the Yale Doppler diagnostic facility. In *Ground-based and Airborne Instrumentation for Astronomy IV*, volume 8446 of *Proc. SPIE*, page 844695, September 2012. doi: 10.1117/12.926357.

References to other work

O. Agertz, B. Moore, J. Stadel, D. Potter, F. Miniati, J. Read, L. Mayer, A. Gawryszczak, A. Kravtsov, Å. Nordlund, F. Pearce, V. Quilis, D. Rudd, V. Springel, J. Stone, E. Tasker, R. Teyssier, J. Wadsley, and R. Walder. Fundamental differences between SPH and grid methods. *MNRAS*, 380: 963–978, September 2007. doi: 10.1111/j.1365-2966.2007.12183.x.

A. Aguirre, L. Hernquist, J. Schaye, N. Katz, D. H. Weinberg, and J. Gardner. Metal Enrichment of the Intergalactic Medium in Cosmological Simulations. *ApJ*, 561:521–549, November 2001. doi: 10.1086/323370.

M. Aumer, S. D. M. White, T. Naab, and C. Scannapieco. Towards a more realistic population of bright spiral galaxies in cosmological simulations. *MNRAS*, 434:3142–3164, October 2013. doi: 10.1093/mnras/stt1230.

I. K. Baldry, K. Glazebrook, J. Brinkmann, Ž. Ivezić, R. H. Lupton, R. C. Nichol, and A. S. Szalay. Quantifying the Bimodal Color-Magnitude Distribution of Galaxies. *ApJ*, 600:681–694, January 2004. doi: 10.1086/380092.

I. K. Baldry, M. L. Balogh, R. G. Bower, K. Glazebrook, R. C. Nichol, S. P. Bamford, and T. Budavari. Galaxy bimodality versus stellar mass and environment. *MNRAS*, 373:469–483, December 2006. doi: 10.1111/j.1365-2966.2006.11081.x.

N. Bastian, K. R. Covey, and M. R. Meyer. A Universal Stellar Initial Mass Function? A Critical Look at Variations. *ARA&A*, 48:339–389, September 2010. doi: 10.1146/annurev-astro-082708-101642.

N. Bastian, K. R. Covey, and M. R. Meyer. Looking for Systematic Variations in the Stellar Initial Mass Function. In C. Johns-Krull, M. K. Browning, and A. A. West, editors, *16th Cambridge Workshop on Cool Stars, Stellar Systems, and the Sun*, volume 448 of *Astronomical Society of the Pacific Conference Series*, page 361, December 2011.

C. M. Baugh, C. G. Lacey, C. S. Frenk, G. L. Granato, L. Silva, A. Bressan, A. J. Benson, and S. Cole. Can the faint submillimetre galaxies be explained in the Λ cold dark matter model? *MNRAS*, 356:1191–1200, January 2005. doi: 10.1111/j.1365-2966.2004.08553.x.

P. S. Behroozi, R. H. Wechsler, and C. Conroy. The Average Star Formation Histories of Galaxies in Dark Matter Halos from z = 0-8. *ApJ*, 770:57, June 2013. doi: 10.1088/0004-637X/770/1/57.

E. F. Bell, D. H. McIntosh, N. Katz, and M. D. Weinberg. The Optical and Near-Infrared Properties of Galaxies. I. Luminosity and Stellar Mass Functions. *ApJS*, 149:289–312, December 2003. doi: 10.1086/378847.

E. F. Bell, C. Wolf, K. Meisenheimer, H.-W. Rix, A. Borch, S. Dye, M. Kleinheinrich, L. Wisotzki, and D. H. McIntosh. Nearly 5000 Distant Early-Type Galaxies in COMBO-17: A Red Sequence and Its Evolution since z˜1. *ApJ*, 608:752–767, June 2004. doi: 10.1086/420778.

A. J. Benson, R. G. Bower, C. S. Frenk, C. G. Lacey, C. M. Baugh, and S. Cole. What Shapes the Luminosity Function of Galaxies? *ApJ*, 599:38–49, December 2003. doi: 10.1086/379160.

Y. Birnboim and A. Dekel. Virial shocks in galactic haloes? *MNRAS*, 345: 349–364, October 2003a. doi: 10.1046/j.1365-8711.2003.06955.x.

Y. Birnboim and A. Dekel. Virial shocks in galactic haloes? *MNRAS*, 345: 349–364, October 2003b. doi: 10.1046/j.1365-8711.2003.06955.x.

Y. Birnboim and A. Dekel. Gravitational quenching by clumpy accretion in cool-core clusters: convective dynamical response to overheating. *MNRAS*, 415:2566–2579, August 2011. doi: 10.1111/j.1365-2966.2011.18880.x.

K. Blancato, S. Genel, and G. Bryan. Implications of Galaxy Buildup for Putative IMF Variations in Massive Galaxies. *ApJ*, 845:136, August 2017. doi: 10.3847/1538-4357/aa7b84.

R. D. Blandford and R. L. Znajek. Electromagnetic extraction of energy from Kerr black holes. *MNRAS*, 179:433–456, May 1977. doi: 10.1093/mnras/179.3.433.

R. Bordoloi, S. J. Lilly, E. Hardmeier, T. Contini, J.-P. Kneib, O. Le Fevre, V. Mainieri, A. Renzini, M. Scodeggio, G. Zamorani, S. Bardelli, M. Bolzonella, A. Bongiorno, K. Caputi, C. M. Carollo, O. Cucciati, S. de la Torre, L. de Ravel, B. Garilli, A. Iovino, P. Kampczyk, K. Kovač, C. Knobel, F. Lamareille, J.-F. Le Borgne, V. Le Brun, C. Maier, M. Mignoli, P. Oesch, R. Pello, Y. Peng, E. Perez Montero, V. Presotto, J. Silverman, M. Tanaka, L. Tasca, L. Tresse, D. Vergani, E. Zucca, A. Cappi, A. Cimatti, G. Coppa, P. Franzetti, A. Koekemoer, M. Moresco, P. Nair, and L. Pozzetti. The Dependence of Galactic Outflows on the Properties and Orientation of zCOSMOS Galaxies at z ˜ 1. *ApJ*, 794:130, October 2014. doi: 10.1088/0004-637X/794/2/130.

J. Bovy, D. L. Nidever, H.-W. Rix, L. Girardi, G. Zasowski, S. D. Chojnowski, J. Holtzman, C. Epstein, P. M. Frinchaboy, M. R. Hayden, T. S. Rodrigues, S. R. Majewski, J. A. Johnson, M. H. Pinsonneault, D. Stello, C. Allende Prieto, B. Andrews, S. Basu, T. C. Beers, D. Bizyaev, A. Burton, W. J. Chaplin, K. Cunha, Y. Elsworth, R. A. García, D. A. García-Herńandez, A. E. García Pérez, F. R. Hearty, S. Hekker, T. Kallinger, K. Kinemuchi, L. Koesterke, S. Mészáros, B. Mosser, R. W. O'Connell, D. Oravetz, K. Pan, A. C. Robin, R. P. Schiavon, D. P. Schneider, M. Schultheis, A. Serenelli, M. Shetrone, V. Silva Aguirre, A. Simmons, M. Skrutskie, V. V. Smith, K. Stassun, D. H. Weinberg, J. C. Wilson, and O. Zamora. The APOGEE Red-clump Catalog: Precise Distances, Velocities, and High-resolution Elemental Abundances over a Large Area of the Milky Way's Disk. *ApJ*, 790:127, August 2014. doi: 10.1088/0004-637X/790/2/127.

R. G. Bower, A. J. Benson, R. Malbon, J. C. Helly, C. S. Frenk, C. M. Baugh, S. Cole, and C. G. Lacey. Breaking the hierarchy of galaxy formation. *MNRAS*, 370:645–655, August 2006. doi: 10.1111/j.1365-2966.2006.10519.x.

G. B. Brammer, K. E. Whitaker, P. G. van Dokkum, D. Marchesini, I. Labbé, M. Franx, M. Kriek, R. F. Quadri, G. Illingworth, K.-S. Lee, A. Muzzin, and G. Rudnick. The Dead Sequence: A Clear Bimodality in Galaxy Colors from z = 0 to z = 2.5. *ApJ*, 706:L173–L177, November 2009. doi: 10.1088/0004-637X/706/1/L173.

J. Brinchmann, S. Charlot, S. D. M. White, C. Tremonti, G. Kauffmann, T. Heckman, and J. Brinkmann. The physical properties of star-forming galaxies in the low-redshift Universe. *MNRAS*, 351:1151–1179, July 2004. doi: 10.1111/j.1365-2966.2004.07881.x.

M. Brüggen and E. Scannapieco. The Launching of Cold Clouds by Galaxy Outflows II: The Role of Thermal Conduction. *ArXiv e-prints 1602.01843*, February 2016.

G. Bruzual and S. Charlot. Stellar population synthesis at the resolution of 2003. *MNRAS*, 344:1000–1028, October 2003. doi: 10.1046/j.1365-8711.2003.06897.x.

M. Cappellari, R. M. McDermid, K. Alatalo, L. Blitz, M. Bois, F. Bournaud, M. Bureau, A. F. Crocker, R. L. Davies, T. A. Davis, P. T. de Zeeuw, P.-A. Duc, E. Emsellem, S. Khochfar, D. Krajnović, H. Kuntschner, R. Morganti, T. Naab, T. Oosterloo, M. Sarzi, N. Scott, P. Serra, A.-M. Weijmans, and L. M. Young. The ATLAS^{3D} project - XX. Mass-size and mass-σ distributions of early-type galaxies: bulge fraction drives kinematics, mass-to-light ratio, molecular gas fraction and stellar initial mass function. *MNRAS*, 432:1862–1893, July 2013. doi: 10.1093/mnras/stt644.

A. Cattaneo, A. Dekel, J. Devriendt, B. Guiderdoni, and J. Blaizot. Modelling the galaxy bimodality: shutdown above a critical halo mass. *MNRAS*, 370:1651–1665, August 2006. doi: 10.1111/j.1365-2966.2006.10608.x.

A. Cattaneo, S. M. Faber, J. Binney, A. Dekel, J. Kormendy, R. Mushotzky, A. Babul, P. N. Best, M. Brüggen, A. C. Fabian, C. S. Frenk, A. Khalatyan, H. Netzer, A. Mahdavi, J. Silk, M. Steinmetz, and L. Wisotzki. The role of black holes in galaxy formation and evolution. *Nature*, 460:213–219, July 2009. doi: 10.1038/nature08135.

R. Cen and N. E. Chisari. Star Formation Feedback and Metal-enrichment History of the Intergalactic Medium. *ApJ*, 731:11, April 2011. doi: 10.1088/0004-637X/731/1/11.

R. Cen and T. Fang. Where Are the Baryons? III. Nonequilibrium Effects and Observables. *ApJ*, 650:573–591, October 2006. doi: 10.1086/506506.

G. Chabrier. Galactic Stellar and Substellar Initial Mass Function. *PASP*, 115:763–795, July 2003. doi: 10.1086/376392.

G. Chabrier, P. Hennebelle, and S. Charlot. Variations of the Stellar Initial Mass Function in the Progenitors of Massive Early-type Galaxies and in Extreme Starburst Environments. *ApJ*, 796:75, December 2014. doi: 10.1088/0004-637X/796/2/75.

C. R. Christensen, R. Davé, F. Governato, A. Pontzen, A. Brooks, F. Munshi, T. Quinn, and J. Wadsley. In-N-Out: the gas cycle from dwarfs to spiral galaxies. *ArXiv e-prints 1508.00007*, July 2015.

S. Cielo, V. Antonuccio-Delogu, A. V. Macciò, A. D. Romeo, and J. Silk. 3D simulations of the early stages of AGN jets: geometry, thermodynamics and backflow. *MNRAS*, 439:2903–2916, April 2014. doi: 10.1093/mnras/stu161.

A. Cimatti, M. Brusa, M. Talia, M. Mignoli, G. Rodighiero, J. Kurk, P. Cassata, C. Halliday, A. Renzini, and E. Daddi. Active Galactic Nucleus Feedback at z ˜ 2 and the Mutual Evolution of Active and Inactive Galaxies. *ApJ*, 779: L13, December 2013. doi: 10.1088/2041-8205/779/1/L13.

B. Clauwens, J. Schaye, and M. Franx. Implications of a variable IMF for the interpretation of observations of galaxy populations. *MNRAS*, 462:2832–2846, November 2016. doi: 10.1093/mnras/stw1808.

L. L. Cowie and A. Songaila. Astrophysical Limits on the Evolution of Dimensionless Physical Constants over Cosmological Time. *ApJ*, 453:596, November 1995. doi: 10.1086/176422.

R. A. Crain, I. G. McCarthy, C. S. Frenk, T. Theuns, and J. Schaye. X-ray coronae in simulations of disc galaxy formation. *MNRAS*, 407:1403–1422, September 2010. doi: 10.1111/j.1365-2966.2010.16985.x.

R. A. Crain, J. Schaye, R. G. Bower, M. Furlong, M. Schaller, T. Theuns, C. Dalla Vecchia, C. S. Frenk, I. G. McCarthy, J. C. Helly, A. Jenkins, Y. M. Rosas-Guevara, S. D. M. White, and J. W. Trayford. The EAGLE simulations of galaxy formation: calibration of subgrid physics and model variations. *ArXiv e-prints*, January 2015.

N. H. M. Crighton, J. F. Hennawi, and J. X. Prochaska. Metal-poor, Cool Gas in the Circumgalactic Medium of a z = 2.4 Star-forming Galaxy: Direct Evidence for Cold Accretion? *ApJ*, 776:L18, October 2013. doi: 10.1088/2041-8205/776/2/L18.

N. H. M. Crighton, J. F. Hennawi, R. A. Simcoe, K. L. Cooksey, M. T. Murphy, M. Fumagalli, J. X. Prochaska, and T. Shanks. Metal-enriched, subkiloparsec gas clumps in the circumgalactic medium of a faint z = 2.5 galaxy. *MNRAS*, 446:18–37, January 2015. doi: 10.1093/mnras/stu2088.

D. J. Croton, V. Springel, S. D. M. White, G. De Lucia, C. S. Frenk, L. Gao, A. Jenkins, G. Kauffmann, J. F. Navarro, and N. Yoshida. The many lives of active galactic nuclei: cooling flows, black holes and the luminosities and colours of galaxies. *MNRAS*, 365:11–28, January 2006. doi: 10.1111/j.1365-2966.2005.09675.x.

H. D. Curtis. Modern Theories of the Spiral Nebulae. *J. R. Astron. Soc. Canada*, 14:317, October 1920.

E. Daddi, M. Dickinson, G. Morrison, R. Chary, A. Cimatti, D. Elbaz, D. Frayer, A. Renzini, A. Pope, D. M. Alexander, F. E. Bauer, M. Giavalisco, M. Huynh, J. Kurk, and M. Mignoli. Multiwavelength Study of Massive Galaxies at z˜2. I. Star Formation and Galaxy Growth. *ApJ*, 670:156–172, November 2007. doi: 10.1086/521818.

C. Dalla Vecchia and J. Schaye. Simulating galactic outflows with kinetic supernova feedback. *MNRAS*, 387:1431–1444, July 2008. doi: 10.1111/j.1365-2966.2008.13322.x.

C. Dalla Vecchia and J. Schaye. Simulating galactic outflows with thermal supernova feedback. *MNRAS*, 426:140–158, October 2012. doi: 10.1111/j.1365-2966.2012.21704.x.

C. W. Danforth, B. A. Keeney, E. M. Tilton, J. M. Shull, M. Stevans, M. M. Pieri, J. T. Stocke, B. D. Savage, K. France, D. Syphers, B. D. Smith, J. C. Green, C. Froning, S. V. Penton, and S. N. Osterman. An HST/COS Survey of the Low-Redshift IGM. I. Survey, Methodology, & Overall Results. *ArXiv e-prints 1402.2655*, February 2014.

R. Davé. The galaxy stellar mass-star formation rate relation: evidence for an evolving stellar initial mass function? *MNRAS*, 385:147–160, March 2008. doi: 10.1111/j.1365-2966.2008.12866.x.

R. Davé and B. D. Oppenheimer. The enrichment history of baryons in the Universe. *MNRAS*, 374:427–435, January 2007. doi: 10.1111/j.1365-2966.2006.11177.x.

R. Davé, K. Finlator, and B. D. Oppenheimer. Galaxy evolution in cosmological simulations with outflows - II. Metallicities and gas fractions. *MNRAS*, 416:1354–1376, September 2011. doi: 10.1111/j.1365-2966.2011.19132.x.

R. Davé, K. Finlator, and B. D. Oppenheimer. An analytic model for the evolution of the stellar, gas and metal content of galaxies. *MNRAS*, 421:98–107, March 2012. doi: 10.1111/j.1365-2966.2011.20148.x.

W. Dehnen and H. Aly. Improving convergence in smoothed particle hydrodynamics simulations without pairing instability. *MNRAS*, 425:1068–1082, September 2012. doi: 10.1111/j.1365-2966.2012.21439.x.

A. Dekel and Y. Birnboim. Galaxy bimodality due to cold flows and shock heating. *MNRAS*, 368:2–20, May 2006. doi: 10.1111/j.1365-2966.2006.10145.x.

A. Dekel and Y. Birnboim. Gravitational quenching in massive galaxies and clusters by clumpy accretion. *MNRAS*, 383:119–138, January 2008. doi: 10.1111/j.1365-2966.2007.12569.x.

A. Dekel and J. Silk. The origin of dwarf galaxies, cold dark matter, and biased galaxy formation. *ApJ*, 303:39–55, April 1986. doi: 10.1086/164050.

A. Di Cintio, C. B. Brook, A. V. Macciò, G. S. Stinson, A. Knebe, A. A. Dutton, and J. Wadsley. The dependence of dark matter profiles on the stellar-to-halo mass ratio: a prediction for cusps versus cores. *MNRAS*, 437:415–423, January 2014. doi: 10.1093/mnras/stt1891.

T. Di Matteo, V. Springel, and L. Hernquist. Energy input from quasars regulates the growth and activity of black holes and their host galaxies. *Nature*, 433:604–607, February 2005. doi: 10.1038/nature03335.

C. L. Doherty, P. Gil-Pons, H. H. B. Lau, J. C. Lattanzio, L. Siess, and S. W. Campbell. Super and massive AGB stars - III. Nucleosynthesis in metal-poor and very metal-poor stars - Z = 0.001 and 0.0001. *MNRAS*, 441:582–598, June 2014. doi: 10.1093/mnras/stu571.

F. Durier and C. Dalla Vecchia. Implementation of feedback in smoothed particle hydrodynamics: towards concordance of methods. *MNRAS*, 419:465–478, January 2012. doi: 10.1111/j.1365-2966.2011.19712.x.

A. A. Dutton and A. V. Macciò. Cold dark matter haloes in the Planck era: evolution of structural parameters for Einasto and NFW profiles. *MNRAS*, 441:3359–3374, July 2014. doi: 10.1093/mnras/stu742.

A. A. Dutton, A. V. Macciò, J. T. Mendel, and L. Simard. Universal IMF versus dark halo response in early-type galaxies: breaking the degeneracy with the Fundamental Plane. *MNRAS*, 432:2496–2511, July 2013. doi: 10.1093/mnras/stt608.

A. A. Dutton, A. V. Macciò, G. S. Stinson, T. A Gutcke, C. Penzo, and T. Buck. The response of dark matter haloes to elliptical galaxy formation: a new test for quenching scenarios. *MNRAS*, 453:2447–2464, November 2015a. doi: 10.1093/mnras/stv1755.

A. A. Dutton, A. V. Macciò, G. S. Stinson, T. A. Gutcke, C. Penzo, and T. Buck. The response of dark matter haloes to elliptical galaxy formation: a new test for quenching scenarios. *MNRAS*, 453:2447–2464, November 2015b. doi: 10.1093/mnras/stv1755.

A. A. Dutton, A. Obreja, L. Wang, T. A Gutcke, T. Buck, S. M. Udrescu, J. Frings, G. S. Stinson, X. Kang, and A. V. Macciò. NIHAO XII: galactic uniformity in a ΛCDM universe. *MNRAS*, 467:4937–4950, June 2017. doi: 10.1093/mnras/stx458.

D. K. Erb, A. E. Shapley, M. Pettini, C. C. Steidel, N. A. Reddy, and K. L. Adelberger. The Mass-Metallicity Relation at z>˜2. *ApJ*, 644:813–828, June 2006. doi: 10.1086/503623.

S. M. Faber, C. N. A. Willmer, C. Wolf, D. C. Koo, B. J. Weiner, J. A. Newman, M. Im, A. L. Coil, C. Conroy, M. C. Cooper, M. Davis, D. P. Finkbeiner, B. F. Gerke, K. Gebhardt, E. J. Groth, P. Guhathakurta, J. Harker, N. Kaiser, S. Kassin, M. Kleinheinrich, N. P. Konidaris, R. G. Kron, L. Lin, G. Luppino, D. S. Madgwick, K. Meisenheimer, K. G. Noeske, A. C. Phillips, V. L. Sarajedini, R. P. Schiavon, L. Simard, A. S. Szalay, N. P. Vogt, and R. Yan. Galaxy Luminosity Functions to z˜1 from DEEP2 and COMBO-17: Implications for Red Galaxy Formation. *ApJ*, 665:265–294, August 2007. doi: 10.1086/519294.

A. C. Fabian. Observational Evidence of Active Galactic Nuclei Feedback. *ARA&A*, 50:455–489, September 2012. doi: 10.1146/annurev-astro-081811-125521.

N. Fanidakis, C. M. Baugh, A. J. Benson, R. G. Bower, S. Cole, C. Done, and C. S. Frenk. Grand unification of AGN activity in the ΛCDM cosmology. *MNRAS*, 410:53–74, January 2011. doi: 10.1111/j.1365-2966.2010.17427.x.

C.-A. Faucher-Giguère, P. F. Hopkins, D. Kereš, A. L. Muratov, E. Quataert, and N. Murray. Neutral hydrogen in galaxy haloes at the peak of the cosmic star formation history. *MNRAS*, 449:987–1003, May 2015. doi: 10.1093/mnras/stv336.

C.-A. Faucher-Giguere, R. Feldmann, E. Quataert, D. Keres, P. F. Hopkins, and N. Murray. A Stellar Feedback Origin for Neutral Hydrogen in High-Redshift Quasar-Mass Halos. *ArXiv e-prints 1601.07188*, January 2016.

G. J. Ferland, K. T. Korista, D. A. Verner, J. W. Ferguson, J. B. Kingdon, and E. M. Verner. CLOUDY 90: Numerical Simulation of Plasmas and Their Spectra. *PASP*, 110:761–778, July 1998. doi: 10.1086/316190.

G. B. Field. Thermal Instability. *ApJ*, 142:531, August 1965. doi: 10.1086/148317.

C. K. Fishlock, A. I. Karakas, M. Lugaro, and D. Yong. Evolution and Nucleosynthesis of Asymptotic Giant Branch Stellar Models of Low Metallicity. *ApJ*, 797:44, December 2014. doi: 10.1088/0004-637X/797/1/44.

J. C. Forbes, M. R. Krumholz, A. Burkert, and A. Dekel. Balance among gravitational instability, star formation and accretion determines the structure and evolution of disc galaxies. *MNRAS*, 438:1552–1576, February 2014. doi: 10.1093/mnras/stt2294.

A. B. Ford, J. K. Werk, R. Dave, J. Tumlinson, R. Bordoloi, N. Katz, J. A. Kollmeier, B. D. Oppenheimer, M. S. Peeples, J. X. Prochaska, and D. H. Weinberg. Baryon Cycling in the Low-Redshift Circumgalactic Medium: A Comparison of Simulations to the COS-Halos Survey. *ArXiv e-prints 1503.02084*, March 2015.

M. Fumagalli, J. F. Hennawi, J. X. Prochaska, D. Kasen, A. Dekel, D. Ceverino, and J. Primack. Confronting Simulations of Optically Thick Gas in Massive Halos with Observations at z = 2-3. *ApJ*, 780:74, January 2014. doi: 10.1088/0004-637X/780/1/74.

J. M. Gabor and R. Davé. Hot gas in massive haloes drives both mass quenching and environment quenching. *MNRAS*, 447:374–391, February 2015. doi: 10.1093/mnras/stu2399.

Galaxy Zoo. Types of galaxies, February 2018. URL https://blog.galaxyzoo.org/2010/05/12/types-of-galaxies/.

A. Gallazzi, S. Charlot, J. Brinchmann, S. D. M. White, and C. A. Tremonti. The ages and metallicities of galaxies in the local universe. *MNRAS*, 362: 41–58, September 2005. doi: 10.1111/j.1365-2966.2005.09321.x.

R. Genzel, N. M. Förster Schreiber, P. Lang, S. Tacchella, L. J. Tacconi, S. Wuyts, K. Bandara, A. Burkert, P. Buschkamp, C. M. Carollo, G. Cresci, R. Davies, F. Eisenhauer, E. K. S. Hicks, J. Kurk, S. J. Lilly, D. Lutz, C. Mancini, T. Naab, S. Newman, Y. Peng, A. Renzini, K. Shapiro Griffin, A. Sternberg, D. Vergani, E. Wisnioski, E. Wuyts, and G. Zamorani. The SINS/zC-SINF Survey of z ˜ 2 Galaxy Kinematics: Evidence for Gravitational Quenching. *ApJ*, 785:75, April 2014. doi: 10.1088/0004-637X/785/1/75.

L. Girardi, B. F. Williams, K. M. Gilbert, P. Rosenfield, J. J. Dalcanton, P. Marigo, M. L. Boyer, A. Dolphin, D. R. Weisz, J. Melbourne, K. A. G. Olsen, A. C. Seth, and E. Skillman. The ACS Nearby Galaxy Survey Treasury. IX. Constraining Asymptotic Giant Branch Evolution with Old Metal-poor Galaxies. *ApJ*, 724:1030–1043, December 2010. doi: 10.1088/0004-637X/724/2/1030.

T. S. Gonçalves, D. C. Martin, K. Menéndez-Delmestre, T. K. Wyder, and A. Koekemoer. Quenching Star Formation at Intermediate Redshifts: Downsizing of the Mass Flux Density in the Green Valley. *ApJ*, 759:67, November 2012. doi: 10.1088/0004-637X/759/1/67.

V. González, I. Labbé, R. J. Bouwens, G. Illingworth, M. Franx, M. Kriek, and G. B. Brammer. The Stellar Mass Density and Specific Star Formation Rate of the Universe at z ˜ 7. *ApJ*, 713:115–130, April 2010. doi: 10.1088/0004-637X/713/1/115.

A. W. Graham, C. A. Onken, E. Athanassoula, and F. Combes. An expanded M_{bh}-σ diagram, and a new calibration of active galactic nuclei masses. *MNRAS*, 412:2211–2228, April 2011. doi: 10.1111/j.1365-2966.2010.18045.x.

R. J. J. Grand, S. Bustamante, F. A. Gómez, D. Kawata, F. Marinacci, R. Pakmor, H.-W. Rix, C. M. Simpson, M. Sparre, and V. Springel. Origin of chemically distinct discs in the Auriga cosmological simulations. *ArXiv e-prints*, August 2017a.

R. J. J. Grand, F. A. Gómez, F. Marinacci, R. Pakmor, V. Springel, D. J. R. Campbell, C. S. Frenk, A. Jenkins, and S. D. M. White. The Auriga Project: the properties and formation mechanisms of disc galaxies across cosmic time. *MNRAS*, 467:179–207, May 2017b. doi: 10.1093/mnras/stx071.

B. Groves, M. A. Dopita, R. S. Sutherland, L. J. Kewley, J. Fischera, C. Leitherer, B. Brandl, and W. van Breugel. Modeling the Pan-Spectral Energy Distribution of Starburst Galaxies. IV. The Controlling Parameters of the Starburst SED. *ApJS*, 176:438-456, June 2008. doi: 10.1086/528711.

K. Gültekin, D. O. Richstone, K. Gebhardt, T. R. Lauer, S. Tremaine, M. C. Aller, R. Bender, A. Dressler, S. M. Faber, A. V. Filippenko, R. Green, L. C. Ho, J. Kormendy, J. Magorrian, J. Pinkney, and C. Siopis. The M-σ and M-L Relations in Galactic Bulges, and Determinations of Their Intrinsic Scatter. *ApJ*, 698:198–221, June 2009. doi: 10.1088/0004-637X/698/1/198.

M. L. P. Gunawardhana, A. M. Hopkins, R. G. Sharp, S. Brough, E. Taylor, J. Bland-Hawthorn, C. Maraston, R. J. Tuffs, C. C. Popescu, D. Wijesinghe, D. H. Jones, S. Croom, E. Sadler, S. Wilkins, S. P. Driver, J. Liske, P. Norberg, I. K. Baldry, S. P. Bamford, J. Loveday, J. A. Peacock, A. S. G. Robotham, D. B. Zucker, Q. A. Parker, C. J. Conselice, E. Cameron, C. S. Frenk, D. T. Hill, L. S. Kelvin, K. Kuijken, B. F. Madore, B. Nichol, H. R. Parkinson, K. A. Pimbblet, M. Prescott, W. J. Sutherland, D. Thomas, and E. van Kampen. Galaxy and Mass Assembly (GAMA): the star formation rate dependence of the stellar initial mass function. *MNRAS*, 415:1647–1662, August 2011. doi: 10.1111/j.1365-2966.2011.18800.x.

Q. Guo, S. White, C. Li, and M. Boylan-Kolchin. How do galaxies populate dark matter haloes? *MNRAS*, 404:1111–1120, May 2010. doi: 10.1111/j.1365-2966.2010.16341.x.

D. Guszejnov, P. F. Hopkins, and X. Ma. Testing Models for IMF Variation in Milky Way-like Galaxies. *ArXiv e-prints*, February 2017.

T. A Gutcke and V. Springel. Simulating a metallicity-dependent initial mass function: Consequences for feedback and chemical abundances. *ArXiv e-prints*, October 2017.

T. A. Gutcke, N. Fanidakis, A. V. Macciò, and C. Lacey. The star formation and AGN luminosity relation: predictions from a semi-analytical model. *MNRAS*, 451:3759–3767, August 2015. doi: 10.1093/mnras/stv1205.

T. A. Gutcke, A. V. Macciò, A. A. Dutton, and G. S. Stinson. Quenching versus quiescence: forming realistic massive ellipticals with a simple starvation model. *MNRAS*, 466:4614–4624, April 2017a. doi: 10.1093/mnras/stx005.

T. A. Gutcke, G. S. Stinson, A. V. Macciò, L. Wang, and A. A. Dutton. NIHAO - VIII. Circum-galactic medium and outflows - The puzzles of H I and O VI gas distributions. *MNRAS*, 464:2796–2815, January 2017b. doi: 10.1093/mnras/stw2539.

F. Haardt and P. Madau. Modelling the UV/X-ray cosmic background with CUBA. In D. M. Neumann and J. T. V. Tran, editors, *Clusters of Galaxies and the High Redshift Universe Observed in X-rays*, 2001.

F. Haardt and P. Madau. Radiative Transfer in a Clumpy Universe. II. The Ultraviolet Extragalactic Background. *unpublished*, April 2005. doi: 10.1086/177035.

G. Hasinger. Absorption properties and evolution of active galactic nuclei. *A&A*, 490:905–922, November 2008. doi: 10.1051/0004-6361:200809839.

C. C. Hayward and P. F. Hopkins. How stellar feedback simultaneously regulates star formation and drives outflows. *ArXiv e-prints*, October 2015.

J. F. Hennawi, J. X. Prochaska, S. Burles, M. A. Strauss, G. T. Richards, D. J. Schlegel, X. Fan, D. P. Schneider, N. L. Zakamska, M. Oguri, J. E. Gunn, R. H. Lupton, and J. Brinkmann. Quasars Probing Quasars. I. Optically Thick Absorbers near Luminous Quasars. *ApJ*, 651:61–83, November 2006. doi: 10.1086/507069.

P. F. Hopkins. Variations in the stellar CMF and IMF: from bottom to top. *MNRAS*, 433:170–177, July 2013. doi: 10.1093/mnras/stt713.

P. F. Hopkins, E. Quataert, and N. Murray. Stellar feedback in galaxies and the origin of galaxy-scale winds. *MNRAS*, 421:3522–3537, April 2012. doi: 10.1111/j.1365-2966.2012.20593.x.

P. F. Hopkins, D. Kereš, J. Oñorbe, C.-A. Faucher-Giguère, E. Quataert, N. Murray, and J. S. Bullock. Galaxies on FIRE (Feedback In Realistic Environments): stellar feedback explains cosmologically inefficient star formation. *MNRAS*, 445:581–603, November 2014. doi: 10.1093/mnras/stu1738.

E. A. Hoversten and K. Glazebrook. Evidence for a Nonuniversal Stellar Initial Mass Function from the Integrated Properties of SDSS Galaxies. *ApJ*, 675:163-187, March 2008. doi: 10.1086/524095.

C. B. Hummels, G. L. Bryan, B. D. Smith, and M. J. Turk. Constraints on hydrodynamical subgrid models from quasar absorption line studies of the simulated circumgalactic medium. *MNRAS*, 430:1548–1565, April 2013. doi: 10.1093/mnras/sts702.

P. Jonsson. SUNRISE: polychromatic dust radiative transfer in arbitrary geometries. *MNRAS*, 372:2–20, October 2006. doi: 10.1111/j.1365-2966.2006.10884.x.

G. G. Kacprzak, S. Muzahid, C. W. Churchill, N. M. Nielsen, and J. C. Charlton. The Azimuthal Dependence of Outflows and Accretion Detected Using O VI Absorption. *ApJ*, 815:22, December 2015. doi: 10.1088/0004-637X/815/1/22.

R. Kannan, G. S. Stinson, A. V. Macciò, J. F. Hennawi, R. Woods, J. Wadsley, S. Shen, T. Robitaille, S. Cantalupo, T. R. Quinn, and C. Christensen. Galaxy formation with local photoionization feedback - I. Methods. *MNRAS*, 437:2882–2893, January 2014. doi: 10.1093/mnras/stt2098.

A. I. Karakas. Updated stellar yields from asymptotic giant branch models. *MNRAS*, 403:1413–1425, April 2010. doi: 10.1111/j.1365-2966.2009.16198.x.

N. Katz. Dissipational galaxy formation. II - Effects of star formation. *ApJ*, 391: 502–517, June 1992. doi: 10.1086/171366.

G. Kauffmann, T. M. Heckman, C. Tremonti, J. Brinchmann, S. Charlot, S. D. M. White, S. E. Ridgway, J. Brinkmann, M. Fukugita, P. B. Hall, Ž. Ivezić, G. T. Richards, and D. P. Schneider. The host galaxies of active galactic nuclei. *MNRAS*, 346:1055–1077, December 2003. doi: 10.1111/j.1365-2966.2003.07154.x.

B. W. Keller, J. Wadsley, S. M. Benincasa, and H. M. P. Couchman. A superbubble feedback model for galaxy simulations. *MNRAS*, 442:3013–3025, August 2014. doi: 10.1093/mnras/stu1058.

D. Kereš, N. Katz, D. H. Weinberg, and R. Davé. How do galaxies get their gas? *MNRAS*, 363:2–28, October 2005. doi: 10.1111/j.1365-2966.2005.09451.x.

D. Kereš, N. Katz, M. Fardal, R. Davé, and D. H. Weinberg. Galaxies in a simulated ΛCDM Universe - I. Cold mode and hot cores. *MNRAS*, 395: 160–179, May 2009. doi: 10.1111/j.1365-2966.2009.14541.x.

S. Khochfar and J. P. Ostriker. Adding Environmental Gas Physics to the Semianalytic Method for Galaxy Formation: Gravitational Heating. *ApJ*, 680:54-69, June 2008. doi: 10.1086/587470.

E. N. Kirby, P. Guhathakurta, J. D. Simon, M. C. Geha, C. M. Rockosi, C. Sneden, J. G. Cohen, S. T. Sohn, S. R. Majewski, and M. Siegel. Multi-element Abundance Measurements from Medium-resolution Spectra. II. Catalog of Stars in Milky Way Dwarf Satellite Galaxies. *ApJS*, 191:352–375, December 2010. doi: 10.1088/0067-0049/191/2/352.

H. Kirk and P. C. Myers. Young Stellar Groups and Their Most Massive Stars. *ApJ*, 727:64, February 2011. doi: 10.1088/0004-637X/727/2/64.

S. R. Knollmann and A. Knebe. AHF: Amiga's Halo Finder. *ApJS*, 182:608–624, June 2009. doi: 10.1088/0067-0049/182/2/608.

C. Kobayashi, H. Umeda, K. Nomoto, N. Tominaga, and T. Ohkubo. Galactic Chemical Evolution: Carbon through Zinc. *ApJ*, 653:1145–1171, December 2006. doi: 10.1086/508914.

J. A. Kollmeier, D. H. Weinberg, B. D. Oppenheimer, F. Haardt, N. Katz, R. Davé, M. Fardal, P. Madau, C. Danforth, A. B. Ford, M. S. Peeples, and J. McEwen. The Photon Underproduction Crisis. *ApJ*, 789:L32, July 2014. doi: 10.1088/2041-8205/789/2/L32.

A. Kravtsov, A. Vikhlinin, and A. Meshscheryakov. Stellar mass – halo mass relation and star formation efficiency in high-mass halos. *ArXiv e-prints*, January 2014.

P. Kroupa. On the variation of the initial mass function. *MNRAS*, 322:231–246, April 2001. doi: 10.1046/j.1365-8711.2001.04022.x.

P. Kroupa. The Initial Mass Function of Stars: Evidence for Uniformity in Variable Systems. *Science*, 295:82–91, January 2002. doi: 10.1126/science.1067524.

P. Kroupa and C. Weidner. Galactic-Field Initial Mass Functions of Massive Stars. *ApJ*, 598:1076–1078, December 2003a. doi: 10.1086/379105.

P. Kroupa and C. Weidner. Galactic-Field Initial Mass Functions of Massive Stars. *ApJ*, 598:1076–1078, December 2003b. doi: 10.1086/379105.

P. Kroupa, C. Theis, and C. M. Boily. The great disk of Milky-Way satellites and cosmological sub-structures. *A&A*, 431:517–521, February 2005. doi: 10.1051/0004-6361:20041122.

F. La Barbera, I. Ferreras, A. Vazdekis, I. G. de la Rosa, R. R. de Carvalho, M. Trevisan, J. Falcón-Barroso, and E. Ricciardelli. SPIDER VIII - constraints on the stellar initial mass function of early-type galaxies from a variety of spectral features. *MNRAS*, 433:3017–3047, August 2013. doi: 10.1093/mnras/stt943.

C. J. Lada and E. A. Lada. Embedded Clusters in Molecular Clouds. *ARA&A*, 41:57–115, 2003. doi: 10.1146/annurev.astro.41.011802.094844.

N. Lehner, J. M. O'Meara, A. J. Fox, J. C. Howk, J. X. Prochaska, V. Burns, and A. A. Armstrong. Galactic and Circumgalactic O VI and its Impact on the Cosmological Metal and Baryon Budgets at $2 < z <\tilde{} 3.5$. *ApJ*, 788:119, June 2014. doi: 10.1088/0004-637X/788/2/119.

C. Leitherer, D. Schaerer, J. D. Goldader, R. M. G. Delgado, C. Robert, D. F. Kune, D. F. de Mello, D. Devost, and T. M. Heckman. Starburst99: Synthesis Models for Galaxies with Active Star Formation. *ApJS*, 123:3–40, July 1999. doi: 10.1086/313233.

A. H. Maller and J. S. Bullock. Multiphase galaxy formation: high-velocity clouds and the missing baryon problem. *MNRAS*, 355:694–712, December 2004. doi: 10.1111/j.1365-2966.2004.08349.x.

P. Marigo, L. Girardi, A. Bressan, M. A. T. Groenewegen, L. Silva, and G. L. Granato. Evolution of asymptotic giant branch stars. II. Optical to far-infrared isochrones with improved TP-AGB models. *A&A*, 482:883–905, May 2008. doi: 10.1051/0004-6361:20078467.

F. Marinacci, R. Pakmor, V. Springel, and C. M. Simpson. Diffuse gas properties and stellar metallicities in cosmological simulations of disc galaxy formation. *MNRAS*, 442:3745–3760, August 2014. doi: 10.1093/mnras/stu1136.

M. Martig, F. Bournaud, R. Teyssier, and A. Dekel. Morphological Quenching of Star Formation: Making Early-Type Galaxies Red. *ApJ*, 707:250–267, December 2009. doi: 10.1088/0004-637X/707/1/250.

M. Martig, A. F. Crocker, F. Bournaud, E. Emsellem, J. M. Gabor, K. Alatalo, L. Blitz, M. Bois, M. Bureau, M. Cappellari, R. L. Davies, T. A. Davis, A. Dekel, P. T. de Zeeuw, P.-A. Duc, J. Falcón-Barroso, S. Khochfar, D. Krajnović, H. Kuntschner, R. Morganti, R. M. McDermid, T. Naab, T. Oosterloo, M. Sarzi, N. Scott, P. Serra, K. S. Griffin, R. Teyssier, A.-M. Weijmans, and L. M. Young. The ATLAS^{3D} project - XXII. Low-efficiency star formation in early-type galaxies: hydrodynamic models and observations. *MNRAS*, 432: 1914–1927, July 2013. doi: 10.1093/mnras/sts594.

C. L. Martin, A. E. Shapley, A. L. Coil, K. A. Kornei, K. Bundy, B. J. Weiner, K. G. Noeske, and D. Schiminovich. Demographics and Physical Properties of Gas Outflows/Inflows at $0.4 < z < 1.4$. *ApJ*, 760:127, December 2012. doi: 10.1088/0004-637X/760/2/127.

D. C. Martin, T. K. Wyder, D. Schiminovich, T. A. Barlow, K. Forster, P. G. Friedman, P. Morrissey, S. G. Neff, M. Seibert, T. Small, B. Y. Welsh, L. Bianchi, J. Donas, T. M. Heckman, Y.-W. Lee, B. F. Madore, B. Milliard, R. M. Rich, A. S. Szalay, and S. K. Yi. The UV-Optical Galaxy Color-Magnitude Diagram. III. Constraints on Evolution from the Blue to the Red Sequence. *ApJS*, 173:342–356, December 2007. doi: 10.1086/516639.

I. Martín-Navarro, A. Vazdekis, F. La Barbera, J. Falcón-Barroso, M. Lyubenova, G. van de Ven, I. Ferreras, S. F. Sánchez, S. C. Trager, R. García-Benito, D. Mast, M. A. Mendoza, P. Sánchez-Blázquez, R. González Delgado, C. J. Walcher, and The CALIFA Team. IMF-Metallicity: A Tight Local Relation Revealed by the CALIFA Survey. *ApJ*, 806:L31, June 2015. doi: 10.1088/2041-8205/806/2/L31.

L. Mayer, F. Governato, and T. Kaufmann. The formation of disk galaxies in computer simulations. *Advanced Science Letters*, 1:7–27, June 2008.

S. T. Megeath, R. Gutermuth, J. Muzerolle, E. Kryukova, J. L. Hora, L. E. Allen, K. Flaherty, L. Hartmann, P. C. Myers, J. L. Pipher, J. Stauffer, E. T. Young, and G. G. Fazio. The Spitzer Space Telescope Survey of the Orion A and B Molecular Clouds. II. The Spatial Distribution and Demographics of Dusty Young Stellar Objects. *AJ*, 151:5, January 2016. doi: 10.3847/0004-6256/151/1/5.

A. J. Mendez, A. L. Coil, J. Lotz, S. Salim, J. Moustakas, and L. Simard. AEGIS: The Morphologies of Green Galaxies at $0.4 < z < 1.2$. *ApJ*, 736:110, August 2011. doi: 10.1088/0004-637X/736/2/110.

G. R. Meurer, O. I. Wong, J. H. Kim, D. J. Hanish, T. M. Heckman, J. Werk, J. Bland-Hawthorn, M. A. Dopita, M. A. Zwaan, B. Koribalski, M. Seibert, D. A. Thilker, H. C. Ferguson, R. L. Webster, M. E. Putman, P. M. Knezek, M. T. Doyle, M. J. Drinkwater, C. G. Hoopes, V. A. Kilborn, M. Meyer, E. V. Ryan-Weber, R. C. Smith, and L. Staveley-Smith. Evidence for a Nonuniform Initial Mass Function in the Local Universe. *ApJ*, 695:765–780, April 2009. doi: 10.1088/0004-637X/695/1/765.

M. Mollá, O. Cavichia, M. Gavilán, and B. K. Gibson. Galactic chemical evolution: stellar yields and the initial mass function. *MNRAS*, 451:3693–3708, August 2015. doi: 10.1093/mnras/stv1102.

J. J. Monaghan. Smoothed particle hydrodynamics. *ARA&A*, 30:543–574, 1992. doi: 10.1146/annurev.aa.30.090192.002551.

B. P. Moster, T. Naab, and S. D. M. White. Galactic star formation and accretion histories from matching galaxies to dark matter haloes. *MNRAS*, 428:3121–3138, February 2013. doi: 10.1093/mnras/sts261.

A. L. Muratov, D. Kereš, C.-A. Faucher-Giguère, P. F. Hopkins, E. Quataert, and N. Murray. Gusty, gaseous flows of FIRE: galactic winds in cosmological simulations with explicit stellar feedback. *MNRAS*, 454:2691–2713, December 2015. doi: 10.1093/mnras/stv2126.

N. Murray, E. Quataert, and T. A. Thompson. On the Maximum Luminosity of Galaxies and Their Central Black Holes: Feedback from Momentum-driven Winds. *ApJ*, 618:569–585, January 2005. doi: 10.1086/426067.

S. J. Mutch, D. J. Croton, and G. B. Poole. The simplest model of galaxy formation - I. A formation history model of galaxy stellar mass growth. *MNRAS*, 435:2445–2459, November 2013. doi: 10.1093/mnras/stt1453.

J. P. Naiman, A. Pillepich, V. Springel, E. Ramirez-Ruiz, P. Torrey, M. Vogelsberger, R. Pakmor, D. Nelson, F. Marinacci, L. Hernquist, R. Weinberger, and S. Genel. First results from the IllustrisTNG simulations: A tale of two elements – chemical evolution of magnesium and europium. *ArXiv e-prints*, July 2017.

K. Nandra, A. Georgakakis, C. N. A. Willmer, M. C. Cooper, D. J. Croton, M. Davis, S. M. Faber, D. C. Koo, E. S. Laird, and J. A. Newman. AEGIS: The Color-Magnitude Relation for X-Ray-selected Active Galactic Nuclei. *ApJ*, 660:L11–L14, May 2007. doi: 10.1086/517918.

R. Narayan and I. Yi. Advection-dominated accretion: A self-similar solution. *ApJ*, 428:L13–L16, June 1994. doi: 10.1086/187381.

M. Ness, H. Rix, D. W. Hogg, A. R. Casey, J. Holtzman, M. Fouesneau, G. Zasowski, D. Geisler, M. Shetrone, D. Minniti, P. M. Frinchaboy, and A. Roman-Lopes. Galactic Doppelganger: The chemical similarity among field stars and among stars with a common birth origin. *ArXiv e-prints*, January 2017.

C. Nipoti, T. Treu, M. W. Auger, and A. S. Bolton. Can Dry Merging Explain the Size Evolution of Early-Type Galaxies? *ApJ*, 706:L86–L90, November 2009. doi: 10.1088/0004-637X/706/1/L86.

K. Nomoto, K. Iwamoto, N. Nakasato, F.-K. Thielemann, F. Brachwitz, T. Tsujimoto, Y. Kubo, and N. Kishimoto. Nucleosynthesis in type Ia supernovae. *Nuclear Physics A*, 621:467–476, February 1997. doi: 10.1016/S0375-9474(97)00291-1.

Aura C. Obreja, G. S. Stinson, A. A. Dutton, A. V. Macciò, L. Wang, and X. Kang. NIHAO VI. The hidden discs of simulated galaxies. *MNRAS, submitted*, December 2016.

B. D. Oppenheimer and R. Davé. Cosmological simulations of intergalactic medium enrichment from galactic outflows. *MNRAS*, 373:1265–1292, December 2006. doi: 10.1111/j.1365-2966.2006.10989.x.

B. D. Oppenheimer and R. Davé. Mass, metal, and energy feedback in cosmological simulations. *MNRAS*, 387:577–600, June 2008. doi: 10.1111/j.1365-2966.2008.13280.x.

B. D. Oppenheimer, R. Davé, D. Kereš, M. Fardal, N. Katz, J. A. Kollmeier, and D. H. Weinberg. Feedback and recycled wind accretion: assembling the z = 0 galaxy mass function. *MNRAS*, 406:2325–2338, August 2010. doi: 10.1111/j.1365-2966.2010.16872.x.

B. D. Oppenheimer, R. Davé, N. Katz, J. A. Kollmeier, and D. H. Weinberg. The intergalactic medium over the last 10 billion years - II. Metal-line absorption and physical conditions. *MNRAS*, 420:829–859, February 2012. doi: 10.1111/j.1365-2966.2011.20096.x.

B. D. Oppenheimer, R. A. Crain, J. Schaye, A. Rahmati, A. J. Richings, J. W. Trayford, J. Tumlinson, R. G. Bower, M. Schaller, and T. Theuns. Bimodality of low-redshift circumgalactic O VI in non-equilibrium EAGLE zoom simulations. *MNRAS*, 460:2157–2179, August 2016. doi: 10.1093/mnras/stw1066.

A. H. Pawlik and J. Schaye. TRAPHIC - radiative transfer for smoothed particle hydrodynamics simulations. *MNRAS*, 389:651–677, September 2008. doi: 10.1111/j.1365-2966.2008.13601.x.

A. H. Pawlik and J. Schaye. Multifrequency, thermally coupled radiative transfer with TRAPHIC: method and tests. *MNRAS*, 412:1943–1964, April 2011. doi: 10.1111/j.1365-2966.2010.18032.x.

P. J. E. Peebles. *The large-scale structure of the universe*. Princeton University Press, 1980.

M. S. Peeples, J. K. Werk, J. Tumlinson, B. D. Oppenheimer, J. X. Prochaska, N. Katz, and D. H. Weinberg. A Budget and Accounting of Metals at z ˜ 0: Results from the COS-Halos Survey. *ApJ*, 786:54, May 2014. doi: 10.1088/0004-637X/786/1/54.

Y.-j. Peng, S. J. Lilly, K. Kovač, M. Bolzonella, L. Pozzetti, A. Renzini, G. Zamorani, O. Ilbert, C. Knobel, A. Iovino, C. Maier, O. Cucciati, L. Tasca, C. M. Carollo, J. Silverman, P. Kampczyk, L. de Ravel, D. Sanders, N. Scoville, T. Contini, V. Mainieri, M. Scodeggio, J.-P. Kneib, O. Le Fèvre, S. Bardelli, A. Bongiorno, K. Caputi, G. Coppa, S. de la Torre, P. Franzetti, B. Garilli, F. Lamareille, J.-F. Le Borgne, V. Le Brun, M. Mignoli, E. Perez Montero, R. Pello, E. Ricciardelli, M. Tanaka, L. Tresse, D. Vergani, N. Welikala, E. Zucca, P. Oesch, U. Abbas, L. Barnes, R. Bordoloi, D. Bottini, A. Cappi, P. Cassata, A. Cimatti, M. Fumana, G. Hasinger, A. Koekemoer, A. Leauthaud, D. Maccagni, C. Marinoni, H. McCracken, P. Memeo, B. Meneux, P. Nair, C. Porciani, V. Presotto, and R. Scaramella. Mass and Environment as Drivers of Galaxy Evolution in SDSS and zCOSMOS and the Origin of the Schechter Function. *ApJ*, 721:193–221, September 2010. doi: 10.1088/0004-637X/721/1/193.

C. Penzo, A. V. Macciò, L. Casarini, G. S. Stinson, and J. Wadsley. Dark MaGICC: the effect of dark energy on disc galaxy formation. Cosmology does matter. *MNRAS*, 442:176–186, July 2014. doi: 10.1093/mnras/stu857.

C. Pfrommer, R. Pakmor, K. Schaal, C. M. Simpson, and V. Springel. Simulating cosmic ray physics on a moving mesh. *ArXiv e-prints*, April 2016.

O. Philcox, J. Rybizki, and T. A Gutcke. On the Optimal Choice of Nucleosynthetic Yields, IMF and Number of SN Ia for Chemical Evolution Modelling. *ArXiv e-prints*, December 2017.

A. Pillepich, V. Springel, D. Nelson, S. Genel, J. Naiman, R. Pakmor, L. Hernquist, P. Torrey, M. Vogelsberger, R. Weinberger, and F. Marinacci. Simulating galaxy formation with the IllustrisTNG model. *MNRAS*, 473:4077–4106, January 2018. doi: 10.1093/mnras/stx2656.

Planck Collaboration, P. A. R. Ade, N. Aghanim, C. Armitage-Caplan, M. Arnaud, M. Ashdown, F. Atrio-Barandela, J. Aumont, C. Baccigalupi, A. J. Banday, and et al. Planck 2013 results. XVI. Cosmological parameters. *A&A*, 571:A16, November 2014. doi: 10.1051/0004-6361/201321591.

Planck Collaboration, P. A. R. Ade, N. Aghanim, Y. Akrami, P. K. Aluri, M. Arnaud, M. Ashdown, J. Aumont, C. Baccigalupi, A. J. Banday, and et al. Planck 2015 results. XVI. Isotropy and statistics of the CMB. *A&A*, 594:A16, September 2016. doi: 10.1051/0004-6361/201526681.

A. Pontzen, R. Roškar, G. Stinson, and R. Woods. pynbody: N-Body/SPH analysis for python. Astrophysics Source Code Library, May 2013.

S. F. Portegies Zwart, S. L. W. McMillan, and M. Gieles. Young Massive Star Clusters. *ARA&A*, 48:431–493, September 2010. doi: 10.1146/annurev-astro-081309-130834.

L. Portinari, C. Chiosi, and A. Bressan. Galactic chemical enrichment with new metallicity dependent stellar yields. *A&A*, 334:505–539, June 1998.

D. J. Price. Modelling discontinuities and Kelvin Helmholtz instabilities in SPH. *Journal of Computational Physics*, 227:10040–10057, December 2008. doi: 10.1016/j.jcp.2008.08.011.

J. X. Prochaska, B. Weiner, H.-W. Chen, J. Mulchaey, and K. Cooksey. Probing the Intergalactic Medium/Galaxy Connection. V. On the Origin of Lyα and O VI Absorption at z $<$ 0.2. *ApJ*, 740:91, October 2011. doi: 10.1088/0004-637X/740/2/91.

J. X. Prochaska, J. F. Hennawi, and R. A. Simcoe. A Substantial Mass of Cool, Metal-enriched Gas Surrounding the Progenitors of Modern-day Ellipticals. *ApJ*, 762:L19, January 2013. doi: 10.1088/2041-8205/762/2/L19.

J. X. Prochaska, M. W. Lau, and J. F. Hennawi. Quasars Probing Quasars. VII. The Pinnacle of the Cool Circumgalactic Medium Surrounds Massive z ˜ 2 Galaxies. *ApJ*, 796:140, December 2014. doi: 10.1088/0004-637X/796/2/140.

E. Puchwein and V. Springel. Shaping the galaxy stellar mass function with supernova- and AGN-driven winds. *MNRAS*, 428:2966–2979, February 2013. doi: 10.1093/mnras/sts243.

E. Quataert, T. Heinemann, and A. Spitkovsky. Linear instabilities driven by differential rotation in very weakly magnetized plasmas. *MNRAS*, 447: 3328–3341, March 2015. doi: 10.1093/mnras/stu2483.

A. Rahmati, J. Schaye, A. H. Pawlik, and M. Raičević. "the impact of local stellar radiation on the h i column density distribution". *MNRAS*, 431:2261–2277, May 2013. doi: 10.1093/mnras/stt324.

A. Rahmati, J. Schaye, R. G. Bower, R. A. Crain, M. Furlong, M. Schaller, and T. Theuns. The distribution of neutral hydrogen around high-redshift galaxies and quasars in the EAGLE simulation. *MNRAS*, 452:2034–2056, September 2015. doi: 10.1093/mnras/stv1414.

A. Rahmati, J. Schaye, R. A. Crain, B. D. Oppenheimer, M. Schaller, and T. Theuns. Cosmic distribution of highly ionized metals and their physical conditions in the EAGLE simulations. *MNRAS*, 459:310–332, June 2016. doi: 10.1093/mnras/stw453.

M. J. Rees and J. P. Ostriker. Cooling, dynamics and fragmentation of massive gas clouds - Clues to the masses and radii of galaxies and clusters. *MNRAS*, 179:541–559, June 1977.

B. E. Robertson, A. V. Kravtsov, N. Y. Gnedin, T. Abel, and D. H. Rudd. Computational Eulerian hydrodynamics and Galilean invariance. *MNRAS*, 401:2463–2476, February 2010. doi: 10.1111/j.1365-2966.2009.15823.x.

V. Rodriguez-Gomez, A. Pillepich, L. V. Sales, S. Genel, M. Vogelsberger, Q. Zhu, S. Wellons, D. Nelson, P. Torrey, V. Springel, C.-P. Ma, and L. Hernquist. The stellar mass assembly of galaxies in the Illustris simulation: growth by mergers and the spatial distribution of accreted stars. *MNRAS*, 458: 2371–2390, May 2016. doi: 10.1093/mnras/stw456.

G. C. Rudie, C. C. Steidel, R. F. Trainor, O. Rakic, M. Bogosavljević, M. Pettini, N. Reddy, A. E. Shapley, D. K. Erb, and D. R. Law. The Gaseous Environment of High-z Galaxies: Precision Measurements of Neutral Hydrogen in the Circumgalactic Medium of z ˜ 2-3 Galaxies in the Keck Baryonic Structure Survey. *ApJ*, 750:67, May 2012. doi: 10.1088/0004-637X/750/1/67.

G. C. Rudie, C. C. Steidel, A. E. Shapley, and M. Pettini. The Column Density Distribution and Continuum Opacity of the Intergalactic and Circumgalactic Medium at Redshift langzrang = 2.4. *ApJ*, 769:146, June 2013. doi: 10.1088/0004-637X/769/2/146.

T. R. Saitoh and J. Makino. A Necessary Condition for Individual Time Steps in SPH Simulations. *ApJ*, 697:L99–L102, June 2009. doi: 10.1088/0004-637X/697/2/L99.

S. Salim. Green Valley Galaxies. *Serbian Astronomical Journal*, 189:1–14, December 2014. doi: 10.2298/SAJ1489001S.

S. Salim, R. M. Rich, S. Charlot, J. Brinchmann, B. D. Johnson, D. Schiminovich, M. Seibert, R. Mallery, T. M. Heckman, K. Forster, P. G. Friedman, D. C. Martin, P. Morrissey, S. G. Neff, T. Small, T. K. Wyder, L. Bianchi, J. Donas, Y.-W. Lee, B. F. Madore, B. Milliard, A. S. Szalay, B. Y. Welsh, and S. K. Yi. UV Star Formation Rates in the Local Universe. *ApJS*, 173:267–292, December 2007. doi: 10.1086/519218.

E. E. Salpeter. The Luminosity Function and Stellar Evolution. *ApJ*, 121:161, January 1955. doi: 10.1086/145971.

B. D. Savage, T.-S. Kim, B. P. Wakker, B. Keeney, J. M. Shull, J. T. Stocke, and J. C. Green. The Properties of Low Redshift Intergalactic O VI Absorbers Determined from High S/N Observations of 14 QSOs with the Cosmic Origins Spectrograph. *ApJS*, 212:8, May 2014. doi: 10.1088/0067-0049/212/1/8.

J. M. Scalo. The stellar initial mass function. *Fundamentals Cosmic Phys.*, 11: 1–278, May 1986.

E. Scannapieco and M. Brüggen. The Launching of Cold Clouds by Galaxy Outflows. I. Hydrodynamic Interactions with Radiative Cooling. *ApJ*, 805: 158, June 2015. doi: 10.1088/0004-637X/805/2/158.

K. Schawinski, D. Thomas, M. Sarzi, C. Maraston, S. Kaviraj, S.-J. Joo, S. K. Yi, and J. Silk. Observational evidence for AGN feedback in early-type galaxies. *MNRAS*, 382:1415–1431, December 2007. doi: 10.1111/j.1365-2966.2007.12487.x.

J. Schaye, A. Aguirre, T.-S. Kim, T. Theuns, M. Rauch, and W. L. W. Sargent. Metallicity of the Intergalactic Medium Using Pixel Statistics. II. The Distribution of Metals as Traced by C IV. *ApJ*, 596:768–796, October 2003. doi: 10.1086/378044.

J. Schaye, C. Dalla Vecchia, C. M. Booth, R. P. C. Wiersma, T. Theuns, M. R. Haas, S. Bertone, A. R. Duffy, I. G. McCarthy, and F. van de Voort. The physics driving the cosmic star formation history. *MNRAS*, 402:1536–1560, March 2010. doi: 10.1111/j.1365-2966.2009.16029.x.

J. Schaye, R. A. Crain, R. G. Bower, M. Furlong, M. Schaller, T. Theuns, C. Dalla Vecchia, C. S. Frenk, I. G. McCarthy, J. C. Helly, A. Jenkins, Y. M. Rosas-Guevara, S. D. M. White, M. Baes, C. M. Booth, P. Camps, J. F. Navarro, Y. Qu, A. Rahmati, T. Sawala, P. A. Thomas, and J. Trayford. The EAGLE project: simulating the evolution and assembly of galaxies and their environments. *MNRAS*, 446:521–554, January 2015. doi: 10.1093/mnras/stu2058.

D. Schiminovich, T. K. Wyder, D. C. Martin, B. D. Johnson, S. Salim, M. Seibert, M. A. Treyer, T. Budavári, C. Hoopes, M. Zamojski, T. A. Barlow, K. G. Forster, P. G. Friedman, P. Morrissey, S. G. Neff, T. A. Small, L. Bianchi, J. Donas, T. M. Heckman, Y.-W. Lee, B. F. Madore, B. Milliard, R. M. Rich, A. S. Szalay, B. Y. Welsh, and S. Yi. The UV-Optical Color Magnitude Diagram. II. Physical Properties and Morphological Evolution On and Off of a Star-forming Sequence. *ApJS*, 173:315–341, December 2007. doi: 10.1086/524659.

C. Schwab, T. A Gutcke, J. F. P. Spronck, D. A. Fischer, and A. Szymkowiak. Investigating spectrograph design parameters with the Yale Doppler diagnostic facility. In *Ground-based and Airborne Instrumentation for Astronomy IV*, volume 8446 of *Proc. SPIE*, page 844695, September 2012. doi: 10.1117/12.926357.

S. Shen, J. Wadsley, and G. Stinson. The enrichment of the intergalactic medium with adiabatic feedback - I. Metal cooling and metal diffusion. *MNRAS*, 407:1581–1596, September 2010. doi: 10.1111/j.1365-2966.2010.17047.x.

S. Shen, P. Madau, A. Aguirre, J. Guedes, L. Mayer, and J. Wadsley. The Origin of Metals in the Circumgalactic Medium of Massive Galaxies at z = 3. *ApJ*, 760:50, November 2012. doi: 10.1088/0004-637X/760/1/50.

D. Sijacki, V. Springel, T. Di Matteo, and L. Hernquist. A unified model for AGN feedback in cosmological simulations of structure formation. *MNRAS*, 380:877–900, September 2007. doi: 10.1111/j.1365-2966.2007.12153.x.

J. D. Silverman, V. Mainieri, B. D. Lehmer, D. M. Alexander, F. E. Bauer, J. Bergeron, W. N. Brandt, R. Gilli, G. Hasinger, D. P. Schneider, P. Tozzi, C. Vignali, A. M. Koekemoer, T. Miyaji, P. Popesso, P. Rosati, and G. Szokoly. The Evolution of AGN Host Galaxies: From Blue to Red and the Influence of Large-Scale Structures. *ApJ*, 675:1025-1040, March 2008. doi: 10.1086/527283.

R. J. Smethurst, C. J. Lintott, B. D. Simmons, K. Schawinski, P. J. Marshall, S. Bamford, L. Fortson, S. Kaviraj, K. L. Masters, T. Melvin, R. C. Nichol, R. A. Skibba, and K. W. Willett. Galaxy Zoo: evidence for diverse star formation histories through the green valley. *MNRAS*, 450:435–453, June 2015. doi: 10.1093/mnras/stv161.

R. S. Somerville, P. F. Hopkins, T. J. Cox, B. E. Robertson, and L. Hernquist. A semi-analytic model for the co-evolution of galaxies, black holes and active galactic nuclei. *MNRAS*, 391:481–506, December 2008. doi: 10.1111/j.1365-2966.2008.13805.x.

C. Spiniello, S. Trager, L. V. E. Koopmans, and C. Conroy. The stellar IMF in early-type galaxies from a non-degenerate set of optical line indices. *MNRAS*, 438:1483–1499, February 2014. doi: 10.1093/mnras/stt2282.

V. Springel. E pur si muove: Galilean-invariant cosmological hydrodynamical simulations on a moving mesh. *MNRAS*, 401:791–851, January 2010. doi: 10.1111/j.1365-2966.2009.15715.x.

V. Springel and L. Hernquist. The history of star formation in a Λ cold dark matter universe. *MNRAS*, 339:312–334, February 2003. doi: 10.1046/j.1365-8711.2003.06207.x.

V. Springel, S. D. M. White, A. Jenkins, C. S. Frenk, N. Yoshida, L. Gao, J. Navarro, R. Thacker, D. Croton, J. Helly, J. A. Peacock, S. Cole, P. Thomas, H. Couchman, A. Evrard, J. Colberg, and F. Pearce. Simulations of the formation, evolution and clustering of galaxies and quasars. *Nature*, 435:629–636, June 2005. doi: 10.1038/nature03597.

J. G. Stadel. *Cosmological N-body simulations and their analysis*. PhD thesis, UNIVERSITY OF WASHINGTON, 2001.

C. C. Steidel, D. K. Erb, A. E. Shapley, M. Pettini, N. Reddy, M. Bogosavljević, G. C. Rudie, and O. Rakic. The Structure and Kinematics of the Circumgalactic Medium from Far-ultraviolet Spectra of z ˜= 2-3 Galaxies. *ApJ*, 717:289–322, July 2010. doi: 10.1088/0004-637X/717/1/289.

G. Stinson, A. Seth, N. Katz, J. Wadsley, F. Governato, and T. Quinn. Star formation and feedback in smoothed particle hydrodynamic simulations - I. Isolated galaxies. *MNRAS*, 373:1074–1090, December 2006. doi: 10.1111/j.1365-2966.2006.11097.x.

G. S. Stinson, J. Bailin, H. Couchman, J. Wadsley, S. Shen, S. Nickerson, C. Brook, and T. Quinn. Cosmological galaxy formation simulations using smoothed particle hydrodynamics. *MNRAS*, 408:812–826, October 2010. doi: 10.1111/j.1365-2966.2010.17187.x.

G. S. Stinson, C. Brook, J. X. Prochaska, J. Hennawi, S. Shen, J. Wadsley, A. Pontzen, H. M. P. Couchman, T. Quinn, A. V. Macciò, and B. K. Gibson. MAGICC haloes: confronting simulations with observations of the circumgalactic medium at z=0. *MNRAS*, 425:1270–1277, September 2012. doi: 10.1111/j.1365-2966.2012.21522.x.

G. S. Stinson, C. Brook, A. V. Macciò, J. Wadsley, T. R. Quinn, and H. M. P. Couchman. Making Galaxies In a Cosmological Context: the need for early stellar feedback. *MNRAS*, 428:129–140, January 2013. doi: 10.1093/mnras/sts028.

G. S. Stinson, A. A. Dutton, L. Wang, A. V. Macciò, J. Herpich, J. D. Bradford, T. R. Quinn, J. Wadsley, and B. Keller. NIHAO III: the constant disc gas mass conspiracy. *MNRAS*, 454:1105–1116, November 2015. doi: 10.1093/mnras/stv1985.

I. Strateva, Ž. Ivezić, G. R. Knapp, V. K. Narayanan, M. A. Strauss, J. E. Gunn, R. H. Lupton, D. Schlegel, N. A. Bahcall, J. Brinkmann, R. J. Brunner, T. Budavári, I. Csabai, F. J. Castander, M. Doi, M. Fukugita, Z. Győry, M. Hamabe, G. Hennessy, T. Ichikawa, P. Z. Kunszt, D. Q. Lamb, T. A. McKay, S. Okamura, J. Racusin, M. Sekiguchi, D. P. Schneider, K. Shimasaku, and D. York. Color Separation of Galaxy Types in the Sloan Digital Sky Survey Imaging Data. *AJ*, 122:1861–1874, October 2001. doi: 10.1086/323301.

K.-Y. Su, P. F. Hopkins, C. C. Hayward, C.-A. Faucher-Giguère, D. Kereš, X. Ma, and V. H. Robles. Feedback first: the surprisingly weak effects of magnetic fields, viscosity, conduction and metal diffusion on sub-L* galaxy formation. *MNRAS*, 471:144–166, October 2017. doi: 10.1093/mnras/stx1463.

T. Sukhbold, T. Ertl, S. E. Woosley, J. M. Brown, and H.-T. Janka. Core-collapse Supernovae from 9 to 120 Solar Masses Based on Neutrino-powered Explosions. *ApJ*, 821:38, April 2016. doi: 10.3847/0004-637X/821/1/38.

J. Suresh, K. H. R. Rubin, R. Kannan, J. K. Werk, L. Hernquist, and M. Vogelsberger. On the OVI Abundance in the Circumgalactic Medium of Low-Redshift Galaxies. *ArXiv e-prints 1511.00687*, November 2015.

J. Suresh, K. H. R. Rubin, R. Kannan, J. K. Werk, L. Hernquist, and M. Vogelsberger. On the OVI abundance in the circumgalactic medium of low-redshift galaxies. *MNRAS*, 465:2966–2982, March 2017. doi: 10.1093/mnras/stw2499.

S. Tacchella, A. Dekel, C. M. Carollo, D. Ceverino, C. DeGraf, S. Lapiner, N. Mandelker, and R. Primack Joel. The confinement of star-forming galaxies into a main sequence through episodes of gas compaction, depletion and replenishment. *MNRAS*, 457:2790–2813, April 2016. doi: 10.1093/mnras/stw131.

M. Takamiya, R. G. Kron, and G. E. Kron. Photoelectric Photometry of Zwicky Galaxies. *AJ*, 110:1083, September 1995. doi: 10.1086/117588.

M. Tala, P. Heeren, M. Grill, R. J. Harris, J. Stürmer, C. Schwab, T. A Gutcke, S. Reffert, A. Quirrenbach, W. Seifert, H. Mandel, L. Geuer, L. Schäffner, G. Thimm, U. Seeman, J. Tietz, and K. Wagner. A high-resolution spectrograph for the 72cm Waltz Telescope at Landessternwarte, Heidelberg. In *Society of Photo-Optical Instrumentation Engineers (SPIE) Conference Series*, volume 9908 of *Proc. SPIE*, page 99086O, August 2016. doi: 10.1117/12.2232730.

T. Theuns, M. Viel, S. Kay, J. Schaye, R. F. Carswell, and P. Tzanavaris. Galactic Winds in the Intergalactic Medium. *ApJ*, 578:L5–L8, October 2002. doi: 10.1086/344521.

C. Thom and H.-W. Chen. A STIS Survey for O VI Absorption Systems at 0.12 $<$ z $<\tilde{}$ 0.5. I. The Statistical Properties of Ionized Gas. *ApJ*, 683:22–32, August 2008. doi: 10.1086/587976.

T. A. Thompson, A. C. Fabian, E. Quataert, and N. Murray. Dynamics of dusty radiation-pressure-driven shells and clouds: fast outflows from galaxies, star clusters, massive stars, and AGN. *MNRAS*, 449:147–161, May 2015. doi: 10.1093/mnras/stv246.

E. Tollet, A. V. Macciò, A. A. Dutton, G. S. Stinson, L. Wang, C. Penzo, T. A Gutcke, T. Buck, X. Kang, C. Brook, A. Di Cintio, B. W. Keller, and J. Wadsley. NIHAO - IV: core creation and destruction in dark matter density profiles across cosmic time. *MNRAS*, 456:3542–3552, March 2016a. doi: 10.1093/mnras/stv2856.

E. Tollet, A. V. Macciò, A. A. Dutton, G. S. Stinson, L. Wang, C. Penzo, T. A. Gutcke, T. Buck, X. Kang, C. Brook, A. Di Cintio, B. W. Keller, and J. Wadsley. NIHAO - IV: core creation and destruction in dark matter density profiles across cosmic time. *MNRAS*, 456:3542–3552, March 2016b. doi: 10.1093/mnras/stv2856.

J. W. Trayford, T. Theuns, R. G. Bower, R. A. Crain, C. d. P. Lagos, M. Schaller, and J. Schaye. It is not easy being green: the evolution of galaxy colour in the EAGLE simulation. *MNRAS*, 460:3925–3939, August 2016. doi: 10.1093/mnras/stw1230.

C. A. Tremonti, T. M. Heckman, G. Kauffmann, J. Brinchmann, S. Charlot, S. D. M. White, M. Seibert, E. W. Peng, D. J. Schlegel, A. Uomoto, M. Fukugita, and J. Brinkmann. The Origin of the Mass-Metallicity Relation: Insights from 53,000 Star-forming Galaxies in the Sloan Digital Sky Survey. *ApJ*, 613:898–913, October 2004. doi: 10.1086/423264.

T. M. Tripp, K. R. Sembach, D. V. Bowen, B. D. Savage, E. B. Jenkins, N. Lehner, and P. Richter. A High-Resolution Survey of Low-Redshift QSO Absorption Lines: Statistics and Physical Conditions of O VI Absorbers. *ApJS*, 177: 39–102, July 2008. doi: 10.1086/587486.

R. B. Tully and J. R. Fisher. A new method of determining distances to galaxies. *A&A*, 54:661–673, February 1977.

J. Tumlinson, C. Thom, J. K. Werk, J. X. Prochaska, T. M. Tripp, D. H. Weinberg, M. S. Peeples, J. M. O'Meara, B. D. Oppenheimer, J. D. Meiring, N. S. Katz, R. Davé, A. B. Ford, and K. R. Sembach. The Large, Oxygen-Rich Halos of Star-Forming Galaxies Are a Major Reservoir of Galactic Metals. *Science*, 334:948–, November 2011. doi: 10.1126/science.1209840.

J. Tumlinson, C. Thom, J. K. Werk, J. X. Prochaska, T. M. Tripp, N. Katz, R. Davé, B. D. Oppenheimer, J. D. Meiring, A. B. Ford, J. M. O'Meara, M. S. Peeples, K. R. Sembach, and D. H. Weinberg. The COS-Halos Survey: Rationale, Design, and a Census of Circumgalactic Neutral Hydrogen. *ApJ*, 777:59, November 2013. doi: 10.1088/0004-637X/777/1/59.

A. Vazdekis, E. Casuso, R. F. Peletier, and J. E. Beckman. A New Chemo-evolutionary Population Synthesis Model for Early-Type Galaxies. I. Theoretical Basis. *ApJS*, 106:307, October 1996. doi: 10.1086/192340.

M. Vogelsberger, S. Genel, D. Sijacki, P. Torrey, V. Springel, and L. Hernquist. A model for cosmological simulations of galaxy formation physics. *MNRAS*, 436:3031–3067, December 2013. doi: 10.1093/mnras/stt1789.

M. Vogelsberger, S. Genel, V. Springel, P. Torrey, D. Sijacki, D. Xu, G. Snyder, D. Nelson, and L. Hernquist. Introducing the Illustris Project: simulating the coevolution of dark and visible matter in the Universe. *MNRAS*, 444: 1518–1547, October 2014. doi: 10.1093/mnras/stu1536.

J. W. Wadsley, J. Stadel, and T. Quinn. Gasoline: a flexible, parallel implementation of TreeSPH. *New Astron.*, 9:137–158, February 2004. doi: 10.1016/j.newast.2003.08.004.

J. W. Wadsley, G. Veeravalli, and H. M. P. Couchman. On the treatment of entropy mixing in numerical cosmology. *MNRAS*, 387:427–438, June 2008. doi: 10.1111/j.1365-2966.2008.13260.x.

J. W. Wadsley, B. W. Keller, and T. R. Quinn. Gasoline2: a modern smoothed particle hydrodynamics code. *MNRAS*, 471:2357–2369, October 2017. doi: 10.1093/mnras/stx1643.

L. Wang, A. A. Dutton, G. S. Stinson, A. V. Macciò, C. Penzo, X. Kang, B. W. Keller, and J. Wadsley. NIHAO project - I. Reproducing the inefficiency of galaxy formation across cosmic time with a large sample of cosmological hydrodynamical simulations. *MNRAS*, 454:83–94, November 2015. doi: 10.1093/mnras/stv1937.

L. Wang, A. A. Dutton, G. S. Stinson, A. V. Macciò, T. A Gutcke, and X. Kang. NIHAO VII: predictions for the galactic baryon budget in dwarf to Milky Way mass haloes. *MNRAS*, 466:4858–4867, April 2017. doi: 10.1093/mnras/stx066.

R. Weinberger, V. Springel, L. Hernquist, A. Pillepich, F. Marinacci, R. Pakmor, D. Nelson, S. Genel, M. Vogelsberger, J. Naiman, and P. Torrey. Simulating galaxy formation with black hole driven thermal and kinetic feedback. *MNRAS*, 465:3291–3308, March 2017. doi: 10.1093/mnras/stw2944.

D. R. Weisz, L. C. Johnson, D. Foreman-Mackey, A. E. Dolphin, L. C. Beerman, B. F. Williams, J. J. Dalcanton, H.-W. Rix, D. W. Hogg, M. Fouesneau, B. D. Johnson, E. F. Bell, M. L. Boyer, D. Gouliermis, P. Guhathakurta, J. S. Kalirai, A. R. Lewis, A. C. Seth, and E. D. Skillman. The High-mass Stellar Initial Mass Function in M31 Clusters. *ApJ*, 806:198, June 2015. doi: 10.1088/0004-637X/806/2/198.

J. K. Werk, J. X. Prochaska, J. Tumlinson, M. S. Peeples, T. M. Tripp, A. J. Fox, N. Lehner, C. Thom, J. M. O'Meara, A. B. Ford, R. Bordoloi, N. Katz, N. Tejos, B. D. Oppenheimer, R. Davé, and D. H. Weinberg. The COS-Halos Survey: Physical Conditions and Baryonic Mass in the Low-redshift Circumgalactic Medium. *ApJ*, 792:8, September 2014. doi: 10.1088/0004-637X/792/1/8.

S. D. M. White and C. S. Frenk. Galaxy formation through hierarchical clustering. *ApJ*, 379:52–79, September 1991. doi: 10.1086/170483.

S. D. M. White and M. J. Rees. Core condensation in heavy halos - A two-stage theory for galaxy formation and clustering. *MNRAS*, 183:341–358, May 1978.

V. Wild, F. Rosales-Ortega, J. Falcón-Barroso, R. García-Benito, A. Gallazzi, R. M. González Delgado, S. Bekeraité, A. Pasquali, P. H. Johansson, B. García Lorenzo, G. van de Ven, M. Pawlik, E. Peréz, A. Monreal-Ibero, M. Lyubenova, R. Cid Fernandes, J. Méndez-Abreu, J. Barrera-Ballesteros, C. Kehrig, J. Iglesias-Páramo, D. J. Bomans, I. Márquez, B. D. Johnson, R. C. Kennicutt, B. Husemann, D. Mast, S. F. Sánchez, C. J. Walcher, J. Alves, A. L. Aguerri, A. Alonso Herrero, J. Bland-Hawthorn, C. Catalán-Torrecilla, E. Florido, J. M. Gomes, K. Jahnke, Á. R. López-Sánchez, A. de Lorenzo-Cáceres, R. A. Marino, E. Mármol-Queraltó, P. Olden, A. del Olmo, P. Papaderos, A. Quirrenbach, J. M. Vílchez, and B. Ziegler. The Mice at play in the CALIFA survey. A case study of a gas-rich major merger between first passage and coalescence. *A&A*, 567:A132, July 2014. doi: 10.1051/0004-6361/201321624.

T. K. Wyder, D. C. Martin, D. Schiminovich, M. Seibert, T. Budavári, M. A. Treyer, T. A. Barlow, K. Forster, P. G. Friedman, P. Morrissey, S. G. Neff, T. Small, L. Bianchi, J. Donas, T. M. Heckman, Y.-W. Lee, B. F. Madore, B. Milliard, R. M. Rich, A. S. Szalay, B. Y. Welsh, and S. K. Yi. The UV-Optical Galaxy Color-Magnitude Diagram. I. Basic Properties. *ApJS*, 173:293–314, December 2007. doi: 10.1086/521402.

Z. Yan, T. Jerabkova, and P. Kroupa. The optimally-sampled galaxy-wide stellar initial mass function - Observational tests and the publicly available GalIMF code. *ArXiv e-prints*, July 2017.

H. M. Yesuf, S. M. Faber, J. R. Trump, D. C. Koo, J. J. Fang, F. S. Liu, V. Wild, and C. C. Hayward. From Starburst to Quiescence: Testing Active Galactic Nucleus feedback in Rapidly Quenching Post-starburst Galaxies. *ApJ*, 792: 84, September 2014. doi: 10.1088/0004-637X/792/2/84.

F. Yuan and R. Narayan. Hot Accretion Flows Around Black Holes. *ARA&A*, 52:529–588, August 2014. doi: 10.1146/annurev-astro-082812-141003.

8

Acknowledgements

I thank Andrea Macciò for giving me the opportunity to persue a PhD and for being my advisor throughout these last four years. I also thank Volker Springel for accepting me into his group and for supporting my work in the last two years. Without him, of course no work with AREPO would be possible.

Next, I want to thank Hans-Walter Rix for accepting the extra work of being my examiner. But more importantly, for being interested in my work and supporting my scientific progress. Not least, I'd like to thank Luca Amendola for showing me the work of early cosmologists and for being on my defense panel.

A big thank you to Glenn van de Ven, Jonathan Stern, Robert Grand and Rüdiger Pakmor for scientific insights, suggestions and useful conversation. I would particularly like to thank Morgan Fouesneau and Alessandra Mastrobuono-Battisti for kind and constructive feedback on this thesis. A special credit goes to Emanuele Paolo Farina for the many ravioli that got me through the PhD.

I graciously acknowledge the funding I received through the Collaborative Research Centre SFB 881 "The Milky Way System" (subproject A1) of the German Research Foundation (DFG).

The simulations were carried out on the High Performance Computing resources of the THEO, HYDRA and DRACO clusters at the Max Planck Computing and Data Facility (MPCDF) in Garching operated by the Max Planck Society (MPG).

GASOLINE2 was developed and written by Tom Quinn and James Wadsley. Without their contributions, this thesis would have been impossible. Some analysis was performed using the `pynbody` package (http://pynbody.github.io/, Pontzen et al. 2013), written by Andrew Pontzen and Rok Roškar.